

INVESTIGATION OF DAMAGE IN GFRP TAPERED COMPOSITE
LAMINATES

A THESIS SUBMITTED TO
THE GRADUATE SCHOOL OF NATURAL AND APPLIED SCIENCES
OF
MIDDLE EAST TECHNICAL UNIVERSITY

BY

SAEID HOSSEINPOUR DASHATAN

IN PARTIAL FULFILLMENT OF THE REQUIREMENTS
FOR
THE DEGREE OF DOCTOR OF PHILOSOPHY
IN
MECHANICAL ENGINEERING

AUGUST 2021

Approval of the thesis:

**INVESTIGATION OF DAMAGE IN GFRP TAPERED COMPOSITE
LAMINATES**

submitted by **SAEID HOSSEINPOUR DASHATAN** in partial fulfillment of the requirements for the degree of **Doctor of Philosophy in Mechanical Engineering Department, Middle East Technical University** by,

Prof. Dr. Halil Kalıpçılar
Dean, Graduate School of **Natural and Applied Sciences**

Prof. Dr. M. A. Sahir Arıkan
Head of Department, **Mechanical Engineering**

Prof. Dr. M. A. Sahir Arıkan
Supervisor, **Mechanical Engineering, METU**

Prof. Dr. Levend Parnas
Co-supervisor, **Mechanical Engineering, TED University**

Examining Committee Members:

Prof. Dr. Suat Kadiođlu
Mechanical Engineering, METU

Prof. Dr. M. A. Sahir Arıkan
Mechanical Engineering, METU

Prof. Dr. Demirkan öker
Aerospace Engineering, METU

Assoc. Prof. Dr. Cihan Tekođlu
Mechanical Engineering, TOBB ETU

Assist. Prof. Dr. Őhram Dizeci
Mechanical Engineering, TED University

Date: 13.08.2021:

I hereby declare that all information in this document has been obtained and presented in accordance with academic rules and ethical conduct. I also declare that, as required by these rules and conduct, I have fully cited and referenced all material and results that are not original to this work.

Name, Surname: Saeid Hosseinpour Dashatan

Signature :

ABSTRACT

INVESTIGATION OF DAMAGE IN GFRP TAPERED COMPOSITE LAMINATES

Dashatan, Saeid Hosseinpour
Ph.D., Department of Mechanical Engineering
Supervisor: Prof. Dr. M. A. Sahir Arıkan
Co-Supervisor: Prof. Dr. Levend Parnas

August 2021, 113 pages

In some applications of composite laminates, thickness variation is necessary to fulfill specific design requirements. One way of accomplishing the intentional thickness variation in composite structures is terminating some plies within a layup. Introducing ply drop-offs causes geometrical and material discontinuities, which lead to high localized stresses around drop-off locations. Despite all the progress made in damage analyses of tapered composite laminates, estimating their load-carrying capacity and strength remains a significant challenge.

In this study, damage in tapered composite laminates under tensile loading is investigated. The cohesive zone method is used to simulate the delamination failure. For simulation of intralaminar damages, a 3-D continuum damage mechanics-based model with Hashin criteria for damage initiation and bi-linear damage propagation softening is employed. Finite element analyses are implemented in Abaqus/Explicit. Computational results are compared to an experimental study.

No significant fiber or matrix damage is detected before and during delaminations. In

addition to loads corresponding to delamination onset, both delamination locations and propagation characteristics are also utilized for making comparisons between computational results and experimental observations. Dynamic characteristic of delamination is employed to validate numerical analyses, further. For this purpose, the delamination predictions are compared to images taken by a high-speed camera. Results show that the ply drop-off type influences laminates' strength and governs the delamination growth to be either dynamic (unstable) or static (stable). A good correlation between experimental and finite element results is observed in terms of delamination onset location, propagation patterns, and stability of delamination growth. For some specimen types, a modified cohesive strength pair is required to enhance these correlations.

To further investigate the local delamination behavior around the resin pocket, combinations of unidirectional plies with 0° and 45° orientations for a laminate with a single, double, and three drop-offs are considered as well. In addition to delamination patterns, the load transfer mechanism, especially in the drop-off region, is also studied. A different delamination behavior is detected for each case, which shows the significance of the effect of orientation of each sublaminar on the load transfer mechanism. Also, results show that the progression of delaminations within various interfaces to be similar for both 2-D and 3-D models in laminates with 0° plies. However, there are some differences in laminates, including 0° . Also, the 3-D model clarifies the significance of ply orientation in delamination propagation patterns, which is not detectable in the 2-D model.

Keywords: Tapered Laminate, Cohesive Zone Modeling, Delamination

ÖZ

DARALAN KESİTLİ KOMPOZİT TABAKALARDA HASAR İNCELENMESİ

Dashatan, Saeid Hosseinpour

Doktora, Makina Mühendisliği Bölümü

Tez Yöneticisi: Prof. Dr. M. A. Sahir Arıkan

Ortak Tez Yöneticisi: Prof. Dr. Levend Parnas

Ağustos 2021 , 113 sayfa

Kompozit yapıların bazı uygulamalarında, belirli tasarım gereklerini karşılamak için kalınlık değişimi gereklidir. Kalınlık değişimini gerçekleştirmenin bir yolu, bir serimin içindeki belirli konumlarda bazı katmanları sonlandırmaktır. Katman düşmeleri, sonlandırma konumlarının çevresinde yüksek lokalize gerilimlere yol açan geometrik ve malzeme süreksizliklerine neden olup bu tür yapıların hasar analizini sabit kalınlıktaki laminatlara kıyasla daha karmaşık bir hale getirir. Daralan kesitli kompozit yapılarının hasar modellemesinde kaydedilen tüm ilerlemeler rağmen, yük taşıma kapasitelerini ve mukavemetlerini tahmin etmek önemli bir problem olmaya devam etmektedir.

Bu çalışmada, daralan kesitli kompozit laminatlardaki çekme yükü altında oluşan hasarlar incelenmiştir. Katmanlar arası hasarı modellemesi için yapışkan arayüz metodu ve Katmanlar içi hasar modellemesinde Hashin hasar başlangıç kriterine sahip sürekli hasarı mekaniği temelli 3-B bir model kullanılıp sonlu elemanlar Abaqus/Explicit analiz programına uygulanmıştır. Sonlu eleman modelleme sonuçları deneysel

bir çalışmanın sonuçları, delaminasyon başlangıcına karşılık gelen yüklere ek olarak, delaminasyon konumları ve yayılma özellikleri açısından karşılaştırılmıştır. Bu amaçla, delaminasyon hesaplamalarında kullanılan yapışkan arayüz yöntemi ile elde edilen sonuçlar yüksek hızlı kamera ile çekilen görüntülerle karşılaştırılmıştır. Sonuçlar, tabaka sonlanma biçiminin sadece mukavemeti etkilemekle sınırlı kalmadığını, dinamik (kararsız) veya statik (kararlı) olacak şekilde delaminasyon büyümesini de belirlediğini göstermektedir. Delaminasyon başlangıç konumu, ilerleme biçimleri ve delaminasyon büyümesinin stabilitesi açısından deneysel ve sonlu elemanlar analiz sonuçları arasında iyi bir uyum gözlemlenmiştir.

Reçine zengin bölge etrafındaki lokal delaminasyon davranışını daha detaylı araştırmak için tek, çift ve üç tabaka sonlanma içeren bir laminat için 0° ve 45° yönelimli tek yönlü tabaka kombinasyonları da incelenmiştir. Her bir kombinasyon için farklı delaminasyon davranışı gözlenmiş, bu da her bir alt tabakanın oryantasyon etkisinin yük transfer mekanizmasına etkisinin önemini göstermektedir. Ayrıca sonuçlar, 0° tabakalı yapılarda hem 2-B hem de 3-B modeller için çeşitli arayüzlerdeki delaminasyonların ilerlemesini gösterilmiştir. Ancak, tabakalı yapılarda 0° de dahil olmak üzere bazı farklılıklar vardır. Ayrıca 3-B model, 2-B modelde saptanamayan delaminasyon ilerleme modellerinde kat oryantasyonunun önemini ortaya çıkartmıştır.

Anahtar Kelimeler: Daralan kesit, ileri kompozit yapılar, yapışkan arayüz, delaminasyon

To My Family

ACKNOWLEDGMENTS

First, I would like to express my deepest gratitude to my supervisor Prof. Dr. Sahir Arıkan, for his support, insight, and patience.

I would like to dedicate my sincere appreciation to my co-supervisor Prof. Dr. Levend Parnas for his continuous support, guidance, encouragement, and criticism during my Ph.D. thesis in Middle East Technical University. His contribution to my academic knowledge and professional life is extremely precious and truly exceptional.

I feel very fortunate and honorable to work with Prof. Dr. Demirkan Çöker during my research. I want to thank him for his endless support, enlightenment, and contribution to this thesis.

I would like to thank my thesis monitoring committee members, Prof. Dr. Suat Kadiođlu, and Assist. Prof. Dr. Şehram Dizeci for their precious comments and discussions about my thesis.

I would also like to thank the jury members of my Ph.D. thesis for their valuable suggestions and feedbacks.

My other special thanks would go to Burak Ođün Yavuz, Miraç Onur Bozkurt, and Emine Burçin Özenç at Rüzgem Structures and Materials Laboratories in Middle East Technical University, where the experiments were conducted. Their contribution to this research is gratefully acknowledged.

I would like to express my special gratitude to the Turkish Aerospace – Rotary Wing Technology Center who funded this study under DKTM/2015/05 project.

Last but not least, my warm thanks go to my dear family, especially my beloved Farnaz, for supporting and encouraging me all the way coming along.

TABLE OF CONTENTS

ABSTRACT	v
ÖZ	vii
ACKNOWLEDGMENTS	x
TABLE OF CONTENTS	xi
LIST OF TABLES	xiv
LIST OF FIGURES	xv
LIST OF ABBREVIATIONS	xx
CHAPTERS	
1 INTRODUCTION	1
1.1 Literature Review	4
1.2 Research Objectives and Outline of Thesis	6
2 MODELING DAMAGE IN TAPERED COMPOSITE LAMINATES	9
2.1 Introduction	9
2.2 Interlaminar Damage	9
2.2.1 Cohesive Zone Modeling	11
2.2.2 Cohesive Zone Parameters	14
2.3 Intralaminar Damage	16
2.3.1 Constitutive Damage Model	17

2.3.2	Damage Evolution	18
2.3.3	Single-Element Test of Ply Damage Model	20
3	VERIFICATION STUDY	25
3.1	Introduction	25
3.2	Experimental Procedure and Specimens Specifications	25
3.3	Finite Element Modeling	29
3.3.1	Material Properties	33
4	RESULTS AND DISCUSSIONS FOR VALIDATION STUDY	35
4.1	Introduction	35
4.2	Experimental Results	35
4.3	Finite Element Results	41
4.4	Discussions	49
4.4.1	Stiffness and Strain	49
4.4.2	Delamination Onset Loads	52
4.4.3	Delamination Initiation and Propagation	53
4.5	Chapter Conclusions	60
5	PARAMETRIC STUDY	63
5.1	Introduction	63
5.2	Model Details	63
5.3	Results	65
5.3.1	2-D Implicit Results	65
5.3.2	2-D Explicit Analysis Results	69
5.3.3	Delamination Propagation Speed	71

5.3.4	2-D vs. 3-D Results	76
5.4	Chapter Conclusions	80
6	CONCLUSIONS AND FUTURE STUDY	83
6.1	Summary	83
	REFERENCES	87
A	95
	CURRICULUM VITAE	111

LIST OF TABLES

TABLES

Table 3.1	Mechanical and interface properties of Glass/Epoxy [1].	33
Table 5.1	Displacement, load, initial and final stiffness for each laminate. . . .	67

LIST OF FIGURES

FIGURES

Figure 1.1	Thickness variations along a wind turbine blade [2].	1
Figure 1.2	(a) Bearingless main rotor hub system, (b) Baseline flexbeam with inconstant thickness [3].	2
Figure 1.3	Schematics and definitions used in a tapered laminate.	3
Figure 2.1	Examples of geometric and material discontinuities as sources of delaminations [4].	10
Figure 2.2	Bi-Linear traction separation law for a single-mode of loading [5].	11
Figure 2.3	Definition of Mode I (normal opening), Mode II (in plane shearing) and Mode III (out-of-plane shearing).	12
Figure 2.4	Bi-Linear traction separation law for a mixed-mode loading case [5].	13
Figure 2.5	Development of damage in elements within cohesive zone length [6].	15
Figure 2.6	Linear Softening model.	19
Figure 2.7	Flowchart of VUMAT code.	21
Figure 2.8	Loading and boundary conditions of single element test for (a) fiber tension (b) fiber compression (c) matrix tension and (d) matrix compression.	22

Figure 2.9	Load-displacement diagrams of single-element test for fiber damage in: (a) tension, (b) compression.	23
Figure 2.10	Load-displacement diagrams of single-element test for matrix damage in: (a) tension, (b) compression.	24
Figure 3.1	(a) Tapered geometry for each configuration and designation, (b) corresponding micro-graphs of test specimens.	26
Figure 3.2	Geometry and dimensions of specimens.	27
Figure 3.3	Experimental setup.	28
Figure 3.4	Locations of cohesive layers for each specimen type are shown in red color.	30
Figure 3.5	Finer cohesive element in tie-constraint method.	31
Figure 3.6	Boundary conditions.	31
Figure 4.1	High-speed images showing damage sequence in U-1.	36
Figure 4.2	High-speed images showing damage sequence in configuration U-2.	37
Figure 4.3	High-speed images showing damage sequence in configuration U-3.	38
Figure 4.4	High-speed images showing damage sequence in U-4.	40
Figure 4.5	Damage sequence in configuration U-5.	41
Figure 4.6	Internal and kinetic energy history in Explicit FEA for configuration U-1.	42
Figure 4.7	Delamination sequences in FEM results for U-1.	43

Figure 4.8	State of damage variable for cohesive element and fiber failure index at a frame just before initiation of fiber damage in configuration U-1.	44
Figure 4.9	State of fiber failure index and fiber damage variable a frame just after initiation of fiber damage in configuration U-1.	45
Figure 4.10	State of fiber failure index at fiber damage variable at the end of loading for configuration U-1.	46
Figure 4.11	Delamination sequences in FEM results for U-2.	47
Figure 4.12	FEM results for configuration U-3 (a) delamination state in edge view , (b) delamination sequence in 3D view.	48
Figure 4.13	Load-displacement curve for specimens from FE results and stroke of test machine.	50
Figure 4.14	Load-displacement curve for U-1 specimen from FE, test machine stroke, DIC and theory.	51
Figure 4.15	Comparison of longitudinal strains from DIC and FEM for configuration U-1.	52
Figure 4.16	Delamination onset load predicted in FEM and measured in experiments.	53
Figure 4.17	Delamination sequences for U-1 configurations (a) experiment, (b) FEM.	54
Figure 4.18	Delamination sequences for U-2 (a) experiment, (b) FEM.	55
Figure 4.19	Delamination sequences for U-3 (a) experiment, (b) FEM.	56
Figure 4.20	Premature delamination in , (a) U-4, (b) U-5.	56
Figure 4.21	Damage evolution and equivalent stress distribution for U-4 specimen with enhanced interface strength.	57

Figure 4.22	Damage evolution for U-5 configuration with enhanced interface strength.	58
Figure 4.23	Delamination load values obtained by nominal strength pair (NSP), enhanced strength pairs (ESP) and experimental results.	59
Figure 5.1	Geometry and Boundary conditions.	64
Figure 5.2	Load-displacement curves for implicit FEA for various ply orientations in (a) 1 drop-off (b) 2 drop-offs (c) 3 drop-offs.	65
Figure 5.3	Load-displacement curves for implicit FEA for similar lay-up and different drop-off number.	66
Figure 5.4	Delamination initiation location for (a) with double drop-offs, (b) $[0/\underline{0}_3/0]_s$ and $[45/\underline{0}_3/0]_s$ and (c) $[0/\underline{45}_3/0]_s$	67
Figure 5.5	Distribution of equivalent stresses in laminate with 2 drop-offs before and after first load-drop.	68
Figure 5.6	Distribution of equivalent stresses in laminates with 3 drop-offs before and after first load-drop.	68
Figure 5.7	Distribution of equivalent stresses after last load-drop in laminates with (a) 2 drop-offs, (b) 3 drop-offs.	69
Figure 5.8	Load-displacement curves for implicit and explicit analyses.	70
Figure 5.9	Delamination propagation patterns in different lay-ups.	71
Figure 5.10	Crack length and crack tip speed vs. time plots for crack initiation in laminates with 2 drop-offs.	72
Figure 5.11	Crack length and crack tip speed vs. time plots for the crack growing into thin section for laminates with 2 drop-offs.	73
Figure 5.12	Crack length and crack tip speed vs. time plots for initial crack in laminates with 3 drop-offs.	74

Figure 5.13	Crack length and Crack tip speed vs. time plots for the crack growing into thin section for laminates with 3 drop-offs.	75
Figure 5.14	Crack length and crack tip speed vs. time plots for all cracks in $[0/45_3/0]_s$ laminate.	76
Figure 5.15	Comparison of load-displacement behavior for 2-D and 3-D explicit analyses.	77
Figure 5.16	Delamination initiation and propagation patterns in 3-D results. . .	78
Figure 5.17	A non-uniform width-wise delamination.	79
Figure 5.18	Comparison of crack length and crack tip speed plots for 2-D and 3-D explicit analyses.	80

LIST OF ABBREVIATIONS

2-D	Two dimensional
3-D	Three dimensional
B-K	Benzeggagh-Kenane
CBS	Curved beam specimen
CDM	Continuum damage mechanics
CZM	Cohesive zone method
DCB	Double cantilever beam
DIC	Digital image correlation
ENF	End-notched flexure
ERR	Energy release rate
ESP	Enhanced strengths pair
FC	Fiber compression
FE	Finite element
FEM	Finite element method
FI	Failure index
FT	Fiber tension
HSC	High-speed camera
ILSS	Interlaminar shear strength
ILTS	Interlaminar tensile strength
NSP	Nominal strength pair
MC	Matrix compression
MT	Matrix tension
SDEG	Scalar stiffness degradation variable
SDV	Solution dependent state variable

TSL	Traction-separation law
TTC	Through-thickness compression

CHAPTER 1

INTRODUCTION

Application of advanced laminated composites have ever been increasing, specifically in the aerospace industry. This trend is mainly due to their significantly higher specific strength and stiffness values over conventional metallic materials, allowing fabrication of structures and components in lower weight. In some applications of composite laminates, thickness variation is necessary to achieve a predefined geometry, stiffness tailoring, or to satisfy other design requirements. In structures such as helicopter rotors or wind turbine blades, stresses are higher in the root region, near the blade hub, and decrease toward the blade tip. They have thicker root sections, which are progressively reduced to thinner sections around the tip (Fig. 1.1).

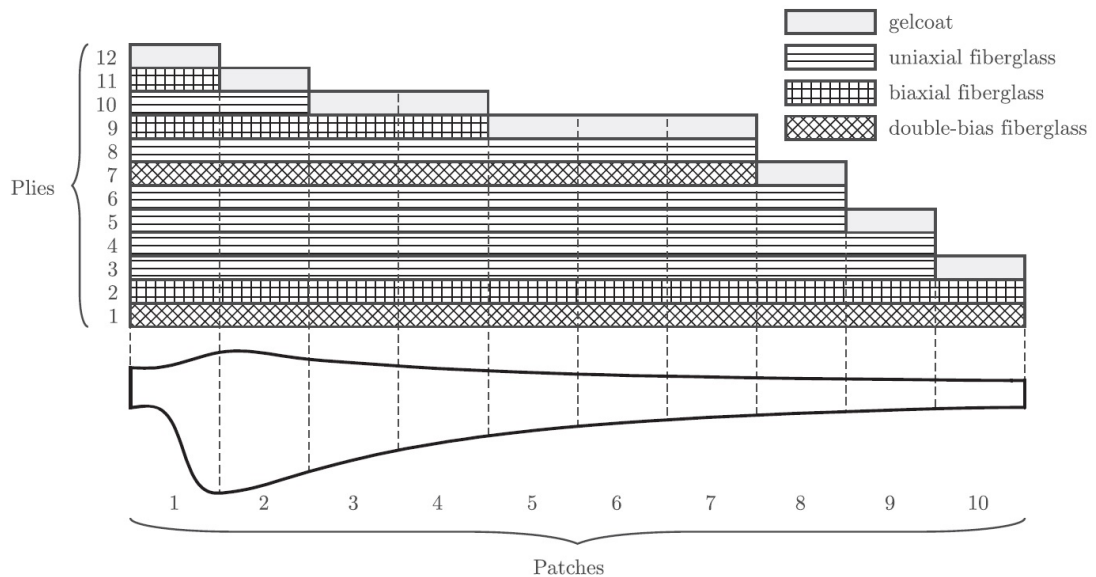
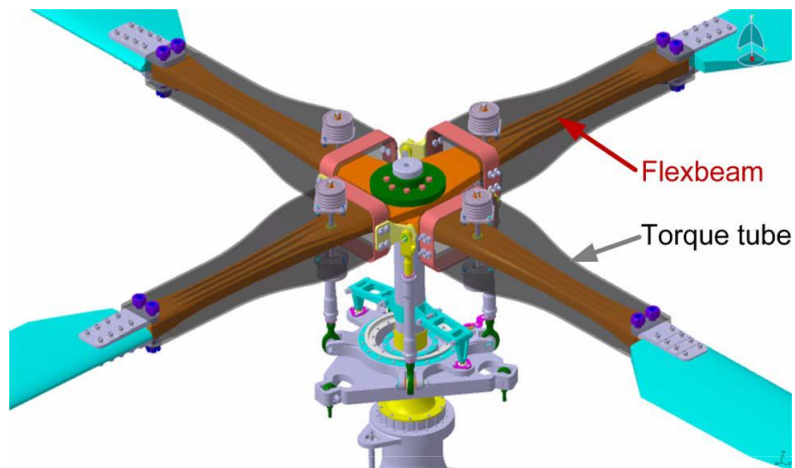


Figure 1.1: Thickness variations along a wind turbine blade [2].

Another specific instance, in the flexbeam of a helicopter rotor hub, during the flight,

the rotor hub is subjected to axial tension from centrifugal loads as well as bending in the flapping flexure region. Therefore, it is required to provide high stiffness around the hub, where structural displacements are preferred to be limited. At the same time, it must be relatively flexible, where large flapping motions of the blade itself must be accommodated [7]. A bearingless rotor hub system with the baseline flexbeam is shown in Fig. 1.2.



(a)



(b)

Figure 1.2: (a) Bearingless main rotor hub system, (b) Baseline flexbeam with constant thickness [3].

One way of accomplishing thickness variation in composite structures can be obtained by terminating some plies in specific locations within a layup, which leads to a

laminate with tapered geometry. The use of laminate tapering by ply terminations results in a significant saving in materials, and hence a remarkable weight reduction can be achieved. The ply termination is commonly referred to as ply drop-off. A tapered laminate can be considered to be composed of three sub-regions that are referred to be thin, tapered, and thick sections as schematically shown in Fig. 1.3.

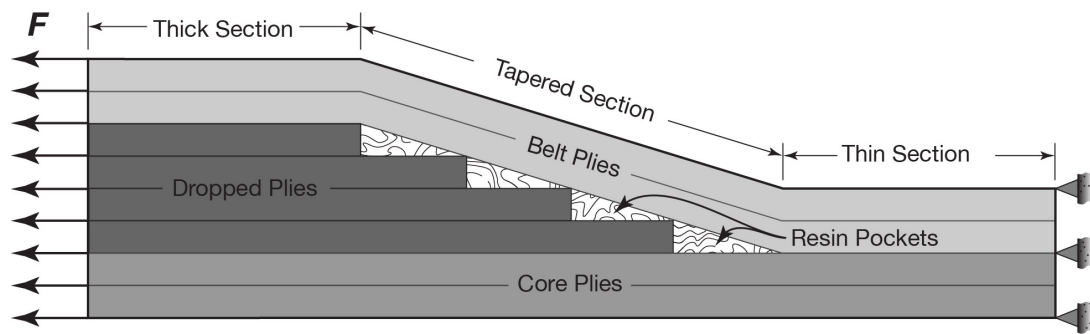


Figure 1.3: Schematics and definitions used in a tapered laminate.

Plies in a tapered laminate can be categorized into three groups, namely continuous (core) plies, terminated (dropped) plies, and cover (belt) plies. Among these, core and belt plies are both continuous. Additionally, resin-rich regions or resin pockets are formed in front of drop-offs [8].

Despite the advantages provided by tapered laminates, ply drop-offs cause geometrical and material discontinuities, which lead to high localized stresses, especially around ply terminations. Stress concentrations and lack of fiber reinforcement at ply termination locations in the interlaminar direction can instigate delaminations, as the dominant damage type, at well below the nominal strength of the laminate [9–12]. Therefore, the strength of a tapered structure is highly dependent on the strength of the tapered region [13]. There is a certain load shared by terminated plies in the thick section. However, in the tapered section, the load carried by them is transferred to the adjacent continuous plies, resulting in a complex interlaminar and intralaminar stress distribution. The resulting stress concentrations and complicated load distribution in the tapered region make the damage analysis in such structures complicated compared to laminates of constant thickness [14, 15].

1.1 Literature Review

Various analytical, numerical, and experimental studies are addressed to deal with the damage caused by introducing ply drop-off in tapered composite laminates [16–25]. Delamination is reported to be the dominant failure mode in tapered laminates. However, ply damage is also reported in some studies [10]. A comprehensive review of damage in tapered laminates can be found in [26,27]. Also, various parametric studies [28–31] have been carried out, and some design guidelines and rules of thumb are developed to minimize the drawbacks associated with drop-offs. Taper angle, distance between dropped plies, taper ratio and drop-off locations are the most considered parameters in these studies. A discussion of these guidelines can be found in [8, 32]. Some of the essential guidelines used in the design of tapered composite laminates are summarized as follows:

- Maintaining symmetry and balance of the laminate while dropping plies, to avoid bending/extension and bending/twisting couplings
- Minimizing the number of dropped plies in a single drop location (dropping more than two plies at the same location is not recommended)
- Minimizing the taper angle
- Keeping the distance between the terminated layers (stagger distance) to at least three times of the ply thickness
- Terminating the stiffest (0°) layer first and the most compliant (90°) layer last
- Avoiding termination of 0° and 90° layers adjacent to each other
- Plies on the upper and lower surfaces of the laminate should not be terminated
- A continuous ply should be kept every three consecutive dropped plies

Despite the functionality of these rules in primary designs, some problems may arise while utilizing these guidelines. First, simultaneous application of multiple rules may not be possible, and in some cases, they may conflict. For instance, minimizing the tapered angle may not be applicable for a predefined severely tapered geometry. Also,

dropping plies with three continuous layers in between can be limited by thickness ratios of thick to thin sections. Second, these guidelines are only qualitative and do not provide any information for a strength assessment [8, 25].

Analytical and numerical delamination studies on tapered laminates can be categorized into two groups. The first one is the strength-based approach in which the interlaminar stress distribution in the vicinity of ply interfaces is determined to locate the delamination onset. It predicts the delamination onset satisfactorily in the absence of the delamination propagation characterization. In contrast, in the fracture mechanics approach, the delamination progression can be predicted more effectively, but it requires the existence of an initial crack which may not be the case for a particular problem [26, 27].

As an increasingly used alternative, Cohesive Zone Modeling (CZM) has been widely utilized for the analyses of the delamination in composite laminates in recent years [33, 34]. The cohesive zone model assumes that the entire fracture zone is lumped into a crack plane. For composite delaminations, where crack paths are known, CZM comes out to be a very efficient method. In its implementation, cohesive elements are placed along potential delamination interfaces. They incorporate stress and fracture based approaches capable of both damage initiation and subsequent propagation without any requirement of a pre-crack. Thus, numerical problems involving singularities are avoided, which is another advantage over others [34]. Despite the widespread use of CZM in the modeling of delamination, studies related to tapered composite laminates are limited [8, 15, 35–39].

Harper et. al [36] utilized interface elements in numerical modeling of a tapered composite structural design. Despite good overall correlations with experimental results, some differences are reported. They point out that the fracture toughness values obtained in standard tests are underestimated in cohesive element modeling of tapered laminates, and a higher value is required. During the simulations, Mode I dominated delaminations just below the belt ply occur before final failure. This phenomenon is less significant in the experiments. For the simulation of drop-off region, they used a small void in the resin pocket front corner without any interface elements. Such artificial voids may not represent the physical problem, this, in turn has an adverse

effect on modeling results.

Gan et. al [8] worked on the development of a global-local finite element-based design approach for tapered laminates, where layered Timoshenko beam models are employed to predict delamination initiation starting from individual drop-offs. They conduct a comparison study with their model and a cohesive model analysis to demonstrate the ability of the local beam approach in identifying failure.

Zhang et. al [39] incorporated the interlaminar shear strength enhancement approach by implementing the through-thickness compression (TTC) into the cohesive law. It was previously found [40] that when there exists a large through-thickness compressive stress field around a cohesive layer, the strength of cohesive elements needs to be close to the real material strength values of interlaminar interfaces. Parametric studies are undertaken considering the effects of element size, cohesive strength pair, and TTC enhancement definitions on the numerical predictions.

1.2 Research Objectives and Outline of Thesis

The above studies mainly concentrated on the delamination loads or initiation locations, whereas delamination propagation and dynamic crack behavior are not considered. Some studies have pointed out the fact that delamination is intrinsically a dynamic phenomenon [41]. Dynamic characteristics of damage can be employed to validate numerical analyses further and, consequently, help to the development of more reliable predictions for the strength of tapered composite structures.

Despite all the progress made in analyzing damage in tapered composite laminates, estimating their load-carrying capacity and strength remains a significant challenge. Developing an appropriate modeling methodology capable of correctly predicting the damage behavior enables the evaluation of alternative design options and parameters for a specific tapered laminate. Understanding the failure mechanisms, particularly delamination behavior, is a critical step for developing such a methodology.

In this study, damage in tapered composite laminates is investigated. Abaqus/Explicit software package is utilized to carry out finite element analyses. Cohesive zone

modeling is used to predict delamination. For intralaminar damage, a 3-D continuum damage mechanics model with Hashin failure criteria is implemented into the finite element model via a user-written subroutine VUMAT. For validation, the finite element analysis results are compared to an experimental study in terms of delamination initiation location and the corresponding load as well as crack growth patterns and stability behavior of the crack growth.

The structure of the thesis is as follows: in Chapter 2, the theory of cohesive zone model and the continuum damage model used in this study are presented. Details of the specimens, their layups and corresponding finite element model are provided in Chapter 3. In Chapter 4, the results of finite element modeling and comparison with the experimental observation are presented. The results of parametric study is provided in Chapter 5. Finally, the outcome of the thesis with some suggestions for future studies are summarized in Chapter 6.

CHAPTER 2

MODELING DAMAGE IN TAPERED COMPOSITE LAMINATES

2.1 Introduction

Damage in laminated composites can be categorized into two modes, namely, intralaminar and interlaminar damage. Intralaminar damages occur in the plane of the plies. This mode includes fiber dominated damages (fiber breakage, fiber buckling), matrix-dominated damages (matrix cracking), and fiber-matrix debonding. The separation of two adjacent layers in the laminate, known as delamination, is the main interlaminar damage. Depending to the loading state and geometry of the laminate, combinations and interactions of these damage modes can also occur in a composite laminate. In this chapter, the theoretical background for each failure type and the corresponding modeling methods are discussed briefly. Also, the details of the user defined continuum damage model used in this study is discussed.

2.2 Interlaminar Damage

Interlaminar stresses between two adjacent plies can lead to crack formation and separation of the plies. This damage type is called delamination and is one of the most common and important failure modes in laminated composite structures due to their relatively weak interlaminar strengths. Delamination can occur under various circumstances. Material and structural discontinuities as interlaminar stress risers are the most common sources of delamination. Ply drops, regions subjected to out-of-plane bending such as curved beams, mismatch of properties in the free edge of adjacent plies, and transverse concentrated loads caused by low-velocity impacts are some

examples that delaminations are regularly observed (Fig. 2.1).

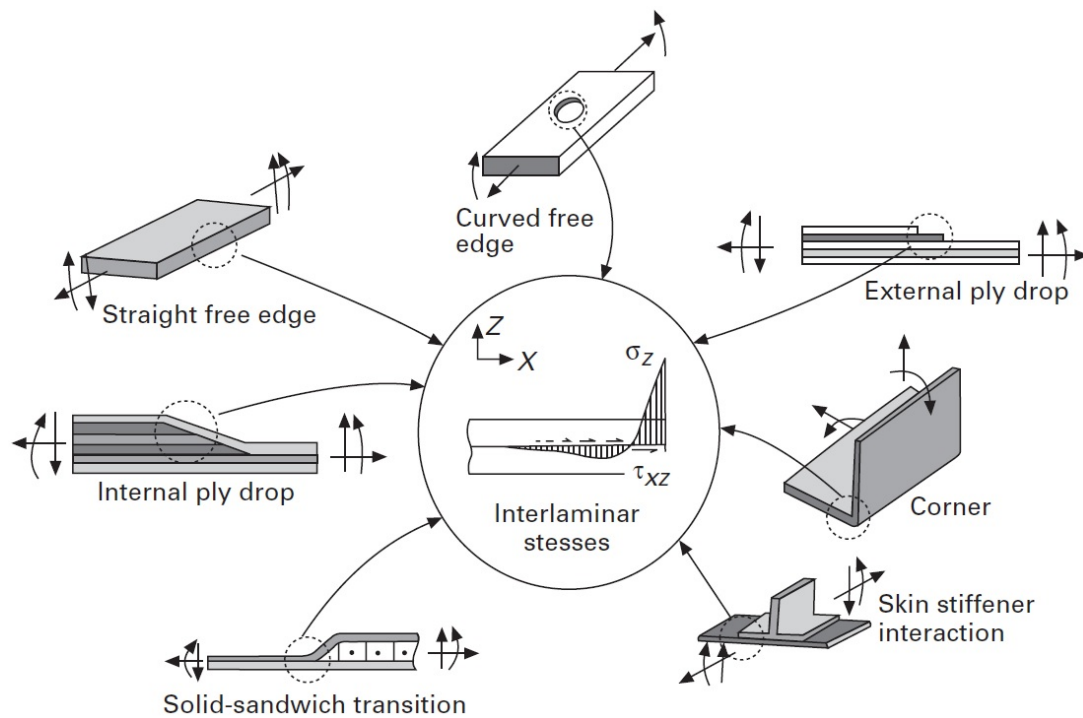


Figure 2.1: Examples of geometric and material discontinuities as sources of delaminations [4].

Various methods have been employed to predict delamination in composite laminates. The early attempts mainly concentrated on calculating interlaminar stresses, followed by applying appropriate failure criteria [42]. However, the effectiveness of this approach is limited due to singularity and problems associated with the calculation of out-of-plane stresses [43]. In addition, it has the restriction of predicting only delamination initiation. Another approach is the fracture mechanics, which has been proven to predict delamination growth effectively while cannot be applied without an initial crack [44]. Also, some methods combining a stress analysis for the delamination onset and fracture mechanics for the delamination growth are proposed [45,46].

Compared with alternative approaches, cohesive zone modeling offer the advantages of encompassing both crack initiation and propagation. It also provides the ability to model multiple crack paths without crack-path following algorithms since the cracks can propagate potentially along any path where cohesive elements are placed [47].

In this study, cohesive zone method is utilized for prediction of delamination in ta-

pered composite laminates. A brief theoretical background of cohesive zone modeling is presented in following section.

2.2.1 Cohesive Zone Modeling

The behavior of cohesive elements is governed by a Traction-Separation Law (TSL), which relates the traction to nodal displacements. Several TSLs are proposed in the literature with various considerations. Comprehensive discussions on various constitutive models and traction-separation laws for CZM are presented in [48, 49]. In this study, Bi-linear Traction-Separation Law [5] is used as the governing behavior which is shown in Fig. 2.2 for a pure or single mode of loading.

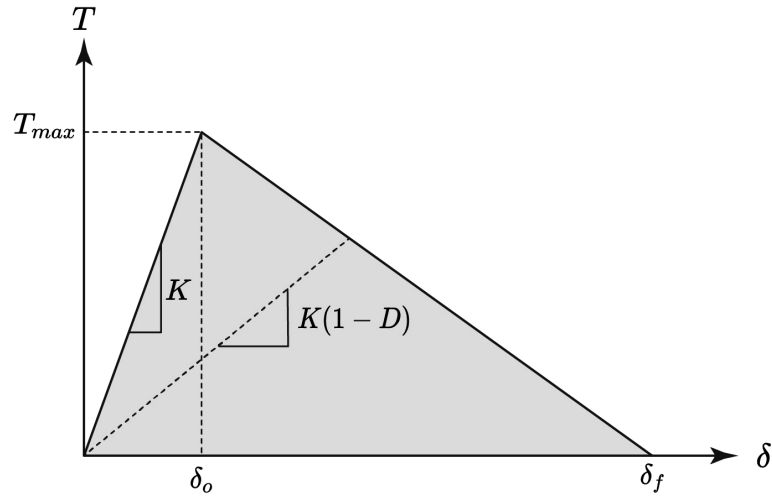


Figure 2.2: Bi-Linear traction separation law for a single-mode of loading [5].

Bi-linear traction-separation law is characterized basically by two material parameters; interlaminar strength and fracture toughness. It starts with an initial linear elastic region until it reaches the interlaminar strength. Right after that point, a linear softening region starts where the element stiffness decreases until the element is fully degraded. The rate of material stiffness degradation is correlated with the area under the curve, which corresponds to the interface fracture toughness, G_c . Three different fracture modes, Mode I (opening), Mode II (in-plane shear), and Mode III (out-of-plane) or combination of these modes (mixed mode) are considered in delamination of composite laminates (Fig. 2.3).

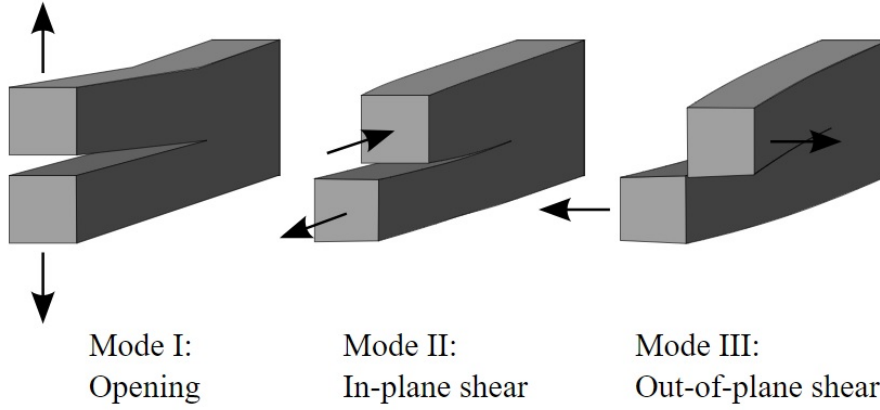


Figure 2.3: Definition of Mode I (normal opening), Mode II (in plane shearing) and Mode III (out-of-plane shearing).

For a specific material, the fracture toughness and interlaminar strength values in a single loading mode can be measured by conducting standard tests. Double Cantilever Beam (DCB) [50] and End Notched Flexure (ENF) [51] tests are the methods to determine Mode I and Mode II fracture toughness values, respectively. Also, Interlaminar Tensile Strength (ILTS) and Interlaminar Shear Strength (ILSS) values can be measured by Curved Beam Specimen (CBS) [52], and Short-Beam Strength test [53].

For a pure mode loading case, the material degradation of a cohesive element is represented by a damage variable as given by [54]:

$$D = \frac{\delta^f(\delta - \delta^0)}{\delta(\delta^f - \delta^0)} \quad (2.1)$$

where the damage variable " D " is equal to zero before damage initiation, unity in full degradation, and varies in between. For mixed-mode loading cases as in tapered laminates, an interaction criterion considering different delamination modes must be included for both damage initiation and progression [6]. The way that these interactions are taken into account is shown in Fig. 2.4.

Camanho et. al [55] suggested an effective displacement for the combination of nor-

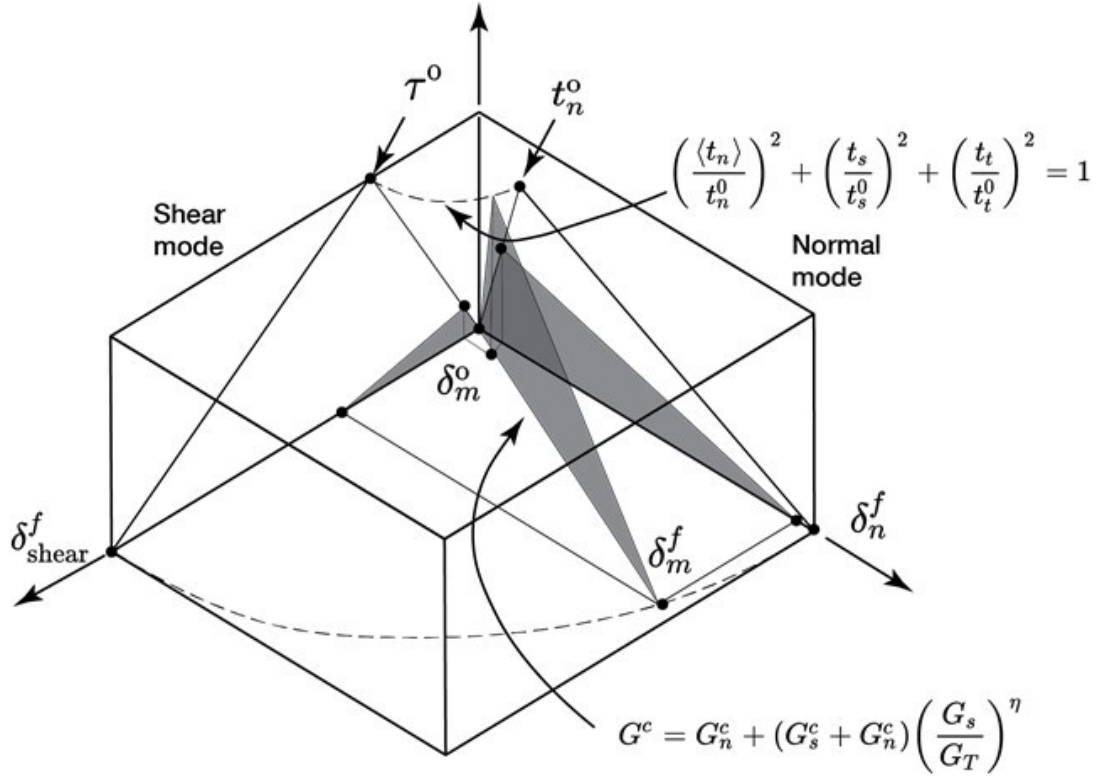


Figure 2.4: Bi-Linear traction separation law for a mixed-mode loading case [5].

mal and shear deformations across the cohesive interface as:

$$\delta_m = \sqrt{\langle \delta_n \rangle^2 + \delta_s^2 + \delta_t^2} \quad (2.2)$$

Thus, the damage variable for a mixed-mode loading takes the following form:

$$D = \frac{\delta_m^f (\delta_m - \delta_m^0)}{\delta_m (\delta_m^f - \delta_m^0)} \quad (2.3)$$

where δ_m , δ_m^0 and δ_m^f are effective displacements at damage initiation, current state and final failure, respectively. The effective displacement value at the final failure can be obtained from:

$$\delta_m^f = \frac{2G_c}{T_{eff}} \quad (2.4)$$

where G_c and T_{eff} are mixed-mode fracture toughness and effective traction at dam-

age initiation, respectively. These values are dependent to the criteria used for mixed mode damage initiation and propagation. Various criteria are proposed for effective traction in damage initiation and mixed mode fracture toughness in literature [56].

In this study, the quadratic nominal stress criterion is used for the damage initiation. According to this criterion, it is assumed that the delamination onset happens when the following equation is satisfied [57]:

$$\left\{ \frac{\langle t_n \rangle}{t_n^0} \right\}^2 + \left\{ \frac{t_s}{t_s^0} \right\}^2 + \left\{ \frac{t_t^0}{t_t^0} \right\}^2 = 1 \quad (2.5)$$

where t_n^0 , t_s^0 and t_t^0 represent the maximum values of nominal stresses for pure deformation cases of normal to the interface, first and the second shear directions, respectively. The symbol, $\langle \dots \rangle$, is the McCauley brackets operator, which signifies that no damage initiates due to pure compression.

The critical Energy Release Rate (ERR) for delamination, G_c , is calculated according to the Mixed-Mode Benzaggah-Kenane (B-K) criterion [58]:

$$G_{IC} + (G_{IIC} - G_{IC}) \left(\frac{G_{II} + G_{III}}{G_I + G_{II} + G_{III}} \right)^\eta = G_c \quad (2.6)$$

where G_I and G_{II} are energy release rates and G_{IC} and G_{IIC} critical energy release rates for Mode I and Mode II, respectively.

2.2.2 Cohesive Zone Parameters

Some limitations and considerations should be taken into account in implementing the cohesive zone method in finite element analyses. The results obtained by CZM can be highly affected by parameters such as element size, penalty stiffness, and interface properties. The limitation related to the mesh size is one of the most significant problems of the CZM. To conduct accurate delamination analyses, sufficiently fine mesh is required to ensure that enough elements exist within the cohesive zone length (L_{cz}). L_{cz} is defined as the region along the crack path where interfacial tractions increase to the maximum interfacial strength some distance ahead of the crack tip.

The length of the cohesive zone reaches a maximum ($L_{cz,f}$) at the point where the crack tip interface element completely fails (Fig. 2.5).

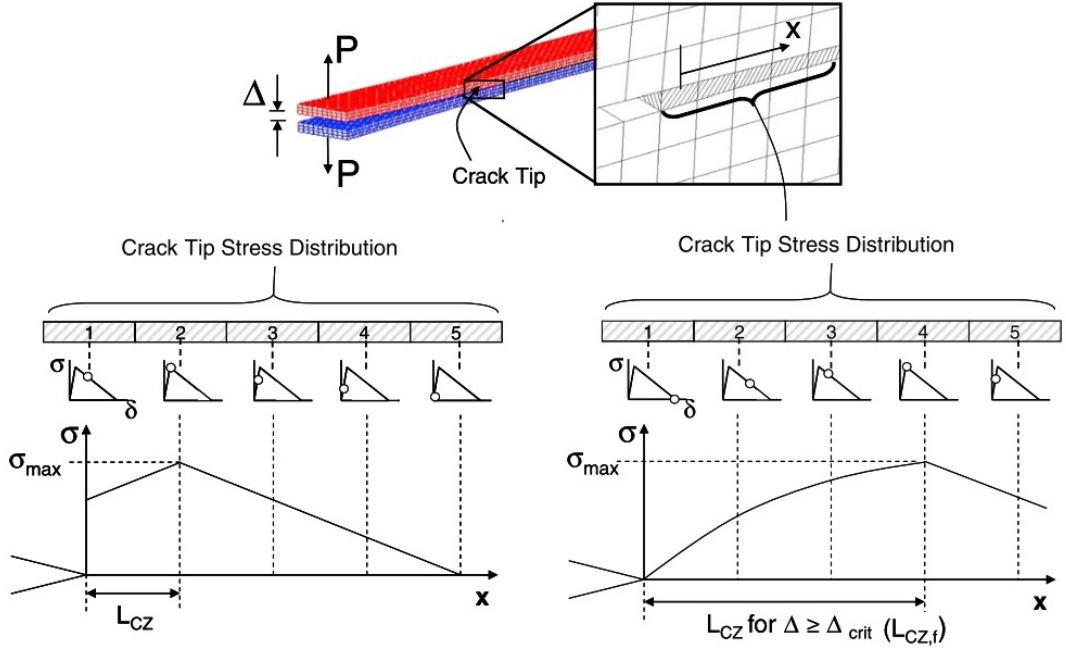


Figure 2.5: Development of damage in elements within cohesive zone length [6].

The selection of appropriate mesh size relies on the accurate prediction of both cohesive zone length and the minimum number of interface elements within this region. Depending on the loading mode, some researchers have proposed different formulations to calculate cohesive zone length [6,59–61]. For example, (L_{cz}) for Mode I [61] and Mode II [62] loading for an orthotropic material can be calculated by:

$$l_{ch,I} = E'_I \frac{G_{IC}}{(\sigma_{I,max})^2} \quad (2.7a)$$

$$l_{ch,II} = E'_{II} \frac{G_{IIC}}{(\sigma_{II,max})^2} \quad (2.7b)$$

Where E'_I and E'_{II} are equivalent elastic moduli of the material. Cox and Yang suggest a modified forms Eqs. 2.7a and 2.7b for estimating cohesive zone length in slender laminates under mode I and mode II loading, respectively [61]:

$$l_{ch,slender,I} = \left(E'_I \frac{G_{IC}}{(\sigma_{I,max})^2} \right)^{\frac{1}{4}} h^{\frac{3}{4}} \quad (2.8a)$$

$$l_{ch,slender,II} = \sqrt{\left(E'_{II,slender} \frac{G_{IIC}}{(\sigma_{II,max})^2} \right) h} \quad (2.8b)$$

The number of elements within the cohesive zone length can be shown by [6]:

$$N_{el} = \frac{L_{CZ,f}}{L_{el}} \quad (2.9)$$

The minimum number of three elements in the cohesive zone length is reported to be enough to capture the softening ahead of the crack tip accurately. Harper and Hallett [6] proposed a mesh size selection strategy for a general mixed-mode loading with bi-linear TSL as follows:

- First, predict the minimum length of the fully developed cohesive zone length using:

$$L_{CZ,f,predicted} = 0.5 [\min(Eqs.2.7a, 2.7b, 2.8a, 2.8b)] \quad (2.10)$$

- Then divide this length by 3 to calculate the maximum allowable element length:

$$L_{el,max} = \frac{L_{CZ,f,predicted}}{3} \quad (2.11)$$

Another critical parameter in utilizing cohesive elements is the slope of the first part of the traction-separation curve, K , which is shown in Fig. 2.2. Its importance is in ensuring realistic undamaged conditions in the cohesive zone. Insufficient or overestimated penalty stiffnesses lead to unrealistic results due to problems such as spurious oscillations of the tractions in an element or large displacements in cohesive interfaces [63]. Turon et.al [60] derived a relation for penalty stiffness as:

$$K = \alpha \frac{E_3}{t} \quad (2.12)$$

where α is a parameter ($\alpha \gg 1$). Selecting values greater than 50 leads to sufficiently accurate results for most problems.

2.3 Intralaminar Damage

Due to heterogeneity and isotropic nature of composites, damage mechanism in these structures are very complicated. Studies on understanding the damage mechanisms

and development of modeling techniques to effectively estimate their failure behavior are still in progress. In addition to these complexities, highly localized stresses and complicated load distribution in the tapered region make the damage analysis in such structures complicated compared to laminates of constant thickness. The onset of intralaminar failure mechanisms is generally predicted using ply-based failure criteria and applying appropriate damage evolution models.

This section presents the continuum damage model used to simulate ply damage in this study and its implementation method in finite element analyses.

2.3.1 Constitutive Damage Model

Using the three-dimensional version of ply complementary free energy density function, the general 3-D stress-strain relationship for an orthotropic composite lamina can be expressed as [64]:

$$\varepsilon = S_d : \sigma \quad (2.13)$$

where S_d is lamina compliance tensor and is defined as:

$$S_d = \begin{bmatrix} \frac{1}{E_1(1-d_f)} & \frac{-\nu_{12}}{E_1} & \frac{-\nu_{13}}{E_1} & 0 & 0 & 0 \\ \frac{-\nu_{12}}{E_1} & \frac{1}{E_2(1-d_m)} & \frac{-\nu_{23}}{E_1} & 0 & 0 & 0 \\ \frac{-\nu_{13}}{E_1} & \frac{-\nu_{23}}{E_1} & \frac{1}{E_3(1-d_m)} & 0 & 0 & 0 \\ 0 & 0 & 0 & \frac{1}{G_{12}(1-d_s)} & 0 & 0 \\ 0 & 0 & 0 & 0 & \frac{1}{G_{13}(1-d_s)} & 0 \\ 0 & 0 & 0 & 0 & 0 & \frac{1}{G_{23}(1-d_s)} \end{bmatrix} \quad (2.14)$$

where d_i represent the damage variable and indices f and m refer to fiber and matrix. It should be noted that, depending on whether the stresses are tensile or compressive the damage variables can be shown by d_{ft} , d_{fc} , d_{mt} and d_{mc} for fiber tensile, fiber compression, matrix tensile and matrix compression, respectively. The 3-D Hashin failure criterion is employed to determine the constituent failure induced composite

damage initiation. The 3-D Hashin criterion distinguishes matrix and fiber failure modes under tension and compression loading cases by the following equations [65].

Fiber tension ($\sigma_{11} \geq 0$) :

$$FI_{ft} = \left(\frac{\sigma_{11}}{X_T} \right)^2 + \alpha \frac{\sigma_{12}^2 + \sigma_{13}^2}{S_{12}^2} \quad (2.15a)$$

Fiber compression ($\sigma_{11} < 0$) :

$$FI_{fc} = \left(\frac{\sigma_{11}}{X_C} \right)^2 \quad (2.15b)$$

Matrix tension ($\sigma_{22} + \sigma_{33} > 0$) :

$$FI_{mt} = \left(\frac{\sigma_{22} + \sigma_{33}}{Y_T} \right)^2 + \frac{\sigma_{12}^2 + \sigma_{13}^2}{S_{12}^2} + \frac{\sigma_{23}^2 - \sigma_{22}\sigma_{33}}{S_{23}^2} \quad (2.15c)$$

Matrix compression ($\sigma_{22} + \sigma_{33} < 0$) :

$$FI_{mc} = \left[\left(\frac{Y_C}{2S_{23}} \right)^2 - 1 \right] \left(\frac{\sigma_{22} + \sigma_{33}}{Y_C} \right) + \frac{(\sigma_{22} + \sigma_{33})^2}{4S_{23}^2} + \frac{\sigma_{23}^2 - \sigma_{22}\sigma_{33}}{S_{23}^2} + \frac{\sigma_{12}^2 + \sigma_{13}^2}{S_{12}^2} \quad (2.15d)$$

where X_T , X_C , Y_T , Y_C , S_{12} , S_{13} , S_{23} are longitudinal tensile strength, longitudinal compressive strength, transverse tensile strength, transverse compressive strength, in-plane shear strength, and out-of-plane shear strength, respectively. FI_i is the corresponding failure index for each failure mode and α is the interaction coefficient of shear stresses on fiber tensile strength. This coefficient can be determined experimentally and is taken 0 in this study. Damage initiates when the value of each index reaches unity.

2.3.2 Damage Evolution

Once the damage initiation criterion is satisfied the material properties are degraded according to degradation or softening model. Damage evolution is modeled by a linear softening response with equivalent stress-strain approach shown in Fig. 2.6.

A characteristic element length L^c , is introduced such that the total amount of energy dissipated during failure in a continuum element is equal to the fracture toughness defined for a cohesive element of the same size. The area under the curve corresponds

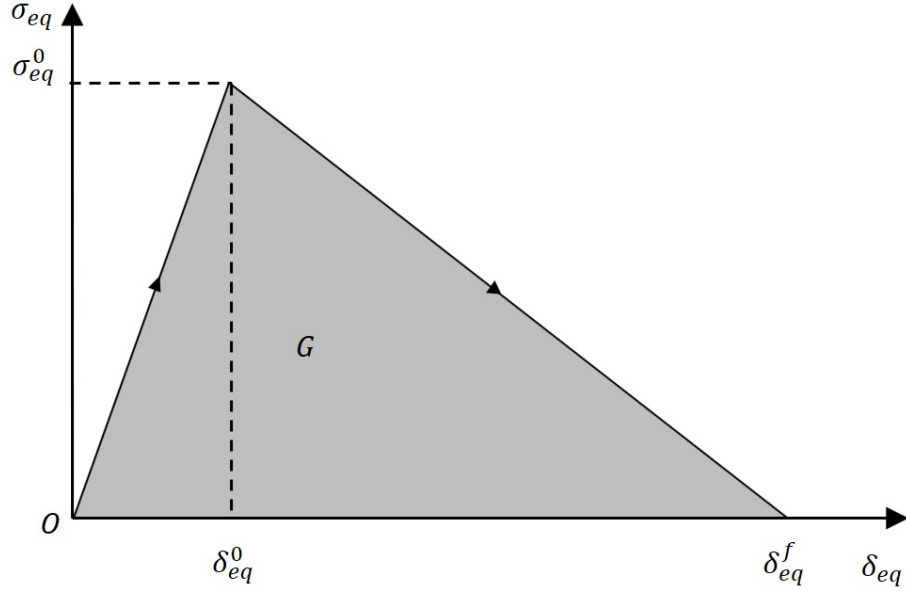


Figure 2.6: Linear Softening model.

to the energy dissipation due to each corresponding failure mode for an element with a characteristic length of L^c is ([65]):

$$\int \sigma_{eq}^i d(\varepsilon_{eq}^i L^c) = G_i, (i = ft, fc, mt, mc) \quad (2.16)$$

where σ_{eq} and δ_{eq} are equivalent stress and strain, respectively. Also ft , fc , mt and mc superscripts are representative of fiber tension, fiber compression, matrix tension and matrix compression, respectively.

The equivalent strain and stress for each failure mode can be defined as:

Fiber tension:

$$\varepsilon_{eq}^{ft} = \sqrt{\langle \varepsilon_{11} \rangle^2 + \alpha \varepsilon_{12}^2 + \alpha \varepsilon_{13}^2} \quad (2.17a)$$

$$\sigma_{eq}^{ft} = \frac{\langle \sigma_{11} \rangle \langle \varepsilon_{11} \rangle + \alpha \sigma_{12} \varepsilon_{12} + \alpha \sigma_{13} \varepsilon_{13}}{\varepsilon_{eq}^{ft}} \quad (2.17b)$$

Fiber compression:

$$\varepsilon_{eq}^{fc} = \langle -\varepsilon_{11} \rangle \quad (2.18a)$$

$$\sigma_{eq}^{ft} = \frac{\langle -\sigma_{11} \rangle \langle -\varepsilon_{11} \rangle}{\varepsilon_{eq}^{fc}} \quad (2.18b)$$

Matrix tension:

$$\varepsilon_{eq}^{mt} = \sqrt{\langle \varepsilon_{22} \rangle^2 + \langle \varepsilon_{33} \rangle^2 + \varepsilon_{12}^2 + \varepsilon_{13}^2 + \varepsilon_{23}^2} \quad (2.19a)$$

$$\sigma_{eq}^{mt} = \frac{\langle \sigma_{22} \rangle \langle \varepsilon_{22} \rangle + \langle \sigma_{33} \rangle \langle \varepsilon_{33} \rangle + \sigma_{12} \varepsilon_{12} + \sigma_{13} \varepsilon_{13} + \sigma_{23} \varepsilon_{23}}{\varepsilon_{eq}^{mt}} \quad (2.19b)$$

Matrix compression:

$$\varepsilon_{eq}^{mc} = \sqrt{\langle -\varepsilon_{22} \rangle^2 + \langle -\varepsilon_{33} \rangle^2 + \varepsilon_{12}^2 + \varepsilon_{13}^2 + \varepsilon_{23}^2} \quad (2.20a)$$

$$\sigma_{eq}^{mc} = \frac{\langle -\sigma_{22} \rangle \langle -\varepsilon_{22} \rangle + \langle -\sigma_{33} \rangle \langle -\varepsilon_{33} \rangle + \sigma_{12} \varepsilon_{12} + \sigma_{13} \varepsilon_{13} + \sigma_{23} \varepsilon_{23}}{\varepsilon_{eq}^{mc}} \quad (2.20b)$$

By taking the initial value of 0 for the initial damage and 1 for the complete failure and knowing that $\varepsilon_{eq}^i L^c = \delta_{eq}^i$, the damage variable for a particular mode is derived using Fig. 2.6 as:

$$d = \frac{\delta_{eq}^f (\delta_{eq} - \delta_{eq}^0)}{\delta_{eq} (\delta_{eq}^f - \delta_{eq}^0)} \quad (2.21)$$

where δ_{eq}^0 and δ_{eq}^f are initial equivalent failure displacement at the damage onset and ultimate equivalent failure displacement for each failure mode.

2.3.3 Single-Element Test of Ply Damage Model

The ply damage model described in previous section, is implemented via a user defined VUMAT subroutine code written in Fortran. The flowchart for the VUMAT is shown in Fig. 2.7.

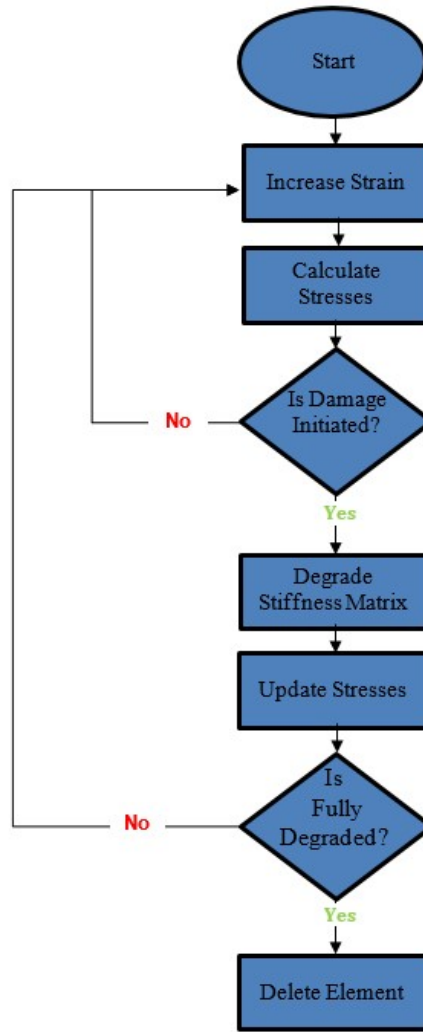


Figure 2.7: Flowchart of VUMAT code.

To resolve the possible errors and evaluate the ply damage model, a single element test is carried out. A single element model with a side length of 1 mm is created and analyzed in Abaqus/Explicit. The principal material directions 1, 2, and 3 are assigned to coincide with local x, y and z coordinates, respectively.

Symmetry boundary conditions in X , Y , and Z directions are assigned to the surfaces with normal vectors in $-X$, $-Y$, and $-Z$ directions, and displacement control fiber tension, fiber compression, matrix tension, and matrix compression loading cases are applied to the single element. The boundary conditions and loading of single element fiber tension and matrix tension cases are shown in Fig. 2.8.

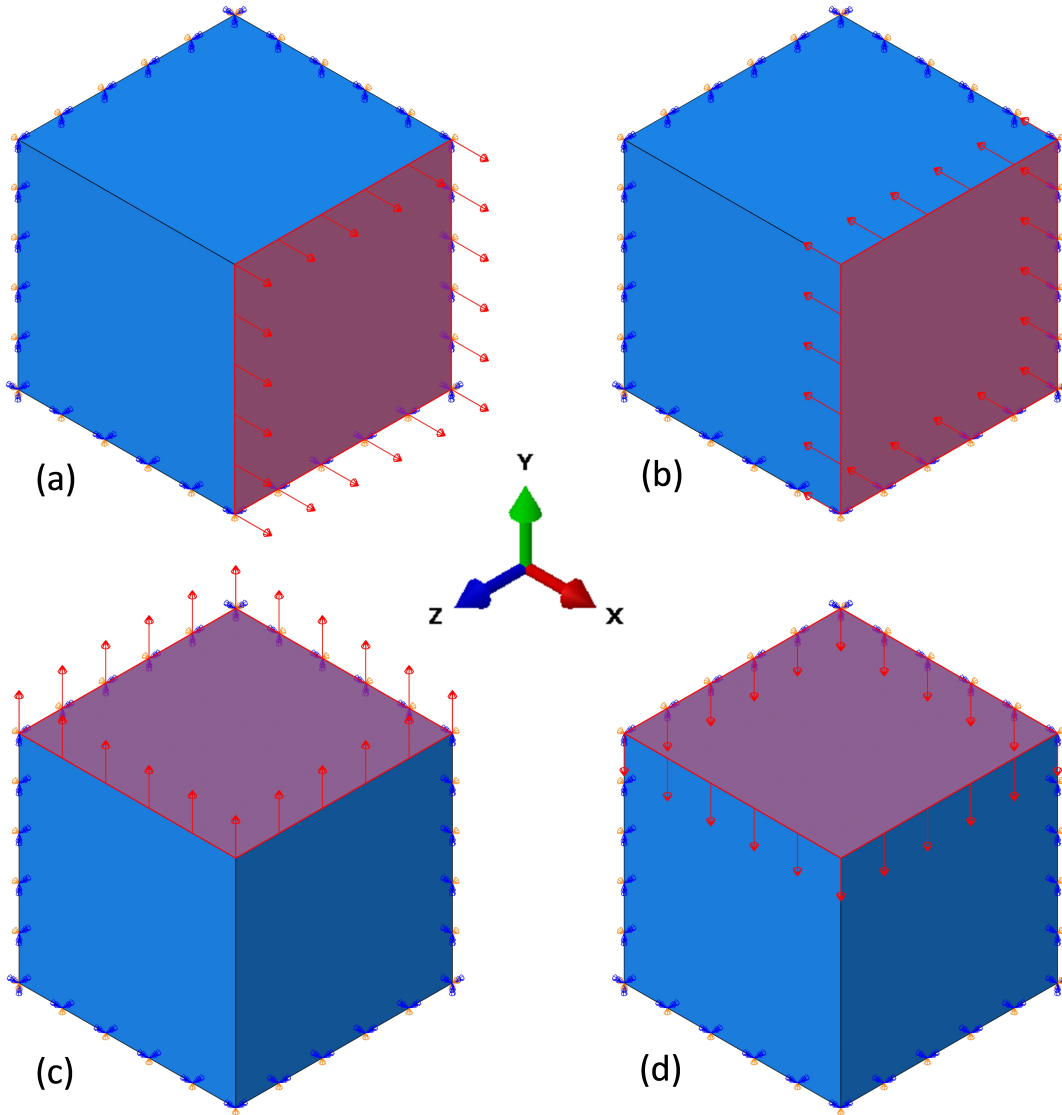
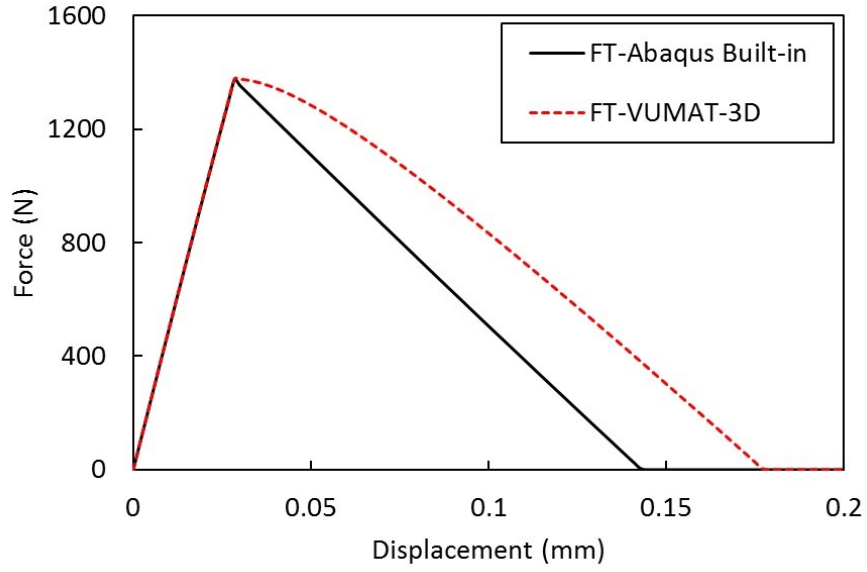


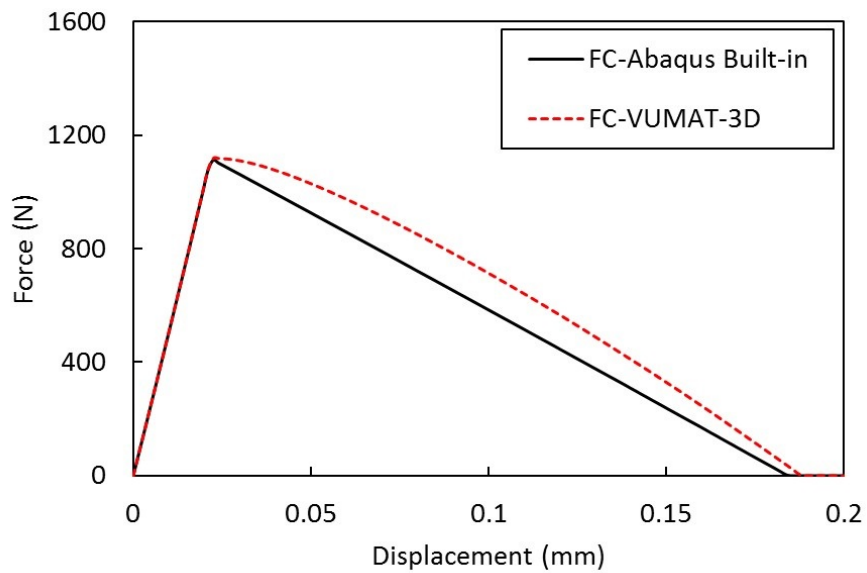
Figure 2.8: Loading and boundary conditions of single element test for (a) fiber tension (b) fiber compression (c) matrix tension and (d) matrix compression.

The load-displacement curves of single element test is compared to Abaqus built-in Hashin failure model under tension and compression loading for matrix and fiber damages and are shown in Figs. 2.9 and 2.10, respectively.

As shown in these figures, the damage initiation calculated by VUMAT for each failure mode is entirely the same as Abaqus built-in Hashin damage model. However, there are some differences in final failure displacement, mainly due to the 3-D nature of the implemented model and taking the stresses in the z-direction taking into ac-



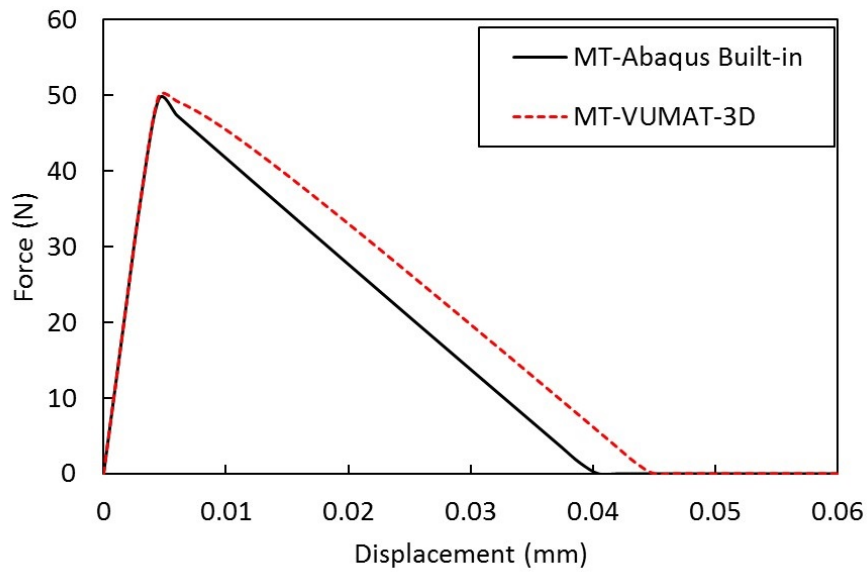
(a)



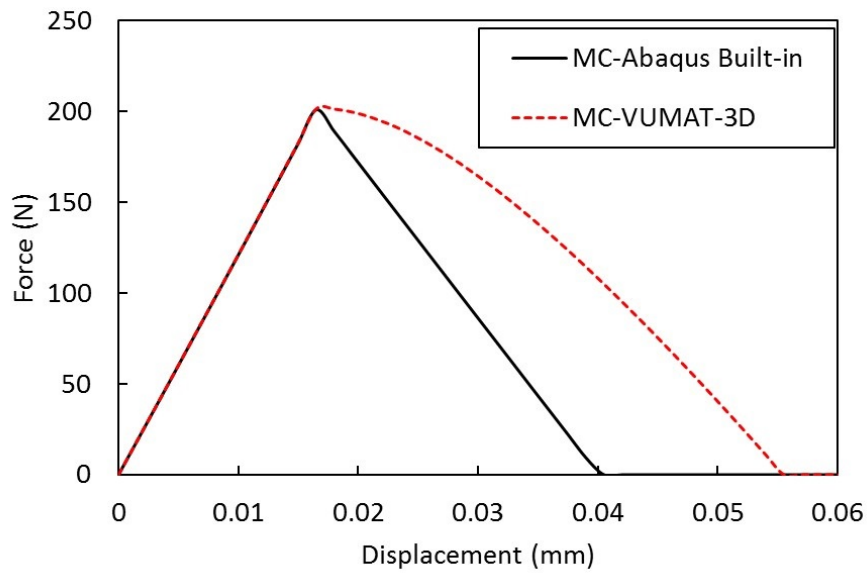
(b)

Figure 2.9: Load-displacement diagrams of single-element test for fiber damage in: (a) tension, (b) compression.

count. This leads to different values for equivalent stresses and strains. Noting that identical fracture energies are used in both implemented VUMAT and Abaqus built-in Hashin model, the calculated δ_{eq}^f in Eqn. 2.21 will also be changed.



(a)



(b)

Figure 2.10: Load-displacement diagrams of single-element test for matrix damage in: (a) tension, (b) compression.

CHAPTER 3

VERIFICATION STUDY

3.1 Introduction

To validate the finite element model described in Chapter 2 the experimental results of a research project is used. The experimental study is a part of DKTM 2015-5 project and is carried out in Structures and Materials Laboratories in Center For Wind Energy, "METUWIND" in Middle East Technical University. In this chapter, the details of the specimens and corresponding finite element model used in the simulations are presented.

3.2 Experimental Procedure and Specimens Specifications

Five different types of asymmetric tapered specimens with different drop-off methods and layups are manufactured from HexPly S2-Glass / 913 UD prepregs. The specimens are composed of 18 plies in the thick section and 12 plies in the thin section with 6 drop-offs. The thickness ratio of thick and thin sections is 3 : 2 with a taper angle of approximately 9.5° for all specimens. The nominal ply thickness and resin pocket lengths are 0.25 mm and 1.50 mm, respectively. Therefore, the nominal thickness of specimens are reduced from 4.5 mm in the thick section into 3 mm in the thin section with tapered region length of 9 mm. The drop-off method in the tapered section of each configuration is shown in Fig. 3.1a, schematically. In this figures, layups in thick section of each laminate is also presented. The underlined angels represent dropped plies in the laminate.

In configurations U-1 and U-2, the plies are terminated consecutively and no con-

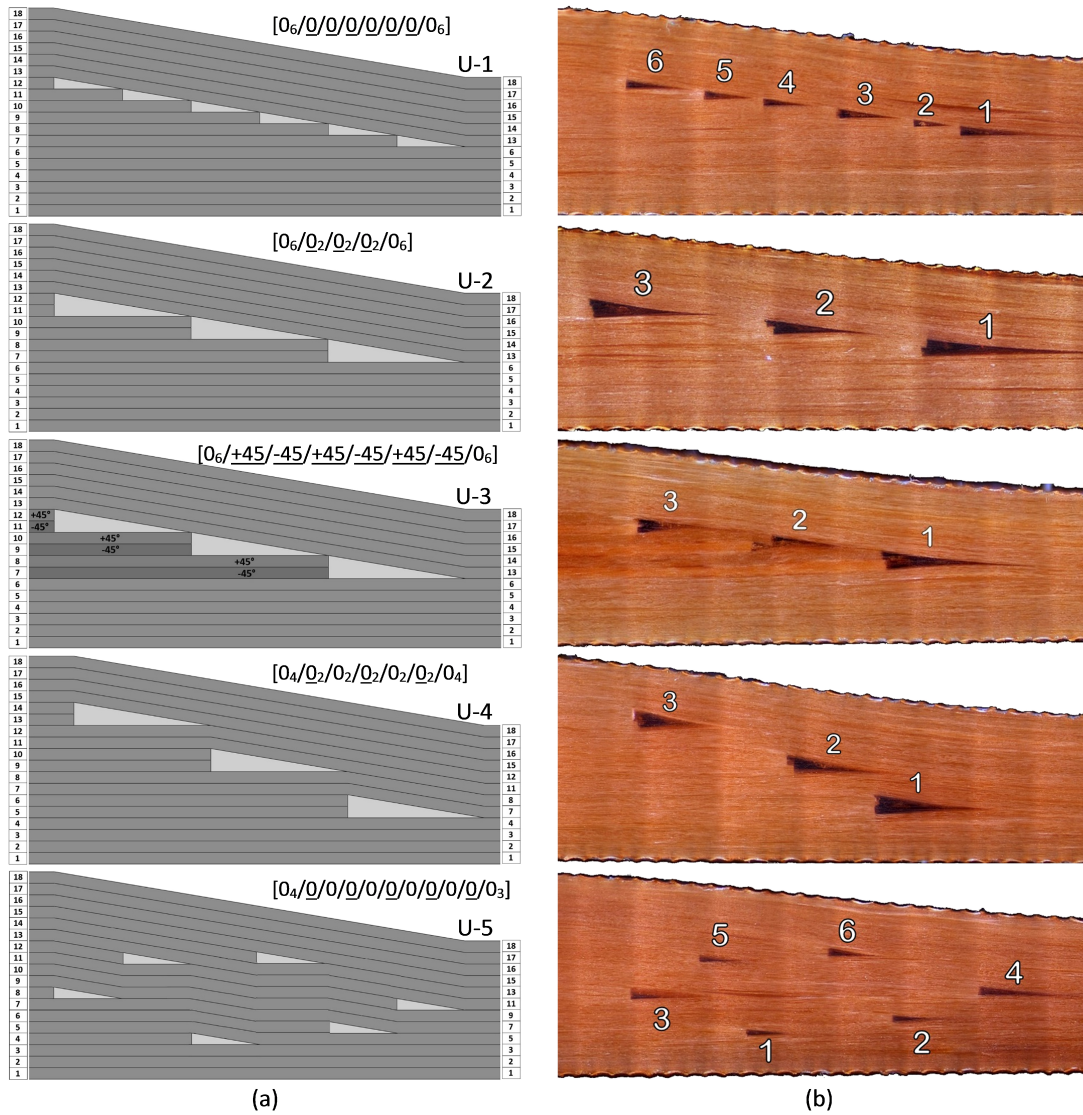


Figure 3.1: (a) Tapered geometry for each configuration and designation, (b) corresponding micro-graphs of test specimens.

tinuous ply exist between dropped plies. One and two plies are terminated in each drop-off location for case U-1 and U-2, respectively. Only 0° plies are used for these specimen configurations. Drop-off method in configuration U-3 is the same as U-2, but $+45^\circ$ and -45° plies are used as drop-offs. In specimen U-4, each pair of dropped plies is followed by two continuous layers. Finally, in configuration U-5, a drop-off layer is followed by a continuous ply in a way that the resin pockets lay in a trapezoidal order.

For the manufacturing of the specimens asymmetrically, tapered laminates are laid on

a flat die assuring that one face of the beam is constrained to be flat, and inherently, the other face is tapered. On one side of the specimen, tabs (S2-glass woven fabric stacked in $\pm 45^\circ$ orientations) with 50-mm length are laid on the tapered side of the laminate to have equal thicknesses at both ends. After the autoclave curing, tabs that are produced separately and bonded on the flat surface. Finally, three specimens with dimensions of 209 mm \times 25 mm are cut by a diamond cutter. The nominal dimensions and geometry of the specimens are shown in Fig. 3.2, schematically.

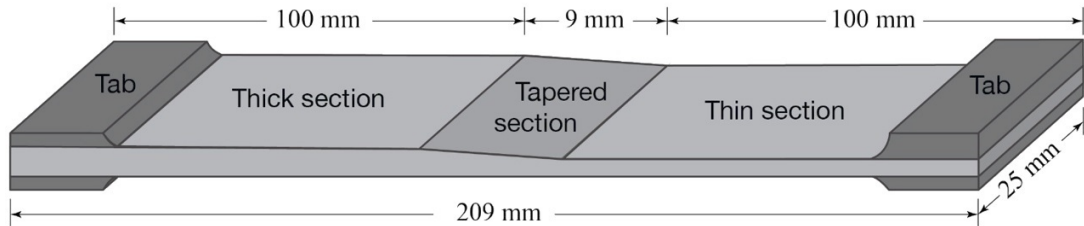


Figure 3.2: Geometry and dimensions of specimens.

Before experiments, the sides of each specimens are polished to provide better visualization for the detection of any manufacturing-related defects, and for any microscopic investigation before testing. It is also necessary for the high-speed camera recording during the tests. Tapered section micrographs of intact specimens are shown in Fig. 3.1b where resin pocket regions can be observed. They are formed by dropping of neighboring plies. No major defect is observed in these micrographs. Comparing the micrographs of intact specimens in Fig. 3.1b to idealized finite element geometry in Fig. 1.2a, some differences can be identified. First, the thickness variation and taper angle are smoother and smaller in manufactured specimens. Second, the geometry, size and distance of the resin pockets from each other are not completely even. Finally, a relatively small thinning occurs at the end of drop-offs behind resin pockets.

Static tensile tests are conducted in an MTS universal servo-hydraulic testing machine with 250 kN capacity and a displacement control system. During the experimental program, grip pressures varying between 20-25 MPa are applied to prevent sliding. Tests are carried out with a loading rate of 0.5 mm/min and displacement is applied via the vertical motion of the lower grip while the upper grip is held fixed. Failure events are recorded from one side via Photron SA5 ultra-high-speed camera

at capturing rates of 124,000 fps.

Digital image correlation (DIC) analyses are conducted in the experiments of configuration U-1 on the tapered face to measure the deformation and strain along the specimen. Also, since the stiffnesses of the specimens are comparable to that of the testing machine, data obtained from the cross-head may not be identical to the elongation of the specimen. Therefore, real deformation fields obtained from DIC analysis are used to interpret the results. Experiments are recorded at a rate of 1 Hz via a 1MP camera with a resolution of 1024 pixels pixels. All analyses are conducted using NCORR, which is an open DIC tool developed in the MATLAB environment. In the calculations, the subset radius is set to be 20 pixels with 5 pixels travel size. The radius used in strain computation is set to 15 pixels. The experimental setup is shown in Fig. 3.3.

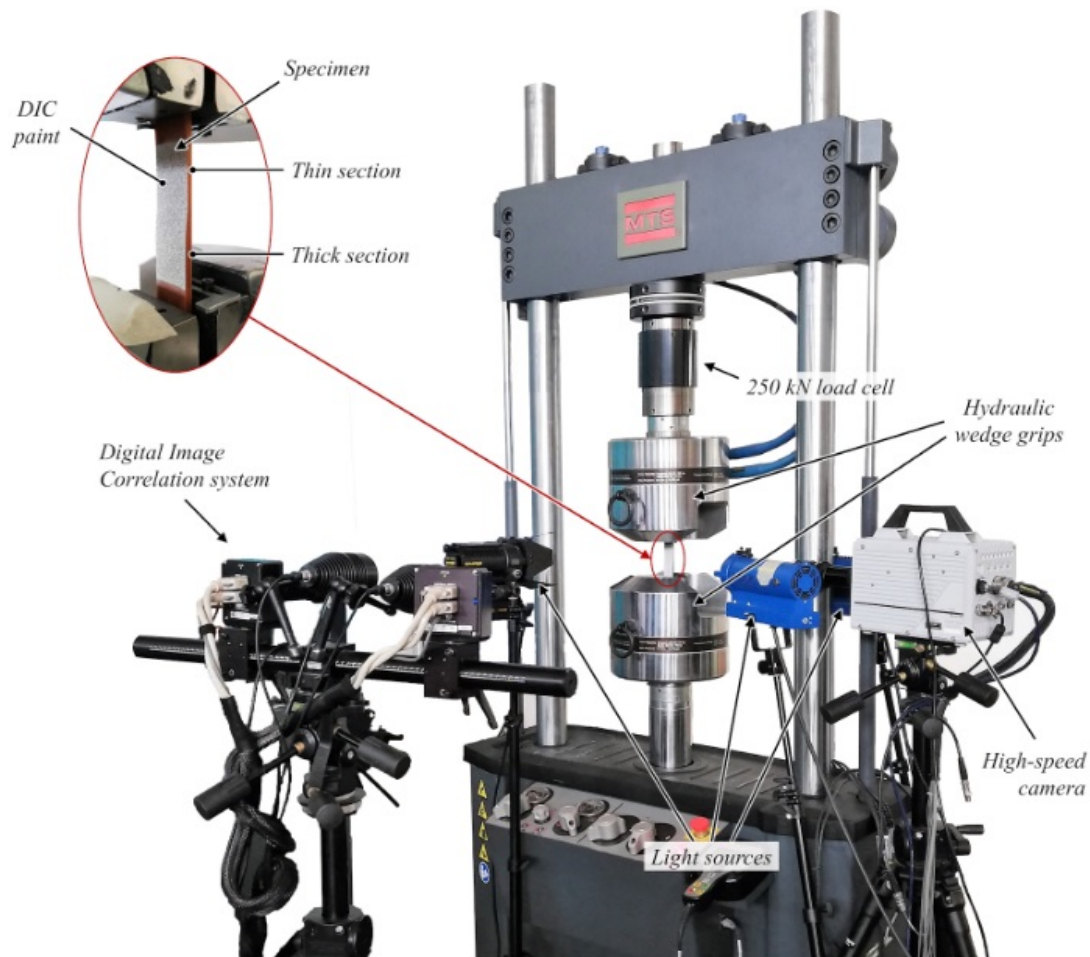


Figure 3.3: Experimental setup.

3.3 Finite Element Modeling

Built-in cohesive elements of Abaqus program are employed to model delaminations. Cohesive elements are placed in all sublaminates/sublaminates, sublaminates/resin pocket, and dropped plies interfaces. No cohesive elements are used between the plies inside the core and belt sublaminates since these interfaces are observed to be less prone to delamination. The interfaces where cohesive elements are inserted for each specimen are shown with red color in Fig. 3.4. For insertion of cohesive elements, the tie-constraint method is used, which has two important advantages. For reliable results, cohesive element formulation requires the use of a fine mesh structure [6]. In the case of the matched mesh, finer mesh requirement for cohesive elements causes surrounding composite plies to also have a finer mesh size, unnecessarily. Tie-constraint, however, allows the use of a finer mesh for the cohesive layer and a coarser mesh for neighboring composite parts. This leads to a considerable saving in computational cost. For tapered laminates and especially for resin pockets, three cohesive layers geometrically coincide at resin pocket corners, where they share a single node. Surface normals of each cohesive layer at these points are different, and this leads to a mathematical singularity which should somehow be handled numerically. One of the methods of eliminating such a problem is the use of tie-constraint and defining separate and independent cohesive layers at such a corner. In Fig. 3.5, a cohesive layer is schematically shown with a finer discretization than the adjacent composite parts which is achieved by tie-constraints.

For composite plies, solid C3D8R elements with an element size of $0.25 \times 0.25 \times 0.25$ mm are utilized. One reason for this selection is the fact that, the upper limit for the thickness of the element should be below the thickness of the nominal ply thickness of 0.25 mm. Also, element thickness smaller than ply thickness is not preferred in this study just to keep computational costs at a reasonable level. For cohesive layers, COH3D8 elements with fixed element lengths of 0.125 mm are selected. Only for vertical interfaces of resin pocket, the element length is selected to be 0.08 mm. They satisfy the cohesive element length conditions as described in [59,60]. For resin pockets, a 6-node linear triangular prism element type (C3D6) is selected. Due to differences in tapered section and number of cohesive layers (Fig. 3.4), the number of elements used in each model is not the same for all specimens. The total number

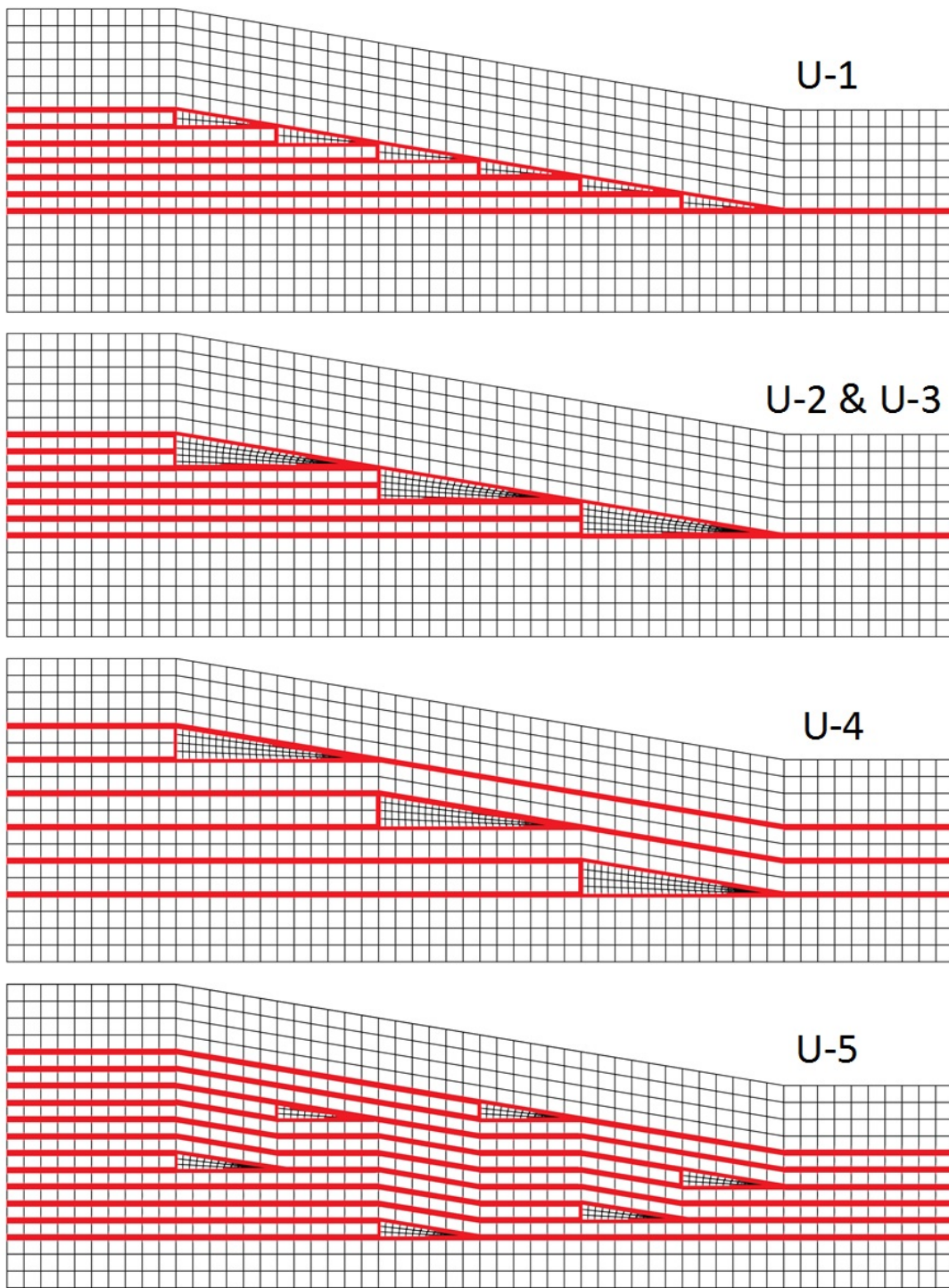


Figure 3.4: Locations of cohesive layers for each specimen type are shown in red color.

of solid and cohesive elements varies between 650400-652200 and 703234-1582434, respectively.

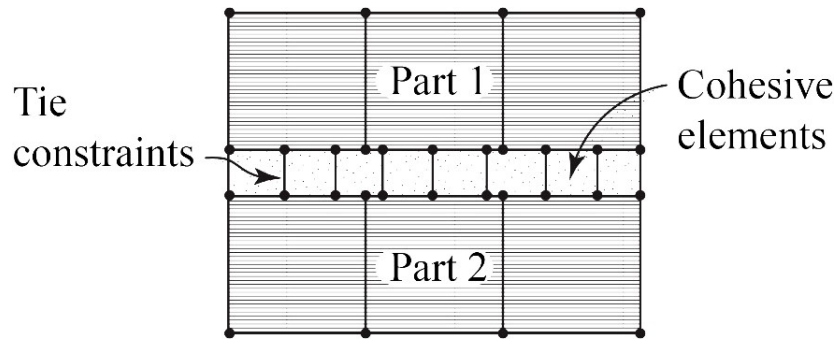


Figure 3.5: Finer cohesive element in tie-constraint method.

The part of geometry between tabs is included in FE model. Tensile displacement loading is applied to tapered specimen models by constraining the thin section and assigning a 3-mm displacement to the thick section as carried out in experiments. The boundary conditions used in FEM is shown in Fig. 3.6.

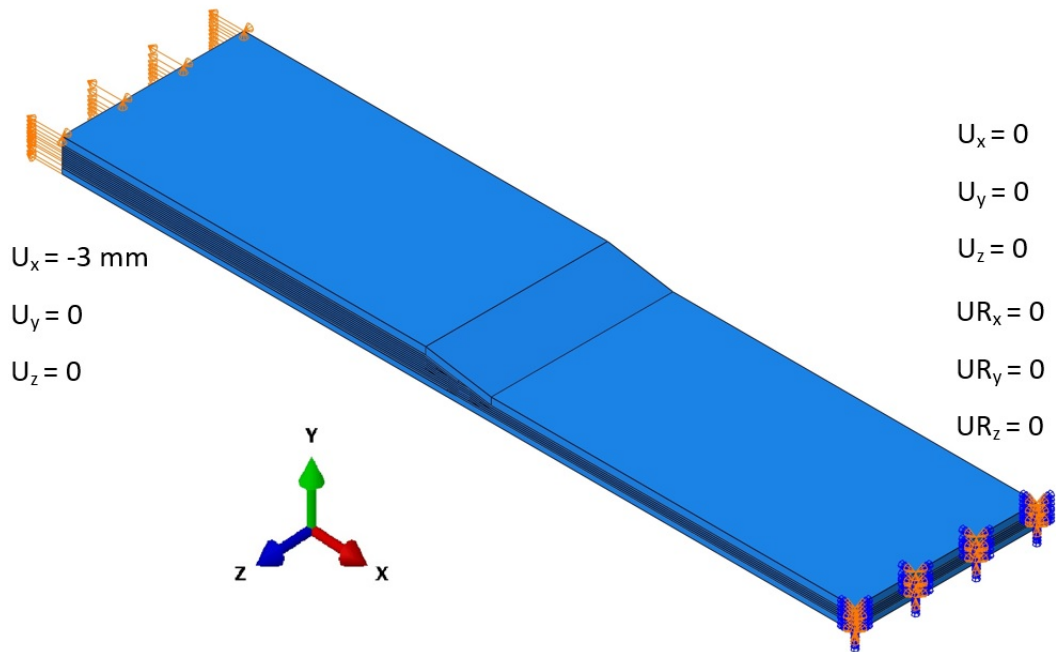


Figure 3.6: Boundary conditions.

The prescribed displacement is applied as a smooth-step [66] to avoid the sudden loading, and its value is obtained by primary simulations, which is calculated to be sufficient enough to make large delaminations.

The rate at which the loading is applied is of great importance in a dynamic FE analysis. Actual time modeling is always favorable; however, the computational time increases by analysis step time in explicit dynamic analyses. Therefore, real time scale modeling is often computationally unaffordable in practice. Increasing stable time increment to reduce computational time can be achieved by mass scaling and increasing the loading rate.

In both methods, inertial forces may become more dominant than the real case and influence the results. The loading rate can be increased by using a shorter step time. The maximum loading rate or minimum step time limit that satisfies quasi-static conditions is calculated as in [67]. The dominant response of a quasi-static analysis is the first structural mode. A modal analysis is carried out, and the first natural frequency and the corresponding time period of the specimen are found to be 209 Hz and 0.00478 seconds. Using the 3-*mm* displacement, the maximum loading rate is calculated by:

$$V = \frac{D}{T} \quad (3.1)$$

Where V , T , and D are loading rate, time period, and displacement boundary condition used in the modeling, respectively, which leads to a maximum loading rate of 0.627 m/s. It is also recommended that the loading speed should not exceed 1% of the wave speed of the material [68]. The wave speeds in fiber, transverse, and shear, in terms of stiffness matrix can be calculated by [69] :

$$c_l^{\parallel} = \left(\frac{c_{11}}{\rho}\right)^{1/2} \quad (3.2)$$

$$c_l^{\perp} = \left(\frac{c_{22}}{\rho}\right)^{1/2} \quad (3.3)$$

$$c_s = \left(\frac{c_{66}}{\rho}\right)^{1/2} \quad (3.4)$$

where c_{11} , c_{22} , and c_{66} are the diagonal components of compliance matrix of the material. Using the material properties in Table. 3.1 leads to 6503 m/s, 1823 m/s,

and 1350 m/s for longitudinal, transverse, and shear wave speeds, respectively. Using the 1% limit for the least value leads to 13.5 m/s, which means selecting a loading rate below this value satisfies the quasi-static conditions. For the displacement of 3 mm in the prescribed boundary conditions, using Eq. 3.1, the shortest step time is calculated to be 0.00022 sec. In order to ensure the quasi-static conditions, a step time of 0.1 s, equivalent to a loading rate of 0.03 m/s, which is more conservative is used in analyses.

Normal and tangential contact interactions are defined between the adjacent layers using the general contact Algorithm of ABAQUS/Explicit to prevent the interpenetration between layers. The FE analyses are performed on a computer consisting of 16 CPU cores. For each configuration, the duration of stimulation varies between about 52 hours (for U-2 and U-3) and 70 hours for U-5.

3.3.1 Material Properties

The mechanical and interface properties are presented in Table 3.1 [1].

Table 3.1: Mechanical and interface properties of Glass/Epoxy [1].

Mechanical Properties					
E_1 (GPa)	$E_2 = E_3$ (GPa)	$G_{12} = G_{13}$ (GPa)	G_{23} (GPa)	$\nu_{12} = \nu_{13}$	ν_{23}
50	12	4	3.3	0.3	0.45
Interface Properties					
G_{Ic} (N/mm)	G_{IIc} (N/mm)	$\sigma_{I_{max}}$ (MPa)	$\sigma_{II_{max}}$ (MPa)	K_I (N/mm ³)	$K_{II} = K_{III}$ (N/mm ³)
1.25	1.248	43	71.2	5.0e5	2.5e5

CHAPTER 4

RESULTS AND DISCUSSIONS FOR VALIDATION STUDY

4.1 Introduction

In this chapter, the finite element results for each specimen configuration are presented and compared to experimental observations. These comparisons are carried out in the terms of the load at delamination onset, delamination locations, and the dynamic characteristics of delamination propagation. Also, a brief discussion on stiffness of the specimens and longitudinal strains are presented.

4.2 Experimental Results

A summary of the experimental results used for the validation of computational study is given in this section. Damage sequences captured by images taken by the high-speed camera and the delamination onset loads of the specimens under tensile loading is considered for comparisons with finite element modeling. The last frame taken before the occurrence of first delamination is considered as the reference frame and is named as $0 \mu s$.

The first four image taken by High-speed camera for specimen U-1 is shown in Fig. 4.1.

The first crack occurs at the back wall of the first resin pocket in which the upcoming delaminations are triggered. Approximately 0.9 seconds after this damage, cracks are also observed at the back walls of the next three resin pockets. Within the next $8.1 \mu s$, two delaminations nucleate from the initial crack at the first resin pocket /

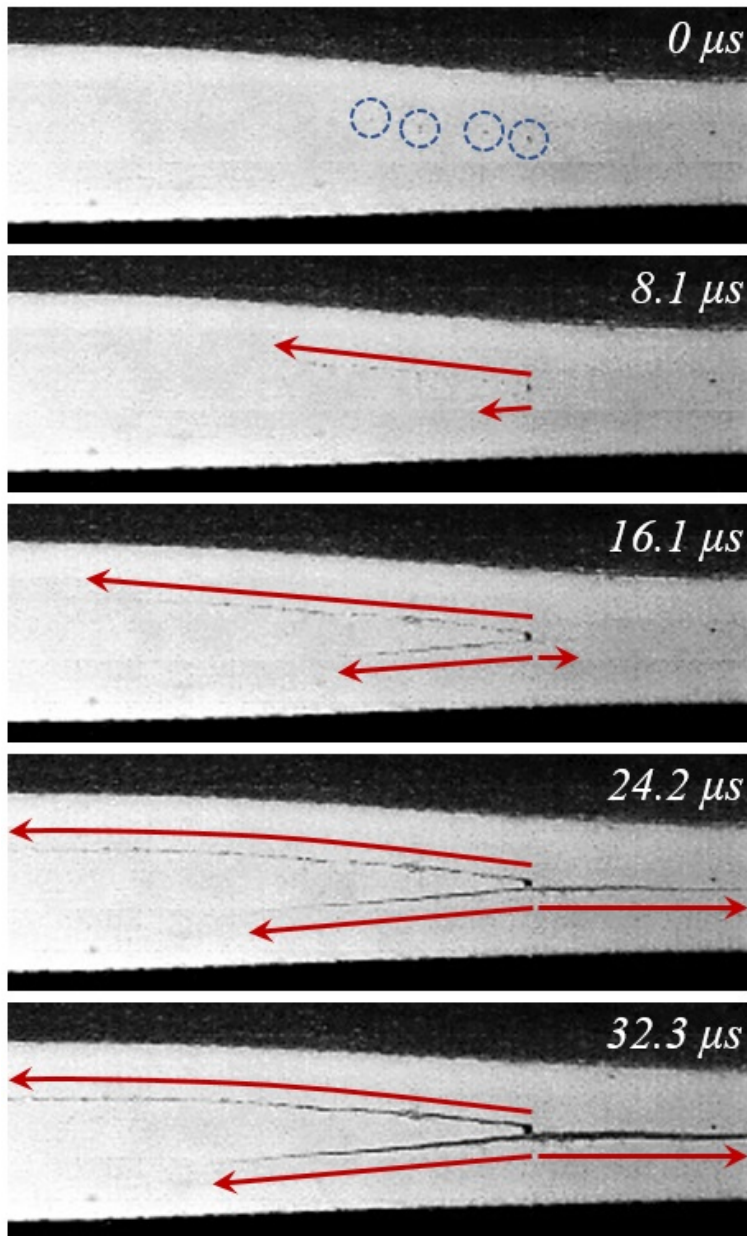


Figure 4.1: High-speed images showing damage sequence in U-1.

lower dropped ply interface are detected at the second resin pocket / belt interface and the first resin pocket / core interface. These delaminations propagate toward the thick section of the laminate. At 16.2 μs , another delamination is nucleated below the first resin pocket, which propagates towards the thin section of the specimen. These delaminations propagate in such a dynamic manner that crack opening modes can be easily recognized at 32.3 μs . Delamination onset load for this specimen is measured to be 45.7 kN and no fiber or matrix failure is observed for this specimen type.

Fig. 4.2 shows the sequence of damage in specimen U-2 taken by high-speed camera images.

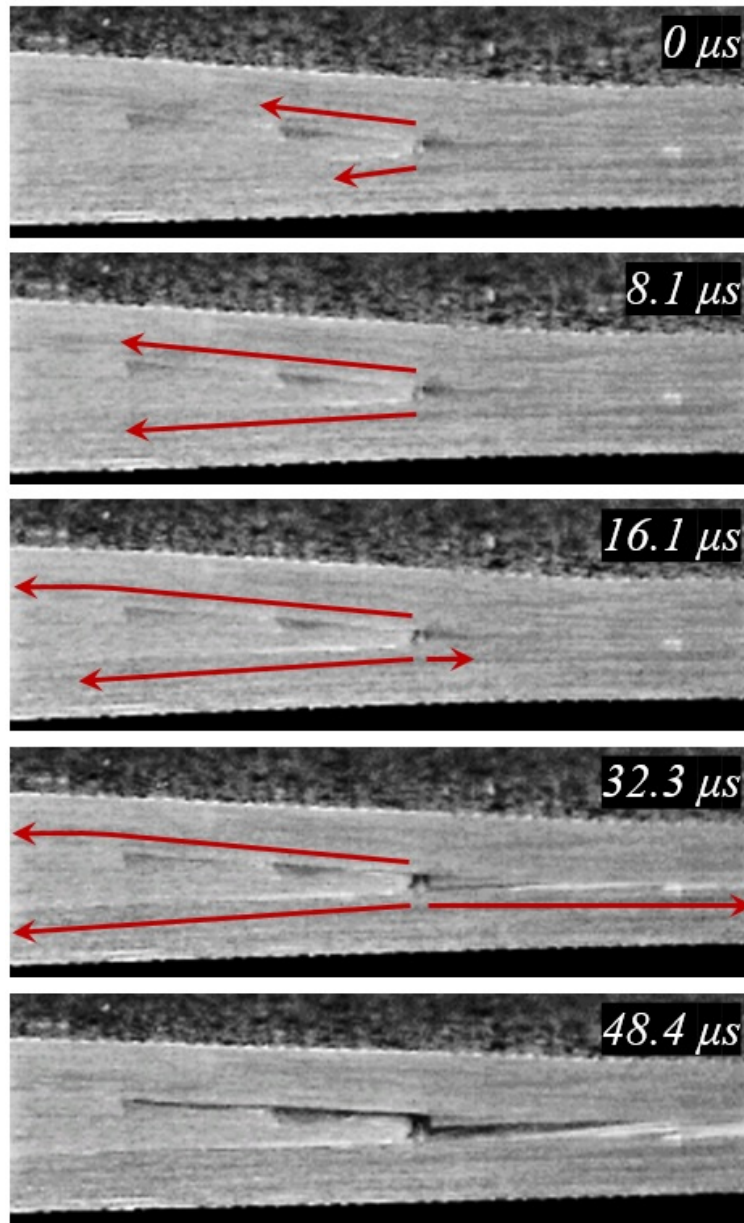


Figure 4.2: High-speed images showing damage sequence in configuration U-2.

A highly dynamic delamination is observed for this configuration. Two delaminations branched from a crack at the vertical interface of the first resin pocket is detectable in the first frame of HSC images. These delaminations are at the belt / dropped plies, and dropped plies / core interfaces and occur at 44.5 kN of the tensile loading. Another delamination initiates at the bottom of the first resin pocket at 16.1 μs. This

crack propagates towards the thin section of the specimen. Within the next $16.1 \mu\text{s}$, these three delaminations fully develop in tapered section of laminate. Delamination openings are easily detectable at $48.4 \mu\text{s}$. Similar to specimen U-2, no in-ply damage is detected for this specimen. However, a vertical crack is observed inside the first resin pocket at delamination initiation.

Configuration U-3, with $\pm 45^\circ$ drop-offs, has a slightly lower stiffness than other configurations. However, the average delamination onset load is considerably higher than in previous cases (84 kN). Images taken by the high-speed camera during the test, showing the sequence of delamination in configurations U-3, are shown in Fig. 4.3.

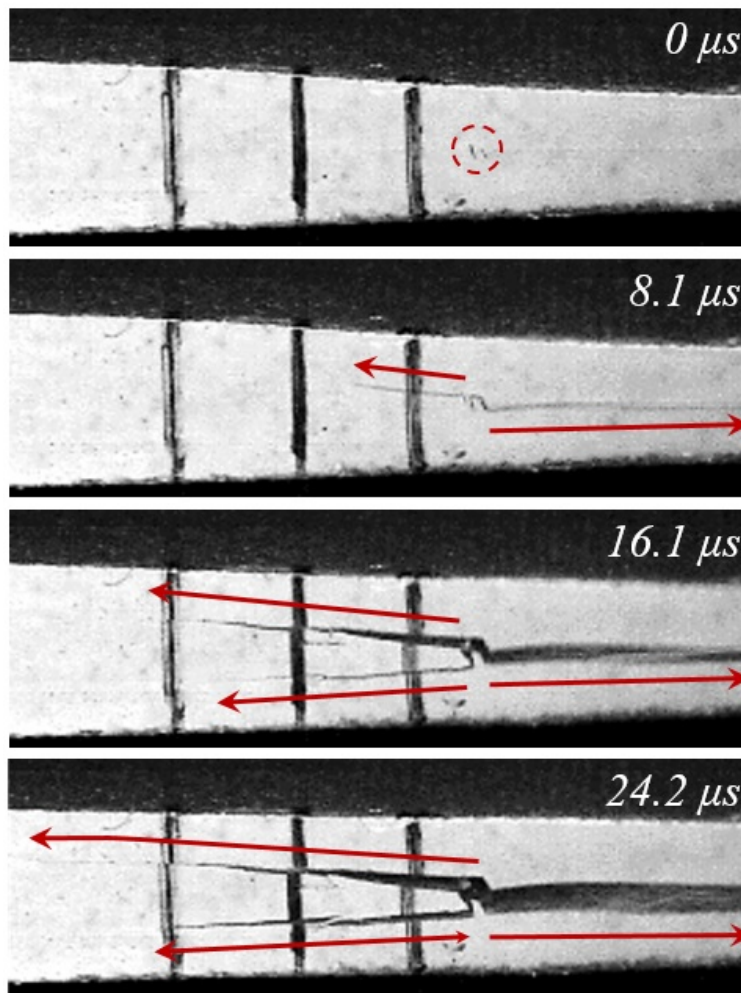


Figure 4.3: High-speed images showing damage sequence in configuration U-3.

For configuration U-3, at $8.1 \mu\text{s}$, two delaminations nucleated by the first resin pocket

are observed in belt / core and belt / resin pocket interfaces propagating toward thin and thick sections. At 16.1 μ s, while these two delaminations grow, the interface between the core and lower dropped ply delaminates, and this delamination propagates towards the thick section. The state of these cracks at 24.2 μ s is shown at the last frame of Fig. 4.3.

In configurations U-1, U-2, and U-3, the plies are terminated consecutively. Audible delamination initiation followed by very dynamic delamination growth is observed in these specimens. However, in Configuration U-4, where two continuous plies exist between two drop-offs, delaminations initiate and propagate in a very different manner. Delamination growth is found to be relatively stable without any opening mode. It makes delamination onset and consequent progression to be very difficult to capture. Therefore, for better illustration, three lines are drawn on the visualized edge of the specimen to track the delamination locations. Discontinuities in these lines represent Mode II delaminations, predominantly. Fig. 4.4a shows the damage sequence for U-4 where the frames are recorded every 10 seconds. Also, for better representation, delaminations are additionally sketched in Fig. 4.4b.

The first frame in this figure is taken approximately at 43.7 kN where three cracks at each resin pocket's back walls are detectable. All vertical black lines are intact, which implies that no delamination is present at this instant. The delaminations propagating towards the thick section are observed in the next frame, at 51.6 kN. Since no image of the damage state could not be captured between these points, the exact delamination loaded could not be determined. As shown in the last frame of Fig. 4.4, six major delamination paths at the top or bottom of the dropped plies are detected for this configuration without fiber or matrix failure up to this stage of loading.

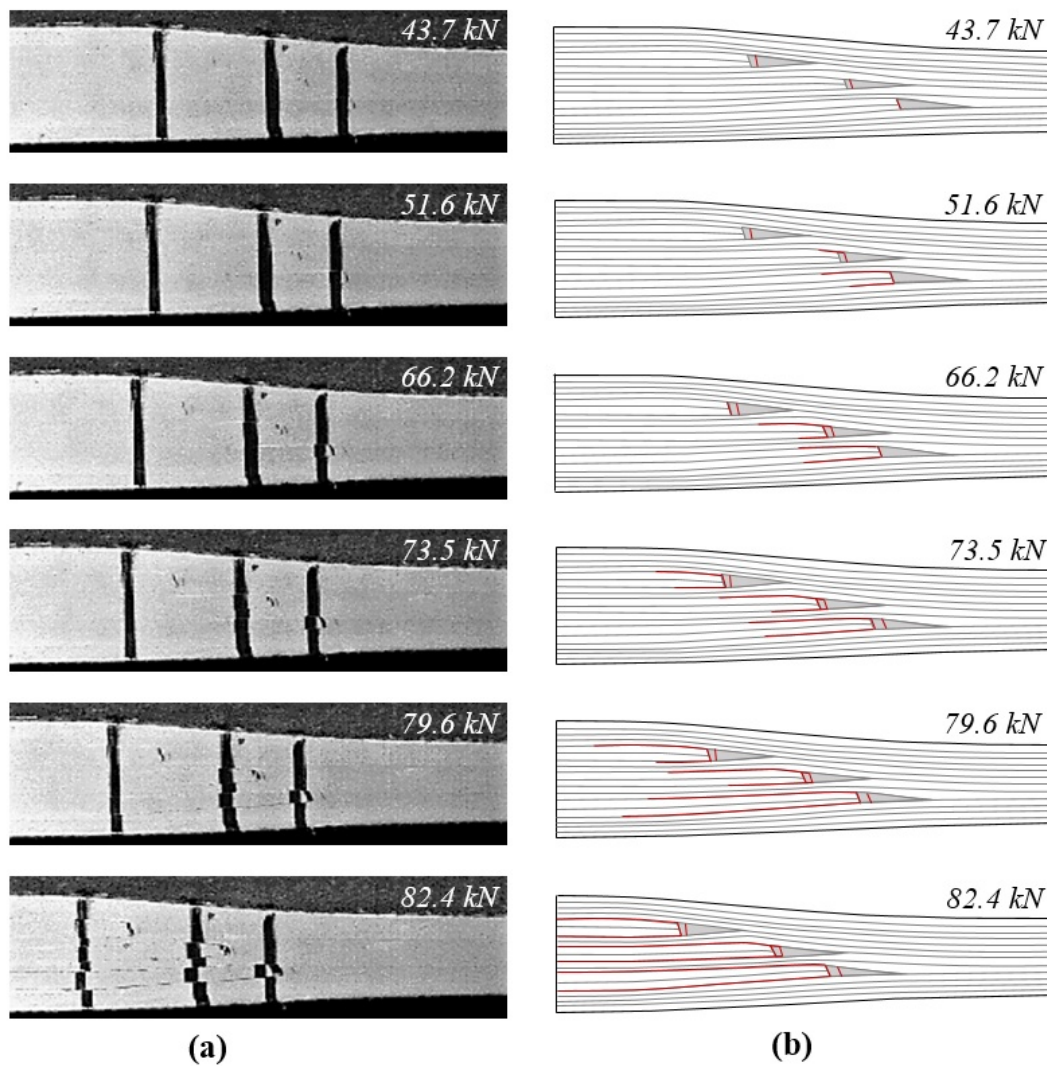


Figure 4.4: High-speed images showing damage sequence in U-4.

Configuration U-5 is tapered with a different drop-off method from previous specimen types. In this specimen, the ply terminations locations lay in a trapezoidal order. Combinations of both stable and unstable delamination growth are observed for this specimen. The first delaminations are detected in the fourth and sixth resin pocket at 70.8 kN of loading. These cracks stably propagate toward thick sections until 84.1 kN. At this instant dynamic failure occurs at the tapered section. The damage sequence for specimen U-8 is shown in Fig. 4.5.

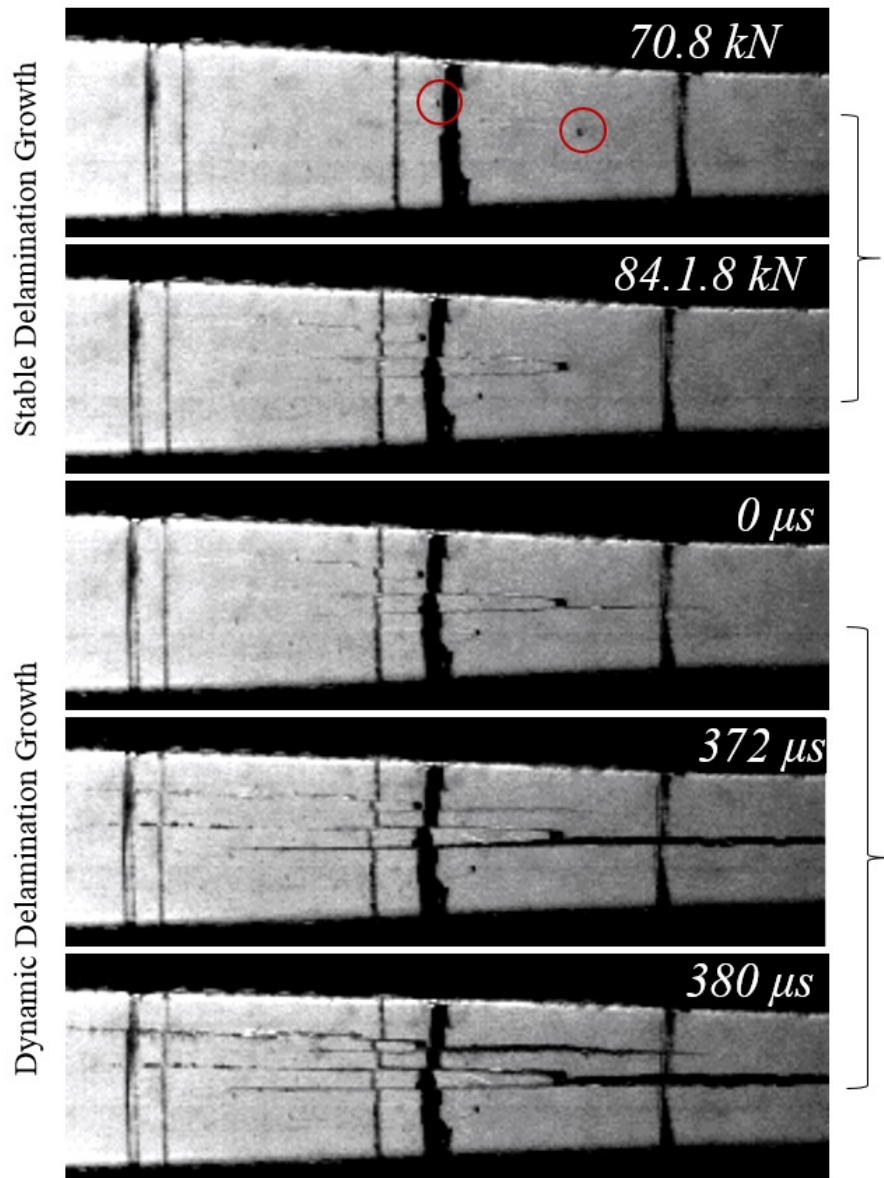


Figure 4.5: Damage sequence in configuration U-5.

4.3 Finite Element Results

The results from finite element analyses for specimens is presented in this section. For better tracking delaminations, laminates are shown here with their outer edges only. The black lines in the following figures represent cohesive elements, and their deletion is representative of the occurrence of delamination in the locations where the elements are deleted. The frame just before the appearance of the first delamination is selected as the time reference.

It should be noted that the damage in the vertical walls of resin pockets is not considered in delamination sequences. The primary analysis revealed that forming a crack in these interfaces does not cause any change in load-displacement curves. In these regions, the resin is in contact with the cut section of the ply. Therefore, a completely different bounding mechanism between resin and fibers exists, making the characterization of interface properties for the resin pocket / dropped ply interface very difficult. However, as shown by experimental observations, they are critical since all the delaminations are triggered in these regions.

In the beginning, to ensure that the effect of inertial forces on the results is limited, the time history of total internal and kinetic energies during the analyses is checked. As previously discussed in Chapter 3, the non-negligible may yield to unrealistic responses in simulation carried out by Abaqus/Explicit. It is recommended that [5], the kinetic energy of the deforming material should not exceed 5% of its internal energy throughout the analysis. However, it should be noted that it is generally impossible to achieve this condition in the early stages of the analysis due to the movement of the deformable body before the development of any significant deformation. As shown in Fig. 4.6, despite a considerable increase of energy after the occurrence of delamination, it is still negligible compared to total internal energy.

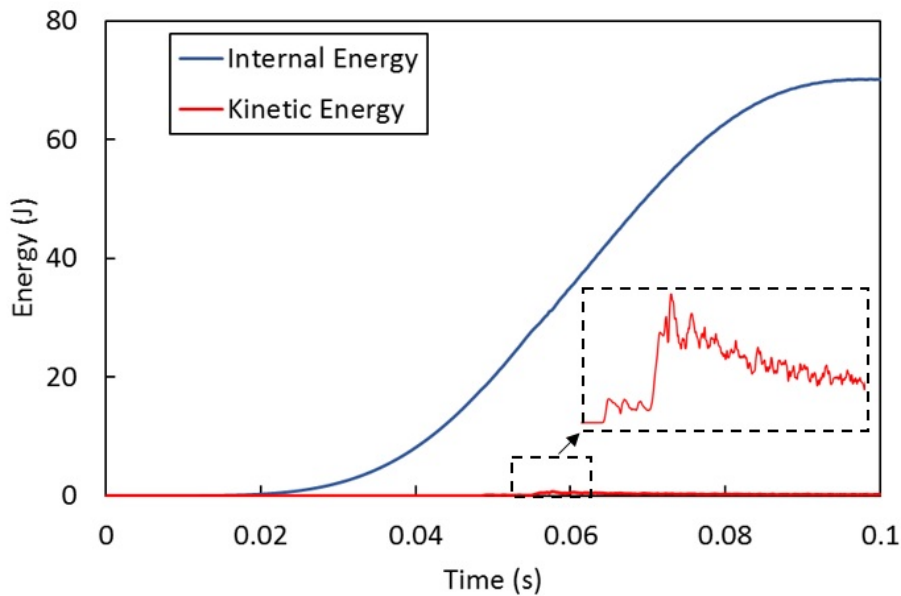


Figure 4.6: Internal and kinetic energy history in Explicit FEA for configuration U-1.

Delamination initiation location and propagation sequence for U-1 configuration obtained from cohesive zone modeling is presented in Fig. 4.7.

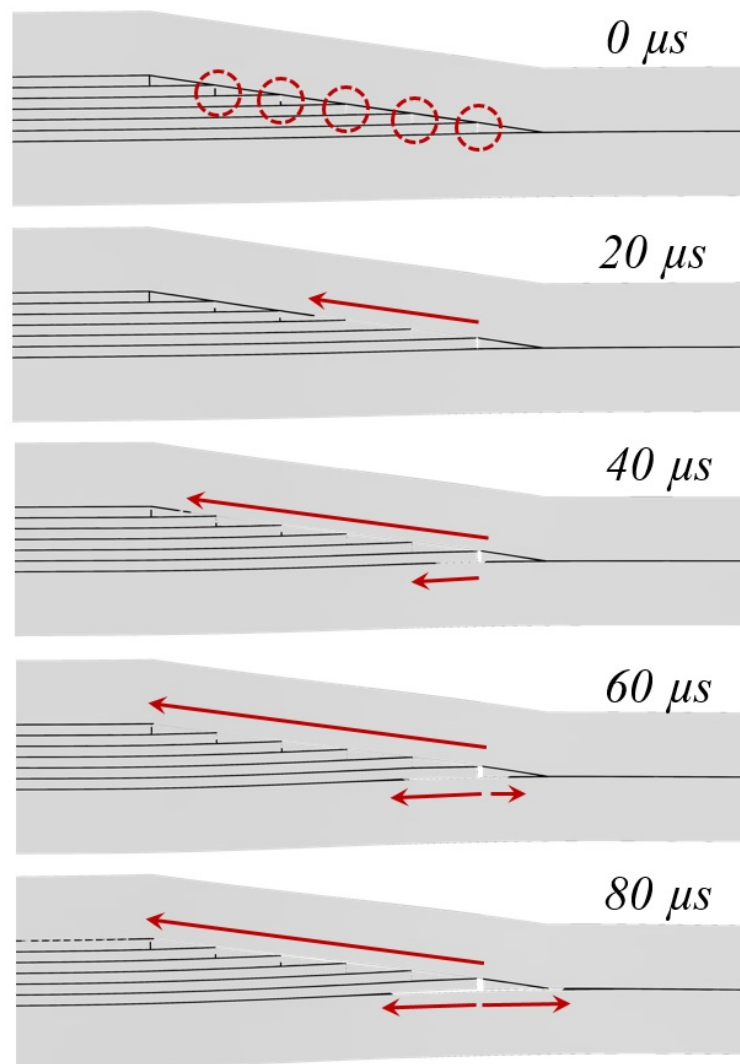


Figure 4.7: Delamination sequences in FEM results for U-1.

As shown in the first frame of Fig. 4.7 defined as $0 \mu s$, in configuration U-1, before initiation of any major delamination, the back wall of all resin pockets are damaged. During next $20 \mu s$, a crack starting from conjunction of second resin pocket / belt interface and vertical interface of first resin pocket, continues toward thick section of the laminate. Next delamination occurs at $40 \mu s$ in lower dropped ply / core interface which propagates toward thick section. While these cracks continue to propagate, another delamination is detected at $60 \mu s$ in the first resin pocket / core interface propagating toward the thin section.

No intralaminar damage is detected to this stage of loading. The first fiber damage (not fiber failure) occurs at about 1.6 ms after detection of first delamination for this specimen. The cohesive damage variable (SDEG) and fiber failure index (SDV 26) at the frame before fiber damage initiation is shown in Fig. 4.8.

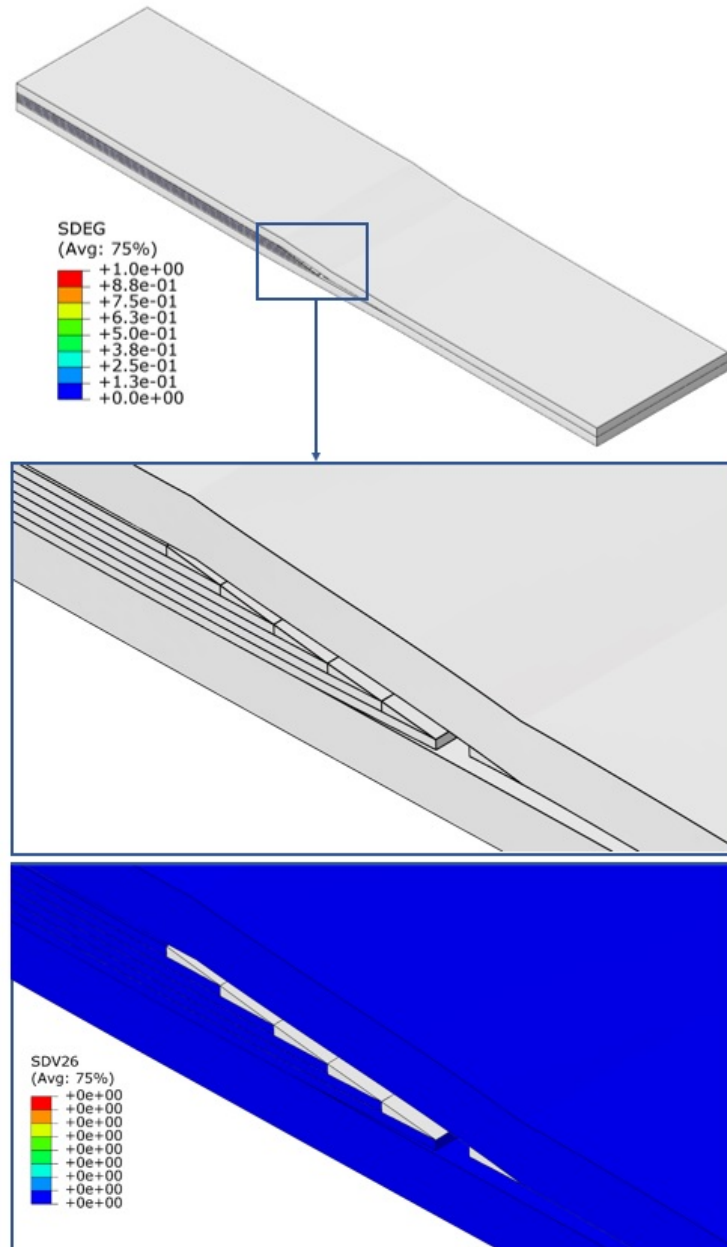


Figure 4.8: State of damage variable for cohesive element and fiber failure index at a frame just before initiation of fiber damage in configuration U-1.

As shown in Fig. 4.9 the value of failure index (SDV 26) is equal to unity which

indicates that the Hashin failure criterion for fiber damage is satisfied at the elements in the upper surface of belt sublaminate in thin section. In addition to tensile stresses along the specimen due to prescribed boundary conditions, additional normal stresses induced by bending also exist in this region. Also, the state of fiber damage index (SDV 7) shows the amount of material degradation for the corresponding failure mode.

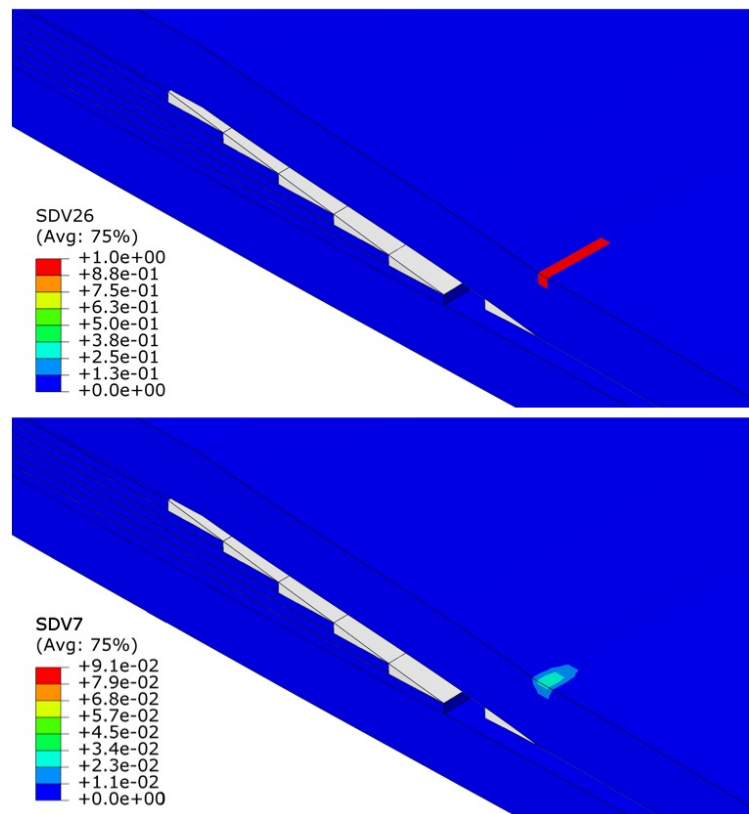


Figure 4.9: State of fiber failure index and fiber damage variable a frame just after initiation of fiber damage in configuration U-1.

The state of fiber damage at the end of loading is shown in Fig. 4.10 where the elements in the lower surface of the belt at the thick section are also damaged. The value of SDV 7 reaches 0.64 at this stage. Since the geometry and material properties for the specimens are the same, and no intralaminar damage is reported in the experimental study, the state of fiber and matrix damage variable is not shown for the remainder of the configurations.

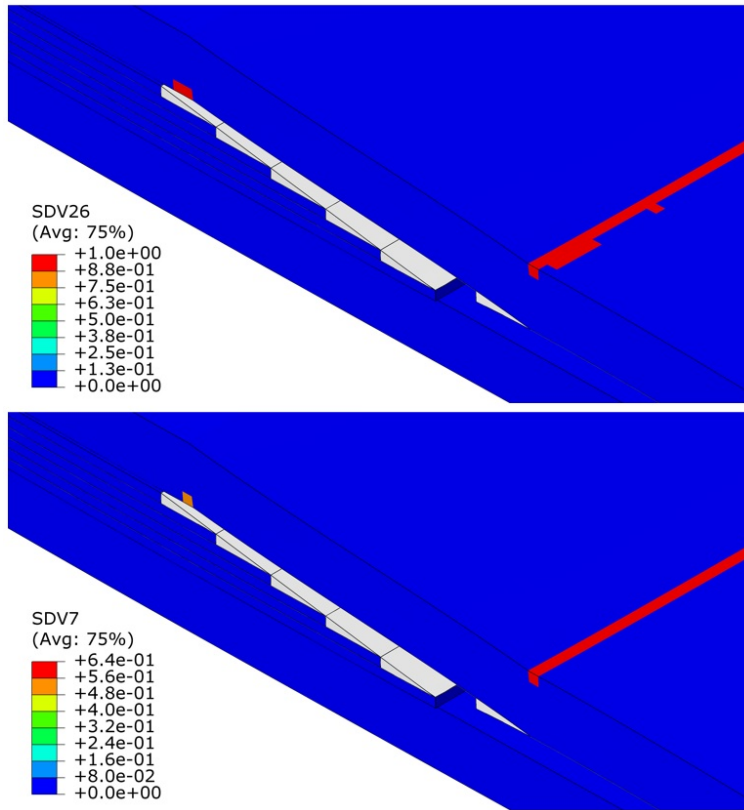


Figure 4.10: State of fiber failure index at fiber damage variable at the end of loading for configuration U-1.

The state of damage for configuration U-2 is shown in the first frame of Fig. 4.11. At 0 μs , back wall of the first two resin pockets are already damaged. Similar to configuration U-1, in configuration U-2, first a delamination occurs in the second resin pocket / belt interface and back wall of first resin pocket conjunction which is easily detectable at 20 μs . It then propagates toward the thick section. At 30 μs , two delaminations occur in the first resin pocket / core interface propagating toward both thin and thick sections. At this instant the vertical interface of the third resin pocket is also cracked.

Delamination initiation location and propagation sequence for U-3 configuration obtained from cohesive zone modeling is presented in Fig. 4.12. For this specimen type, before onset of any major delamination, the vertical interface of all resin pockets are cracked. At 10 μs , two delaminations are detected, one below the first resin pocket which grows to the thin section, and the other nucleating from the upper corner of the

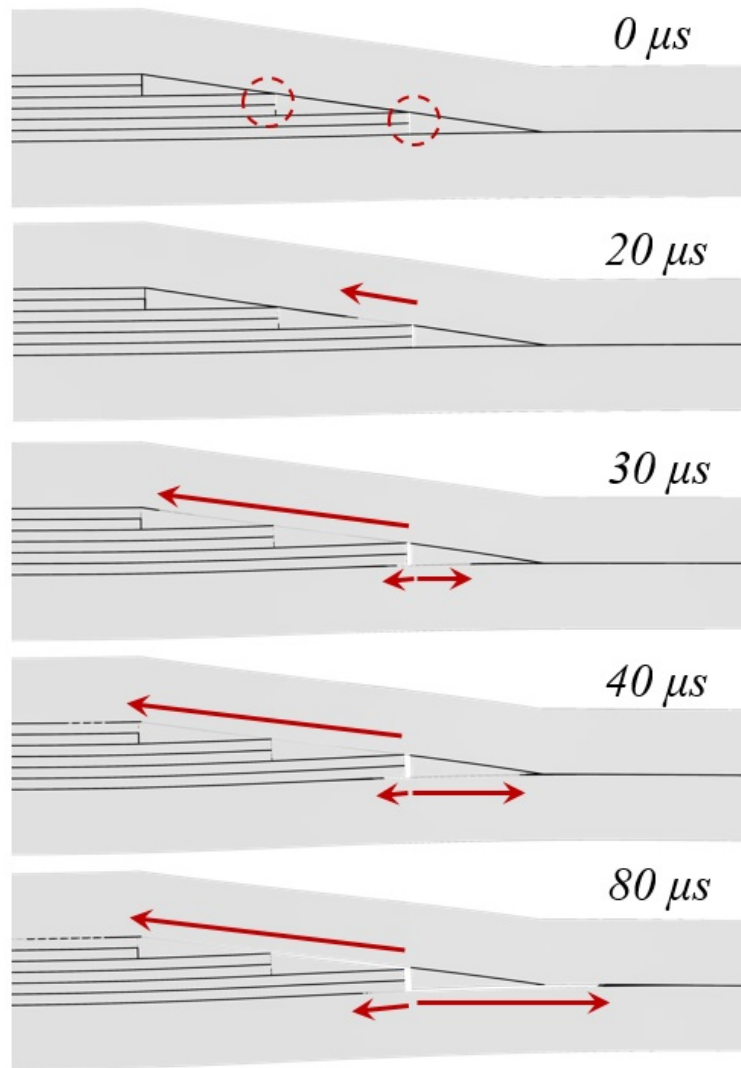
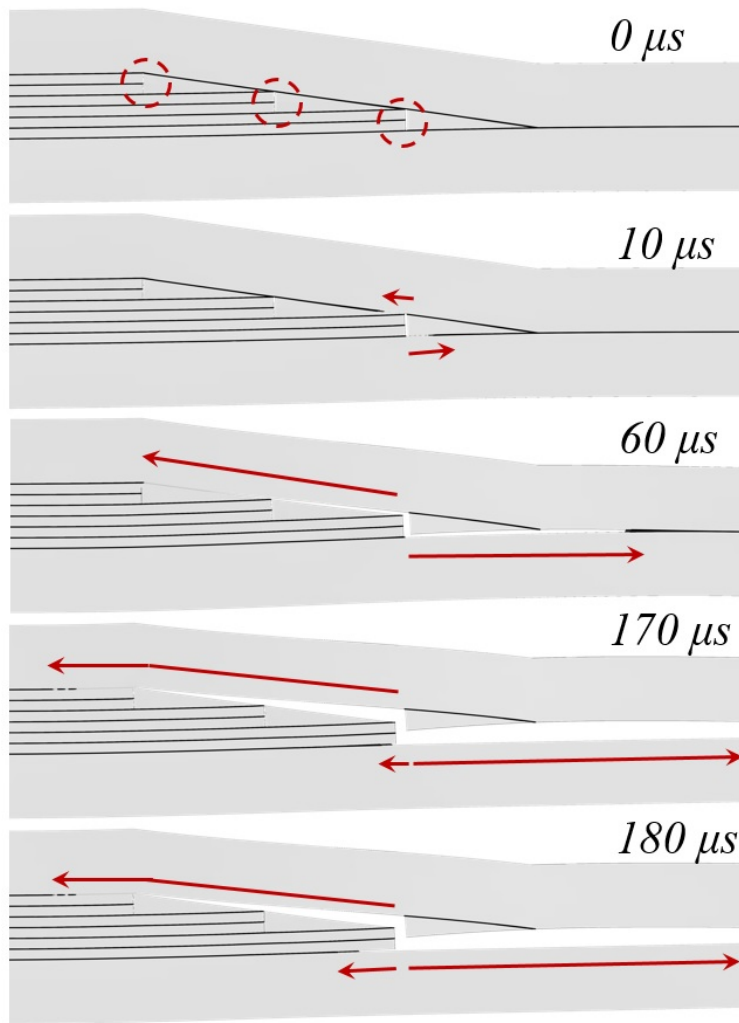


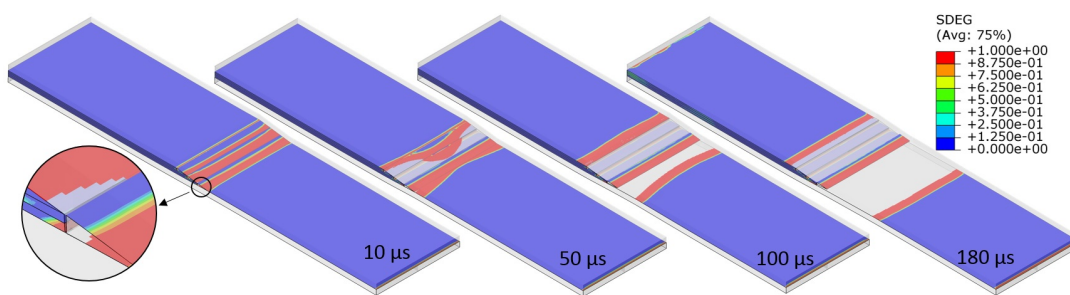
Figure 4.11: Delamination sequences in FEM results for U-2.

first resin pocket and propagating into thick section. While these cracks continue to propagate, at $170 \mu s$, a third delamination occurs in the lower corner of the first resin pocket, and it passes toward the thick section. In specimen types U-1, U-2 and U-3, no delaminations are observed between the dropped plies.

In configurations U-4 and U-5, since a very different delamination sequence from experiments is predicted, a new set of analyses is carried out. The finite element results for these configurations are discussed in detail in the following section.



(a)



(b)

Figure 4.12: FEM results for configuration U-3 (a) delamination state in edge view , (b) delamination sequence in 3D view.

4.4 Discussions

In this chapter, the finite element results for each specimen configuration are presented and compared to experimental observations. These comparisons are carried out in terms of the load at delamination onset, delamination locations, and the dynamic characteristics of delamination propagation. Also, a brief discussion on stiffness of the specimens and longitudinal strains are presented.

4.4.1 Stiffness and Strain

In the first step, the experimental force-stroke data is compared to the force-displacement results from the simulations. Fig. 4.13 shows the load-displacement from testing machine stroke and finite element results. As shown in this figure, the predicted stiffness by FE results is considerably higher than the one obtained from the load-stroke of the testing machine. A theoretical method and digital image correlation technique are utilized to investigate this difference.

Knowing the cross-section area (A), modulus of elasticity (E) and length (L) of each section of the laminate, the stiffness of thin, thick and tapered section of a tapered laminate can be calculated by:

$$K_i = \frac{A_i E_i}{L_i}, i = \text{thick, thin, tapered} \quad (4.1)$$

Thus, the stiffness of whole laminate can be estimated by:

$$K = \frac{1}{\frac{1}{K_{thin}} + \frac{1}{K_{thick}} + \frac{1}{K_{tapered}}} \quad (4.2)$$

Load-displacement curves from experiments based on cross-head displacements, from Digital Image Correlation (DIC) and curves from simulation and Eq. 4.2 for both cured and nominal dimensions for configuration U-1 are compared in Fig. 4.14. As shown in this figure, the predicted stiffness by simulations and theory are quite the same. However, these slopes are considerably higher than the one obtained from the load-stroke of the testing machine. Since the slope of DIC data and the finite element

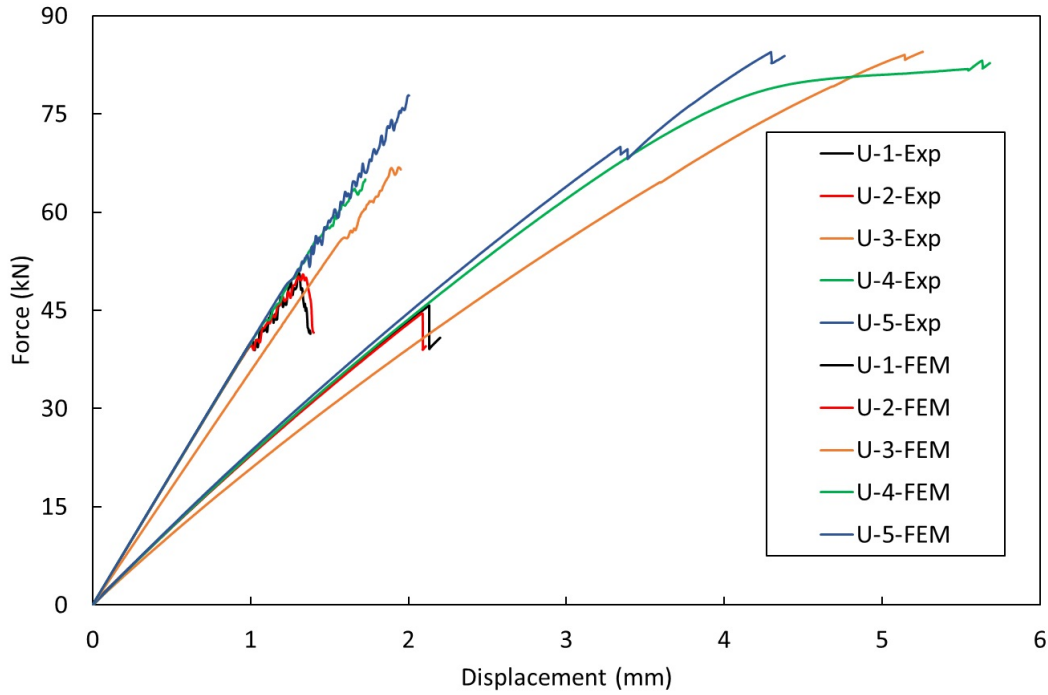


Figure 4.13: Load-displacement curve for specimens from FE results and stroke of test machine.

results for cured dimensions are in good agreement, it can be deduced that the compliance of the test machine is not negligible, and the displacements in force-stroke data can not be directly compared to finite element results. Therefore, only the loads in delamination initiations are used for comparisons, and displacements at these points are not considered.

For configuration U-1, in addition to HSC images, a DIC method is also employed to investigate the change of strain state in upper surface of the specimen during damage evolution. Longitudinal strain obtained by DIC and FEM results in upper surface of tapered region are presented in Fig. 4.15.

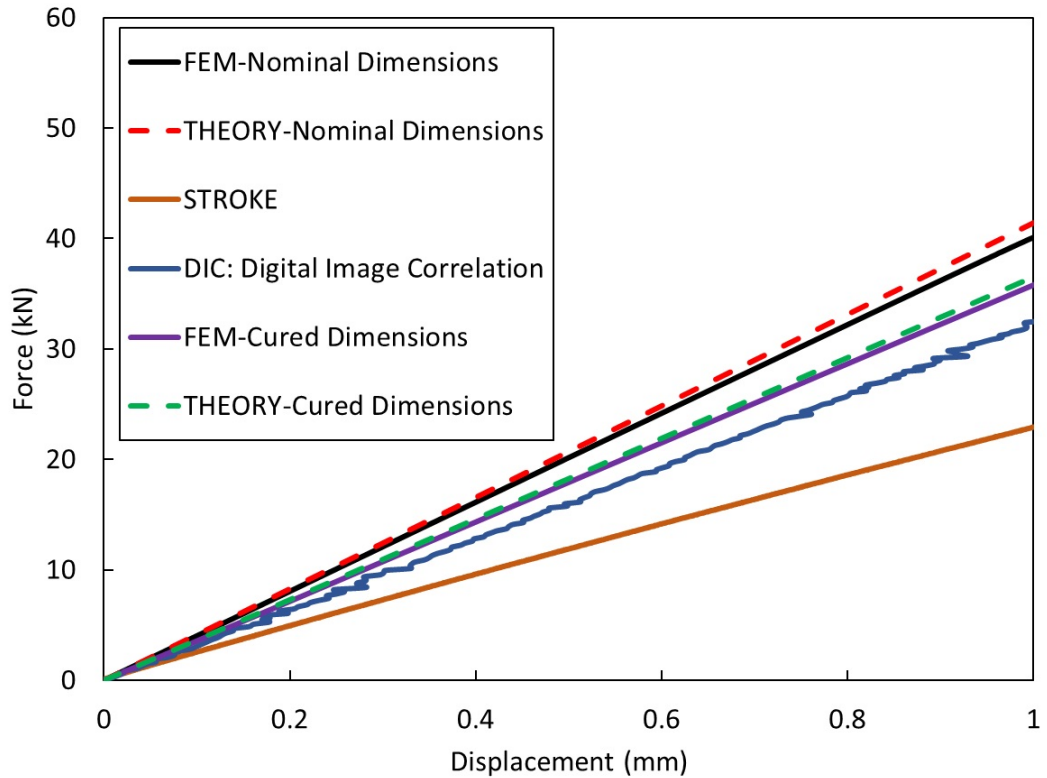


Figure 4.14: Load-displacement curve for U-1 specimen from FE, test machine stroke, DIC and theory.

As shown in Fig. 4.15, due to higher stiffness in the thick section, the longitudinal strain is lower than the thin section of the laminate for both before and after delamination. In regions away from tapered section, this strain component is constant which decreases by getting closer to tapered region. Then increases toward thin section with a maximum at the end of tapered region and after a decrease, it gets constant. The reason for minimum and maximum points of strain in the beginning and end of tapered section is the local bending due to straightening of belt sublaminates. This makes the upper surface of belt to be under compression and tension in the beginning and the end of tapered region, respectively. After failure, in spite of the increase of strain in the thick section, it reduces in the thin section. A similar behavior is found in FE results.

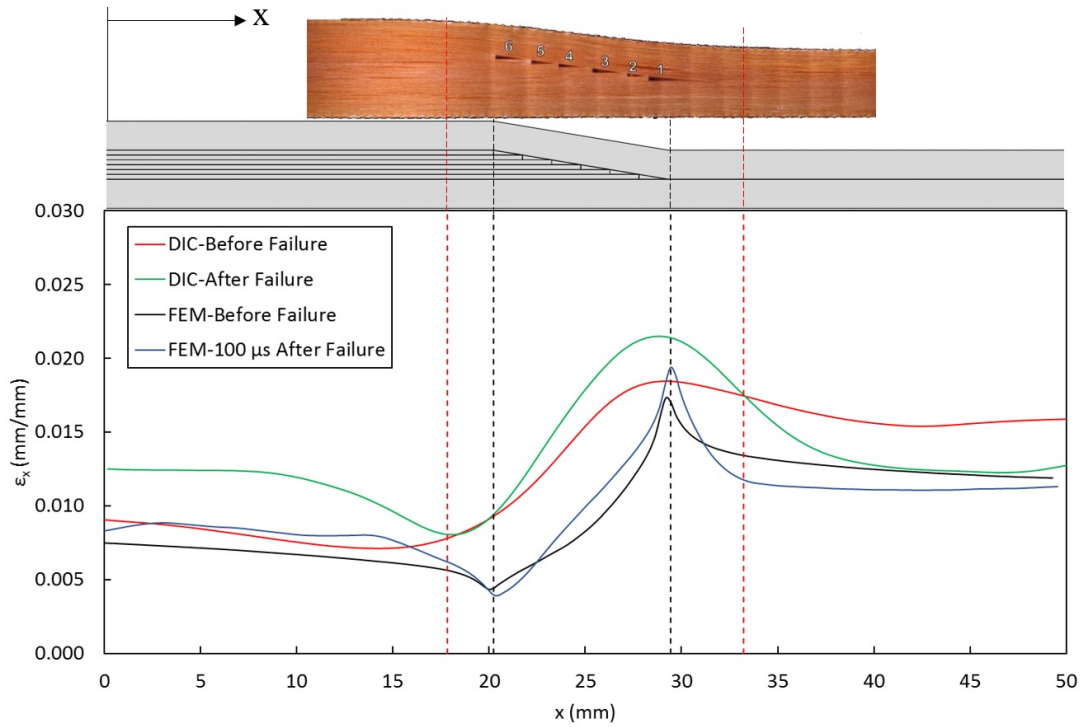


Figure 4.15: Comparison of longitudinal strains from DIC and FEM for configuration U-1.

4.4.2 Delamination Onset Loads

For all cases, a linear and steady behavior exists before delamination initiation. However, after load-drop, some oscillations in the load-displacement curves are detected. These kinds of oscillations are reported in literature especially for structures modeled with explicit finite element cohesive elements [34]. The delamination onset loads obtained from FE results and experiments are shown in Fig. 4.16.

Except for U-3 configuration, in which the exact delamination load could not be determined in experiments, the predicted delamination onset loads are underestimated in all other configurations. The amount of this underestimation is minimum in U-1 and U-2 configurations by approximately 5 kN (10.2%). One of the reasons for such considerable differences in delamination load between experimental and FE results can be due to the idealized geometry used in FEM, which differs from the geometry of the manufactured specimens. However, further investigations on delamination locations are carried out to scrutinize the validation of the finite element model.

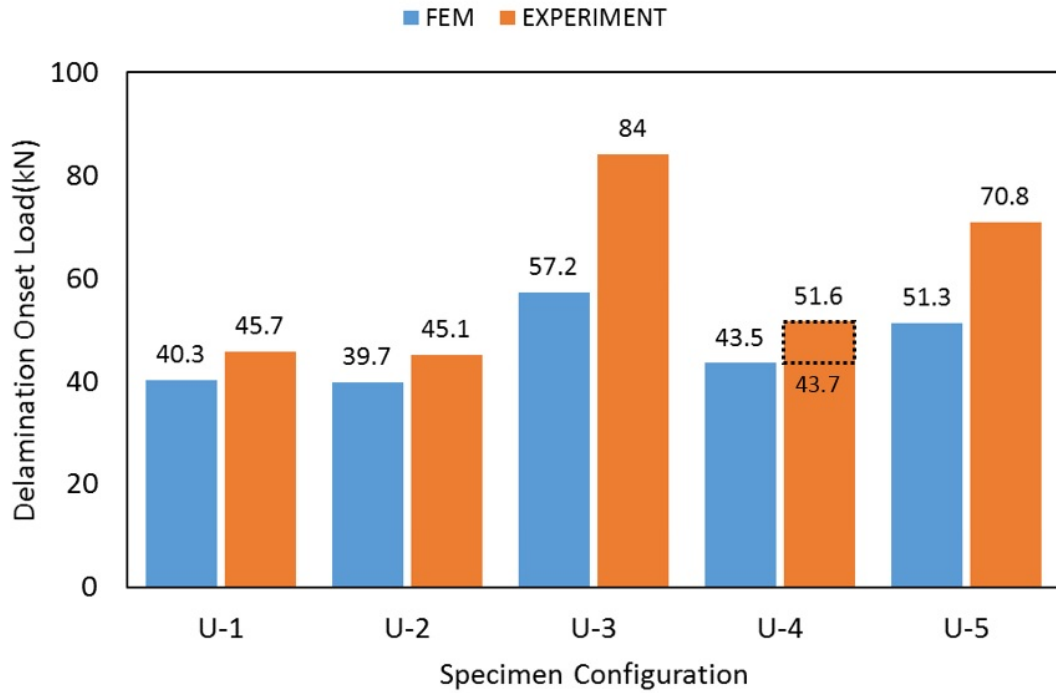


Figure 4.16: Delamination onset load predicted in FEM and measured in experiments.

4.4.3 Delamination Initiation and Propagation

Delamination initiation location and propagation sequence for U-1 configuration which are obtained from cohesive zone modeling and experiments are compared in Fig. 4.17. Comparing Fig. 4.17a to Fig. 4.17b, one can see the agreement in predicting delamination locations and propagation for U-1 specimen. However, comparing the time frames between CZM and images taken by HSC reveals that the delamination growth rate is underestimated in FE results. It takes $32.3 \mu s$ for detected delaminations by HSC to fully develop in the tapered region, while for a similar state of damage, the predicted time is $250 \mu s$. Despite this difference, it should be noted that the delamination propagation in both experiments and FE is very dynamic and in order of μs .

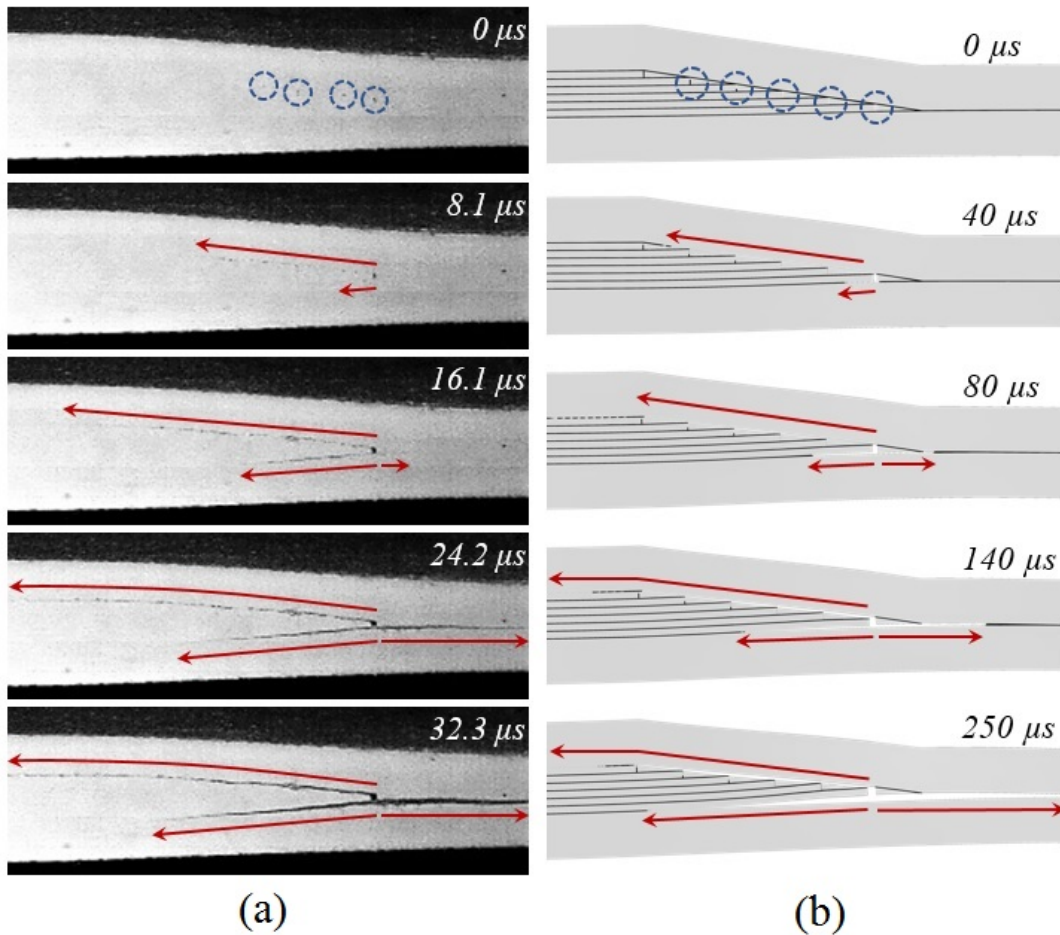


Figure 4.17: Delamination sequences for U-1 configurations (a) experiment, (b) FEM.

Fig. 4.18 shows the delamination sequence for U-2 configuration obtained from FEA and high-speed camera. As shown in Fig. 4.18a and Fig. 4.18b, a good correlation between experimental results and simulations can be found. However, similar to configuration U-1, the delamination growth rate is underestimated in simulations.

Delamination initiation location and propagation sequence for U-3 configuration obtained from cohesive zone modeling is presented in Fig. 4.19. similar to previous cases, a slower delamination propagation, particularly for the third crack is predicted.

In configurations U-4 and U-5, a very different delamination sequence is experienced in simulations. Similar to delamination loads, propagation locations are not predicted correctly for these cases either. A premature opening delamination mode in belt / resin pockets and the belt / core interface exist as shown in Fig. 4.20.

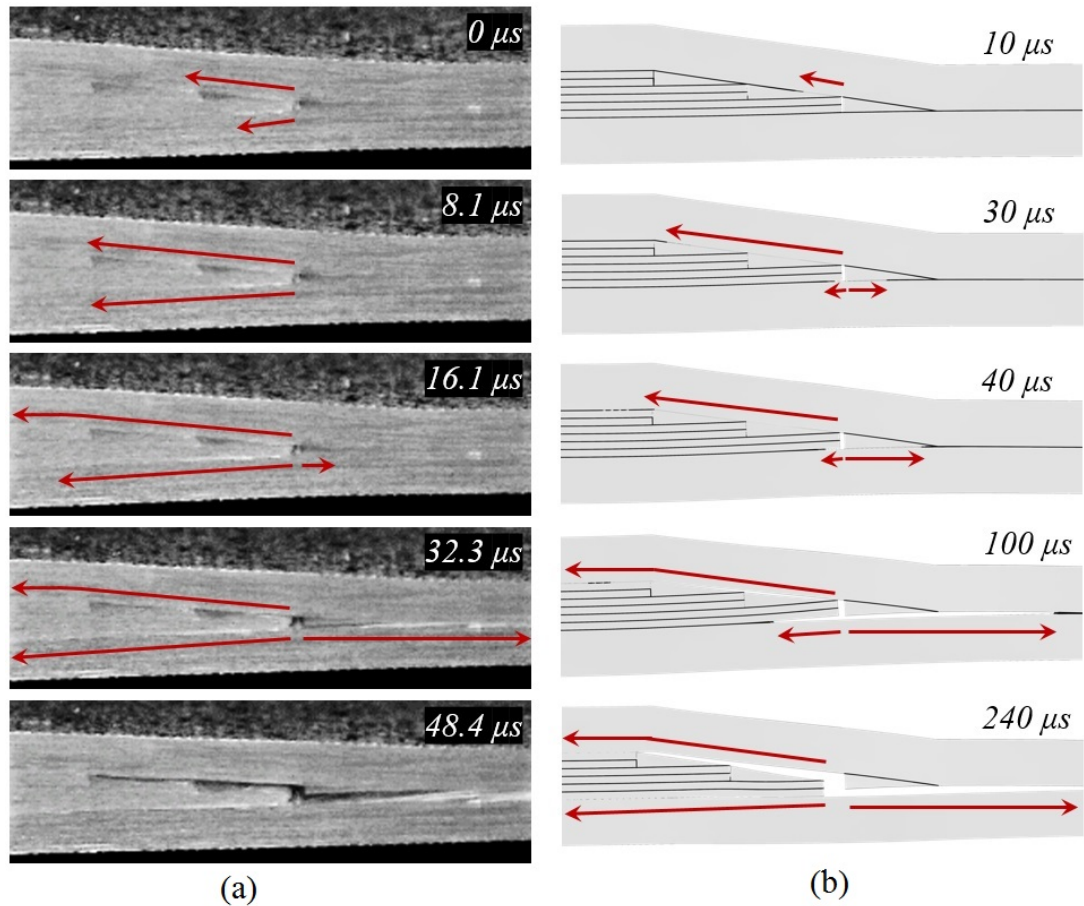


Figure 4.18: Delamination sequences for U-2 (a) experiment, (b) FEM.

Such a considerable difference between experimental and FE results due to the premature delamination is reported in [39], where damage types is categorized into strength-dominated failure initiation and fracture toughness dominated damage propagation cases. In the first case, damage is strongly driven by the cohesive strength pair used in the numerical model, hence the cohesive strength pair should be close to the real Mode I and Mode II interlaminar strengths of an interface. In the second case, the cohesive strength pair has been proved to show relatively less dependence on the material strengths, but it needs to be selected such that there are at least two to three cohesive elements in the cohesive region. In the mentioned study, the authors concluded that the configuration in which a numerically premature delamination occurred is strength-dominated failure case. Therefore, they utilized the average of maximum and minimum cohesive strength pair values for the same material reported in the literature. The new cohesive strength pair value ([60 MPa, 90 MPa]:[ILTS, ILSS])

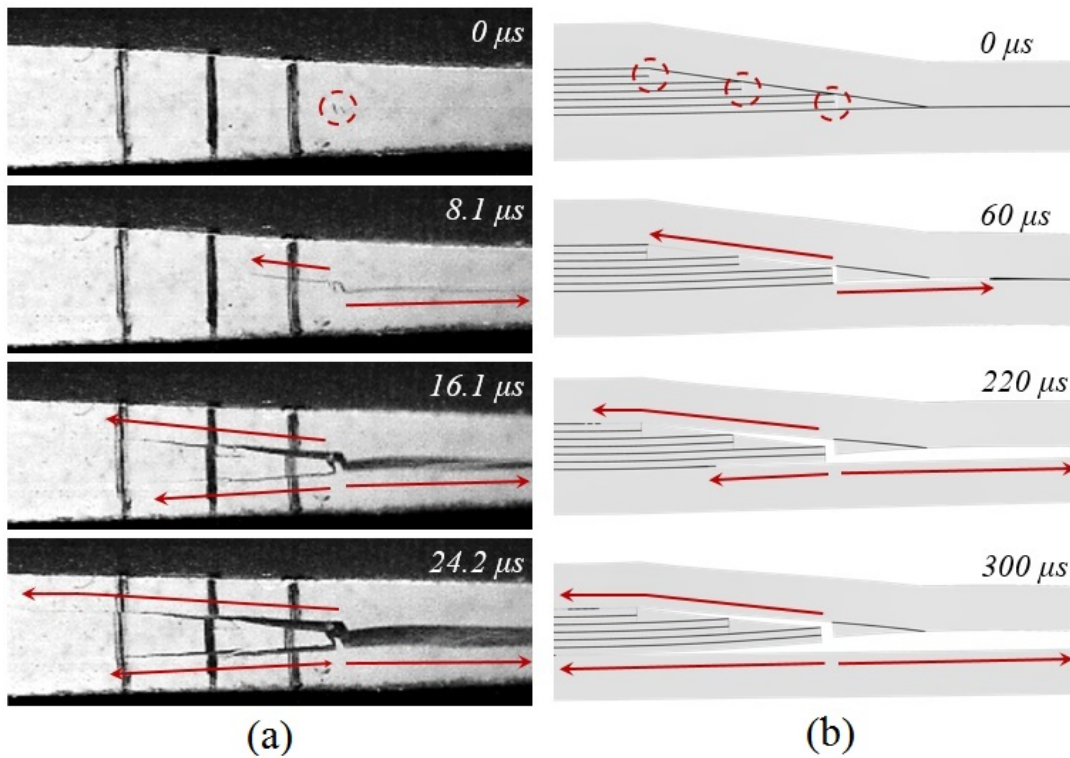


Figure 4.19: Delamination sequences for U-3 (a) experiment, (b) FEM.

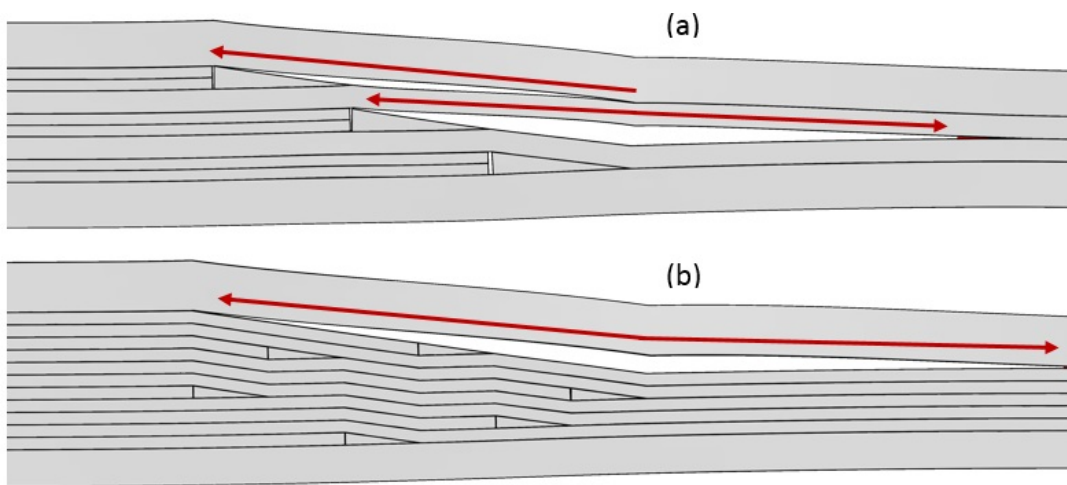


Figure 4.20: Premature delamination in , (a) U-4, (b) U-5.

was considerably higher than the values used in initial analyses [60 MPa, 90 MPa]. Updating strength pair values, eventually yields to good correlation to experimental measurement for delamination loads and delamination locations were also correctly predicted by the model using the new strength pair. A similar approach is utilized for

strength pair of U-4 and U-5 configurations. The ILTS and ILSS values for a similar material in [70] is reported to vary between 85-97 MPa and 60-109 MPa, respectively. Therefore, a new strength pair of [60 MPa, 90 MPa], as the average of minimum and maximum values reported in literature and Table 3.1 are utilized for the new set of analysis.

Fig. 4.21 shows delamination sequences for configuration U-4 with updated interface strength pair.

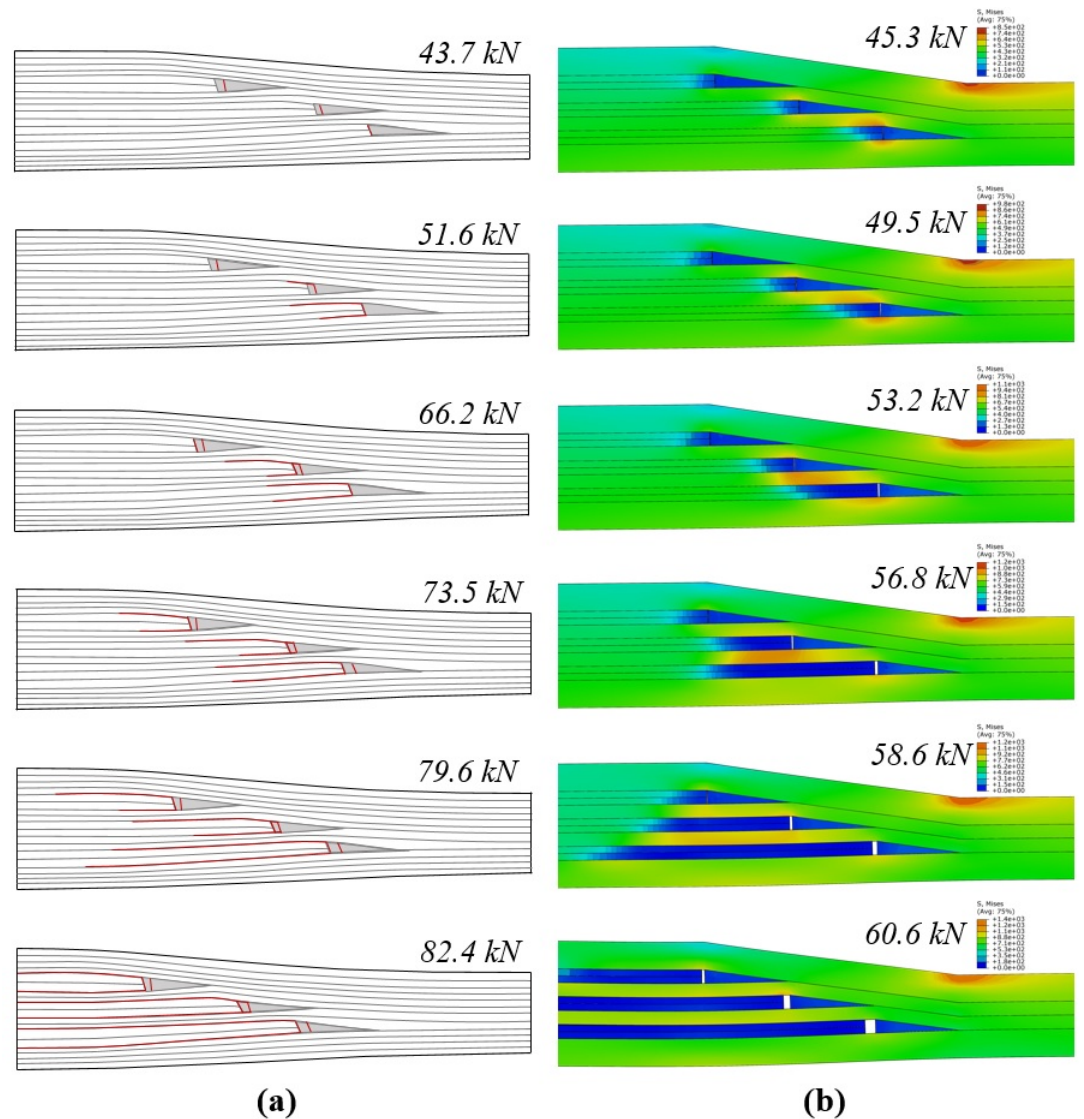


Figure 4.21: Damage evolution and equivalent stress distribution for U-4 specimen with enhanced interface strength.

Using enhanced interface strength pair, a Mode II dominant delamination behavior is

found for configuration U-4. The interfaces between dropped and continuous plies degrades in different locations in a way that the drop-off plies literally slide inside the laminate without any opening mode delaminations. Thus, in order to better illustrate the delamination paths in this specimen types, equivalent stresses in different delamination status are presented. By separation of dropped plies, the load carried by these components decrease, hence, the blue color of the dropped plies are indicator of damaged interfaces in Fig. 4.21. Using the new strength pair, the delamination load increases from 43.5 kN to 45.5 kN and more importantly, the delamination behavior is correctly predicted. It should be noted that since the delamination growth is found to be slow compared to previous cases, the step time of 0.1 s is too small for this case. Therefore, for this configuration, instead of time frames the loads at each damage states are used for comparisons.

Delamination sequences for configuration U-5 with enhanced interface strength pair is presented in Fig. 4.22.

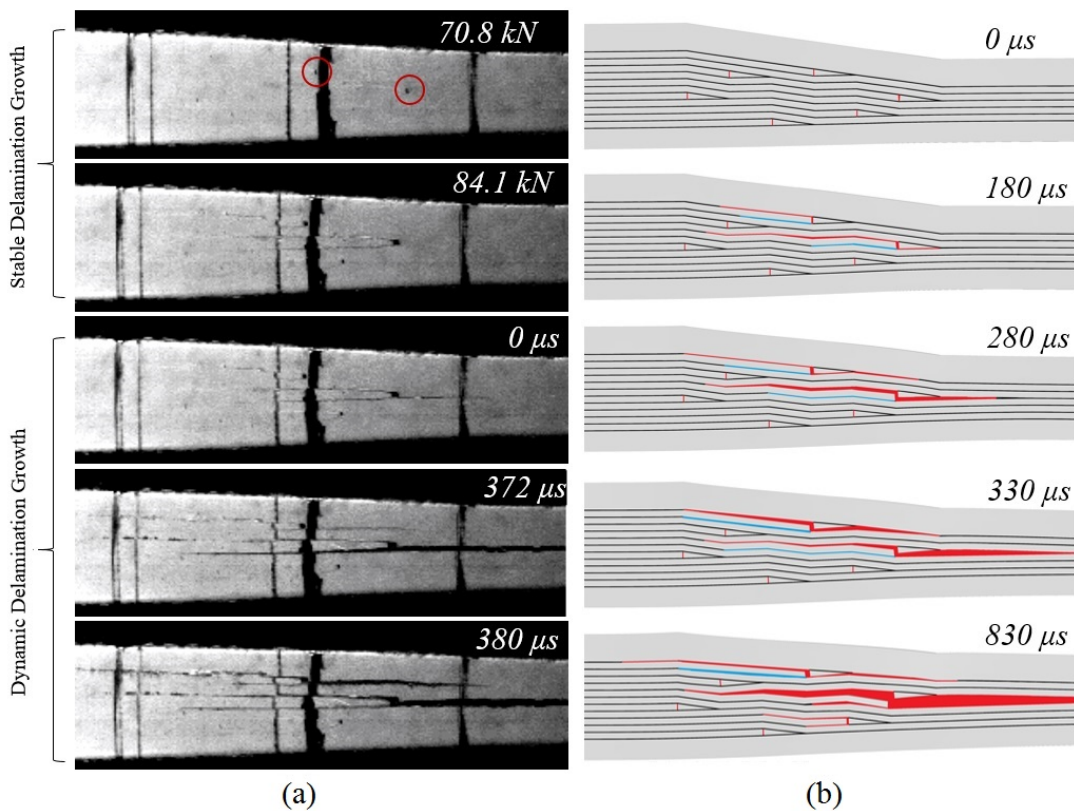


Figure 4.22: Damage evolution for U-5 configuration with enhanced interface strength.

The first delamination for this specimen is found to initiate in the fourth resin pocket. While the crack passes into the thick section, at $180\mu s$ two delamination onsets are detected, one in below the first resin pocket toward the thin section and the other in the sixth resin pocket toward the thick section. Some differences between FE results and HSC images are detected for this specimen type. In HSC images the interfaces below and above fourth and sixth dropped plies at drop-off locations are found to be damaged, while in finite element results the lower interfaces delaminations occur later. These interfaces are shown by blue color in Fig. 4.22. Using the enhanced strength pair for specimen U-5, not just modified the delamination patterns, but also increased the delamination load up to 66.3 kN.

A new set of FE analyses with updated values of interface strength pairs are carried out for other configurations, too. The results are shown in Fig. 4.23.

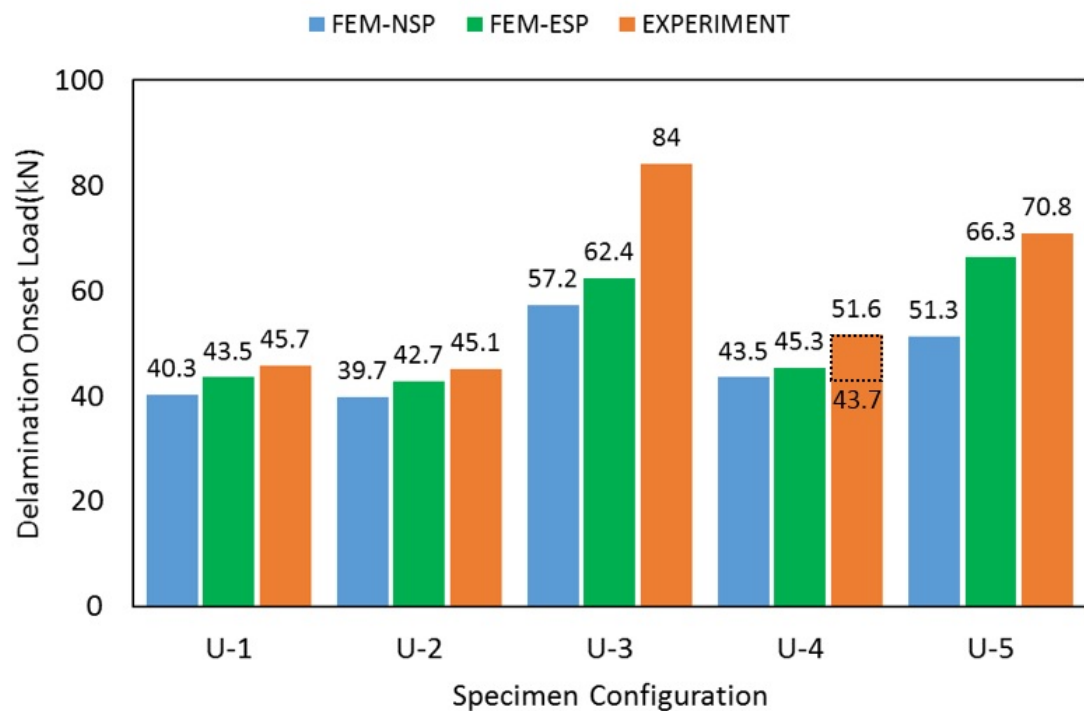


Figure 4.23: Delamination load values obtained by nominal strength pair (NSP), enhanced strength pairs (ESP) and experimental results.

The increase in delamination loads in U-1, U-2 and U-3 configurations due to the interface pair enhancement is 3.2, 3, and 5.2 kN respectively, which is significantly lower than 15 kN calculated for U-5 specimens. This implies that U-1, U-2 and U-3

are cases with the fracture toughness dominated damage, while U-5 is strength based. It should be noted that, taking a higher values for cohesive strength pair may lead to a higher delamination load. However, selecting an appropriate interface strength pair requires more investigations to have a better understanding of the delamination phenomena in strength based cases.

4.5 Chapter Conclusions

Damage in five asymmetric specimen types with different drop-off methods under tensile loading is investigated in this chapter. The simulation results of finite element modeling are compared to the observations of an experimental study. The outcome of this chapter is summarized in the following paragraphs.

Both finite element modeling results and experimental observations show that the vertical interface between resin pocket and dropped ply is the weakest location of the laminate and potential for damage initiation in all configurations.

Both finite element and experimental results show that specimens with consecutive drop-offs without continuous plies in between (U-1, U-2, and U-3) have the lowest delamination strength. Using $+45^\circ$ and -45° plies in drop-offs increases the delamination onset load considerably, which also is reported in the experimental results.

Delamination sequences captured by HSC and the amount of load drop show that delamination is highly dynamic and unstable for these cases. Delamination initiation locations and propagation patterns are effectively predicted by cohesive zone modeling for these cases. An overall good correlation with experimental results is found despite underestimating the delamination growth rate and initiation load in finite element results.

However, in specimens with continuous plies between the drop-offs, the finite element modeling is not as effective as the previous cases. Using the nominal interlaminar strength pair resulted in a premature opening mode which is not observed in HSC images. Preventing this early damage by enhancement of interface strength pairs in cohesive zone modeling, the predicted results are significantly improved in terms of

both delamination loads and locations for these configurations. Compared to the previous specimen types, slower delamination growth makes the time frame comparison for these laminate types less accurate. It also implies that the simulation of dynamic characteristics of delamination using cohesive zone modeling by dynamic explicit analyses is effective when the delamination growth rates are higher than the loading rate. However, to obtain more accurate results in the delamination growth rate for the cases with stable growth behavior, real simulation times are required, which may not be computationally affordable.

A new set of analyses with the enhanced cohesive strength pair is also carried out for all specimen types. The relatively low increase in delamination onset loads in new results shows the configurations with consecutive drop-offs can be categorized as fracture toughness dominant types. Despite a similar trend in delamination initiation load for configuration U-4, such a conclusion can not be made since the delamination characteristics are significantly changed by updating the strength pair. However, the configuration U-5 can be identified as the strength-dominant case, where the load at delamination onset considerably increases by using enhanced cohesive strength pair. Despite a good agreement between the finite element model and experimental results, further studies are required to develop a methodology for better the assessment of delamination characteristics of tapered laminates.

No intralaminar damage is predicted in simulations of all configurations, which is verified by experimental results.

CHAPTER 5

PARAMETRIC STUDY

5.1 Introduction

In addition to the validation study, some important aspects of utilizing cohesive elements in the modeling of delamination in tapered laminates are also investigated. For this purpose, three different cases of laminates with one, two, and three drop-offs are considered. For each case, combinations of 0° and 45° plies for each sublaminates are modeled. For this section, both Abaqus/Standard and Abaqus/Explicit are utilized to carry out static and dynamic analysis, respectively. A method similar to one given in Chapter 3, is used for the calculation of minimum time step. For each case, damage evolution is correlated to the load-displacement graph of the simulation and stress state at delamination locations. The damage status and effective stress states before and after the first load drop is determined for each case. Also, crack extension and crack tip speed diagrams are presented in this chapter.

5.2 Model Details

Three different cases of laminates with one, two, and three drop-offs with combinations of 0° and 45° plies for belt, core and drop-offs are used in finite element modeling. The stacking sequence of the thick section for each combination is taken to be $[0/\underline{0}_n/0]_s$, $[45/\underline{0}_n/0]_s$, and $[0/\underline{45}_n/0]_s$, respectively, where the underline indicates the dropped plies.

Sublaminates thickness of 1 mm is used in this section. Selecting a thickness larger than the one of nominal ply done for magnifying the load drop or for exaggeration

the stiffness change in load-displacement curves since primary simulations show that the load drop is not easily detectable in thin sublaminates. The taper ratio is taken as 1 : 3, that corresponds to a tapered angle of approximately 18° . Thickness ratios of thick to thin sections are 3 : 2, 4 : 2 and 5 : 2 for $n = 1, 2,$ and 3, respectively. The width of the laminate is taken as 10 mm. The resin pocket is modeled as a right triangle.

The tie-constraint method discussed in chapter 3 is used for cohesive element generation. In the two-dimensional model, four-node CPS4R (plane stress) element and COH2D4 element are used for plies and cohesive layers, respectively. Also, eight-node C3D8R elements for composite plies and COH3D8 cohesive elements are used in three-dimensional models. In 2-D models, for 45° plies, the transformed material properties in Table 3.1 are utilized, while in 3-D analysis, a coordinate transformation is used to achieve the material properties in corresponding direction.

The tapered composite structure is considered to be under tensile displacement loading. Boundary conditions are applied at both ends, where the laminate is fixed at the left end of the thick section, and the axial displacement of 1 mm is applied at the right end of the thin section while other degrees of freedom are constrained. Also, symmetry boundary condition in the y-direction on the bottom surface is used. Details for geometry and boundary conditions used in FEM are shown in Fig. 5.1.

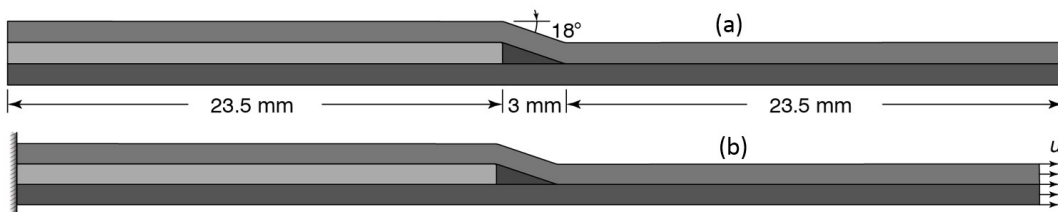


Figure 5.1: Geometry and Boundary conditions.

5.3 Results

5.3.1 2-D Implicit Results

Load-displacement curves of implicit finite element analysis results for laminates with single, double, and three drop-offs with combinations of 0° and 45° ply orientations for the belt, dropped ply, and core sublaminates are shown in Fig. 5.2 and 5.3.

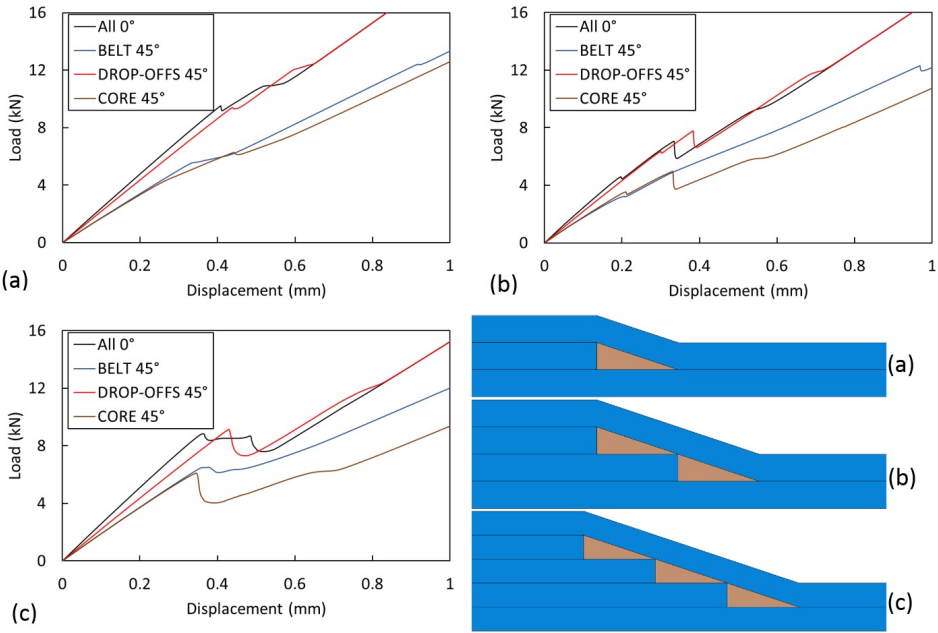


Figure 5.2: Load-displacement curves for implicit FEA for various ply orientations in (a) 1 drop-off (b) 2 drop-offs (c) 3 drop-offs.

Also, the results of load and displacement in the first load-drop, and initial and final stiffnesses for all laminates are summarized in Table 5.1. A consistency in stiffness change patterns is observed by comparing the load-displacement curves in each ply dropping group and between the dropped groups. In all cases involving 45° drop-offs, the initial stiffness (stiffness at the beginning of loading) is slightly less than the stiffness of the laminates composed of only 0° plies. After sequences of load drops and stiffness change, the stiffness of both cases completely matches. At this loading stage, interfaces of dropped plies are delaminated to a great extent, and load is carried by only the belt and core sublaminates, both having only 0° plies carry the

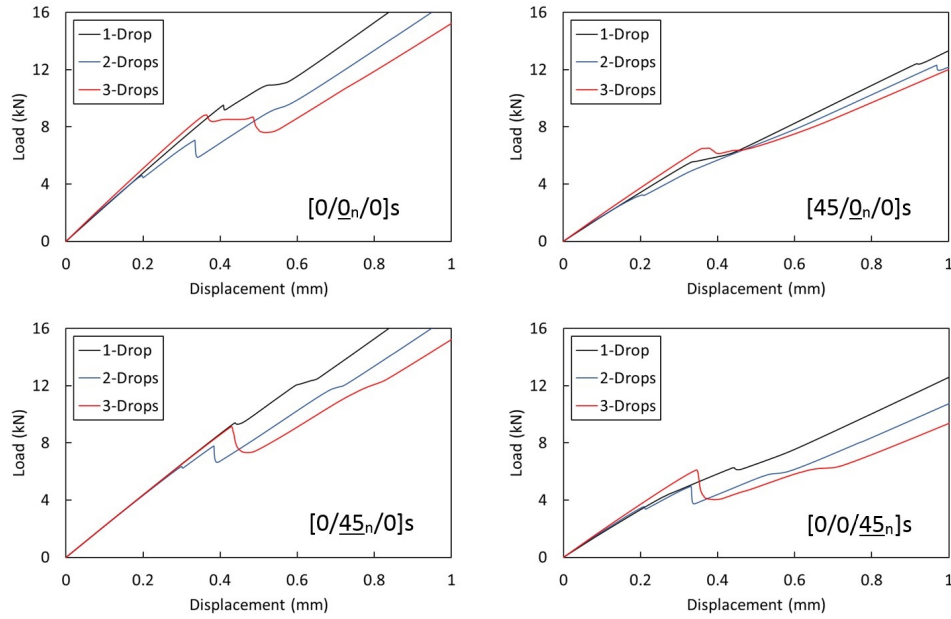


Figure 5.3: Load-displacement curves for implicit FEA for similar lay-up and different drop-off number.

load. $[45/0_n/0]_s$ and $[0/0_n/45]_s$ laminates have quite the same stiffness, considerably lower than $[0/0_n/0]_s$ and $[0/45_n/0]_s$. This implies that the contribution of dropped-ply in the laminate's overall stiffness is not significant. In contrast, the belt and core sublaminates as the continuous plies through the laminate govern the laminate's tensile stiffness. The percentage of load drop is increasing by n for all cases. The laminate with drop-off plies of 45° has the highest displacement and force in the first load drop. There is a load drop in the later stage of loading for all laminates having a 45° belt, which is not detected in other cases.

The location of delamination initiation from implicit analyses results for laminates with two and three drop-offs is shown in Fig. 5.4. In all the laminates with two drop-offs, delamination starts in the upper resin pocket/belt interface, propagating toward the laminate's thick section (Fig. 5.4a). In laminates with three drop-offs, the delamination initiation location is quite the same for $[0/0_3/0]_s$ and $[0/0_3/45]_s$, which starts from the second resin pocket/belt interface (Fig. 5.4b) toward the thick section. For the case of $[0/45_3/0]_s$ delamination initiates from the first resin pocket / belt interface, which propagates to both thin and thick sections (Fig. 5.4c). It should be noted that, in most cases, resin pocket vertical wall / dropped ply interface is found

Table 5.1: Displacement, load, initial and final stiffness for each laminate.

Lay-up	Displacement at 1 st Load-Drop (mm)	Load at 1 st Load-Drop (kN)	Initial stiffness (kN/mm)	Final stiffness (kN/mm)
[0/0/0]	0.41	9.5	23.5	18.9
[45/0/0]	0.33	5.5	17.1	13.1
[0/45/0]	0.44	9.3	21.8	18.8
[0/0/45]	0.27	4.4	16.8	12.6
[0/0 ₂ /0]	0.20	4.6	24.5	17.7
[45/0 ₂ /0]	0.21	3.2	17.5	12.3
[0/45 ₂ /0]	0.30	6.2	21.6	17.8
[0/0 ₂ /45]	0.21	3.5	17.9	11.5
[0/0 ₃ /0]	0.37	8.7	25.6	16.8
[45/0 ₃ /0]	0.37	6.5	18.7	11.6
[0/45 ₃ /0]	0.43	8.9	21.8	16.6
[0/0 ₃ /45]	0.35	6.0	18.4	10.8

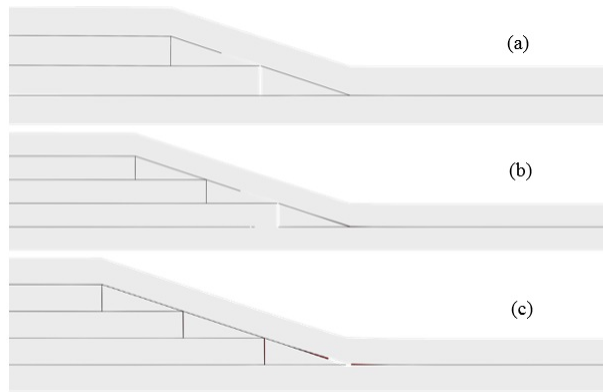


Figure 5.4: Delamination initiation location for (a) with double drop-offs, (b) $[0/0_3/0]_s$ and $[45/0_3/0]_s$ and (c) $[0/45_3/0]_s$.

to be the weakest in laminate, but since it has no effect on load-displacement curves and causes no load-drop, its behavior is not discussed in this study. The state of effective stress for laminates with two drop-offs just before and after the first load-drop is shown in Fig. 5.5. The location of the maximum value in the resin pocket / belt interface is transferred toward the thick section. For the case of $[45/0_2/0]_s$ laminate, since the stiffness of belt plies is less than core ply, the stress in core laminate is higher, while a similar effective stress distribution exist for two other cases.

As shown in Fig. 5.6, the state of effective stresses for laminates with three drop-offs

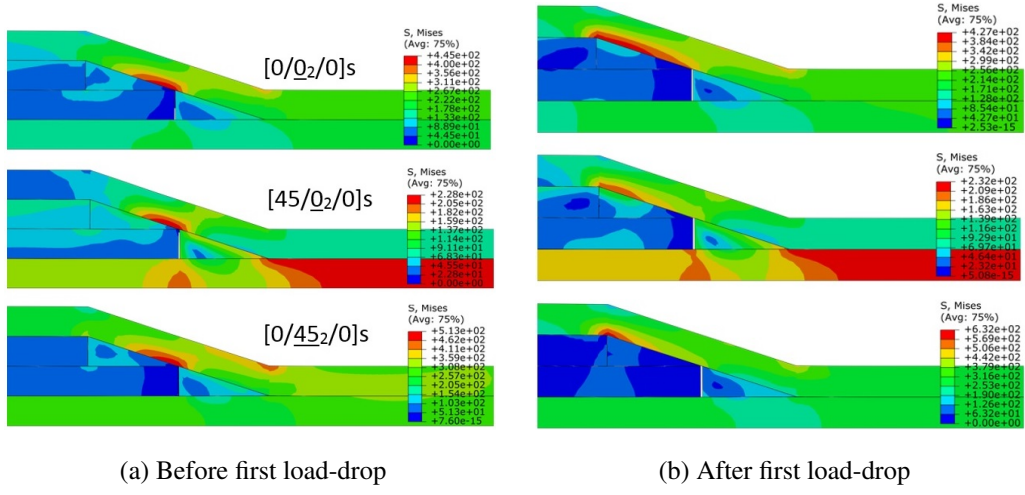


Figure 5.5: Distribution of equivalent stresses in laminate with 2 drop-offs before and after first load-drop.

before and after the first load-drop is very similar to the laminates with two drop-offs.

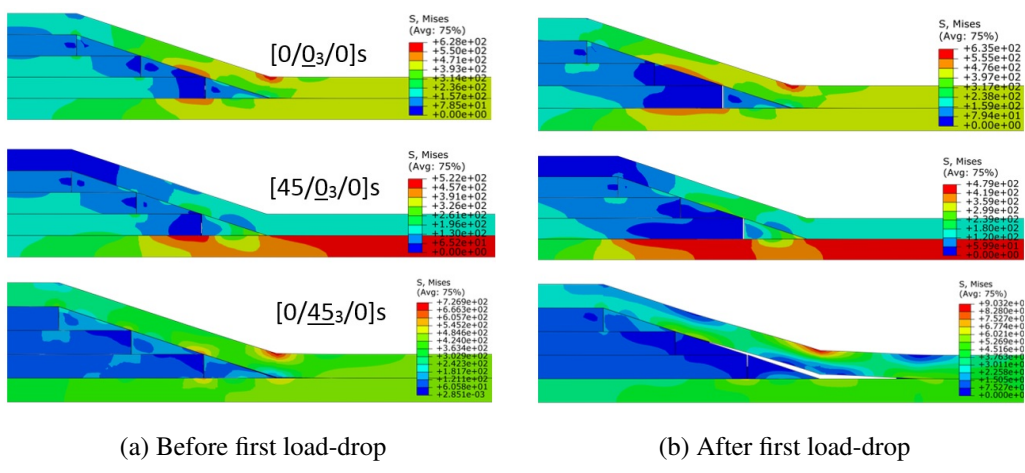


Figure 5.6: Distribution of equivalent stresses in laminates with 3 drop-offs before and after first load-drop.

Fig. 5.7 shows the distribution of effective stress for laminates with double and three drop-offs after the second load drop. A similar effective stress state is detectable between equivalent laminates in 2 drop-offs and 3 drop-offs. Although some useful information can be extracted from implicit analysis, since delamination initiation

and propagation is an intrinsically dynamic phenomenon as clearly observed in experiments, explicit analyses are performed for the study of delamination propagation.

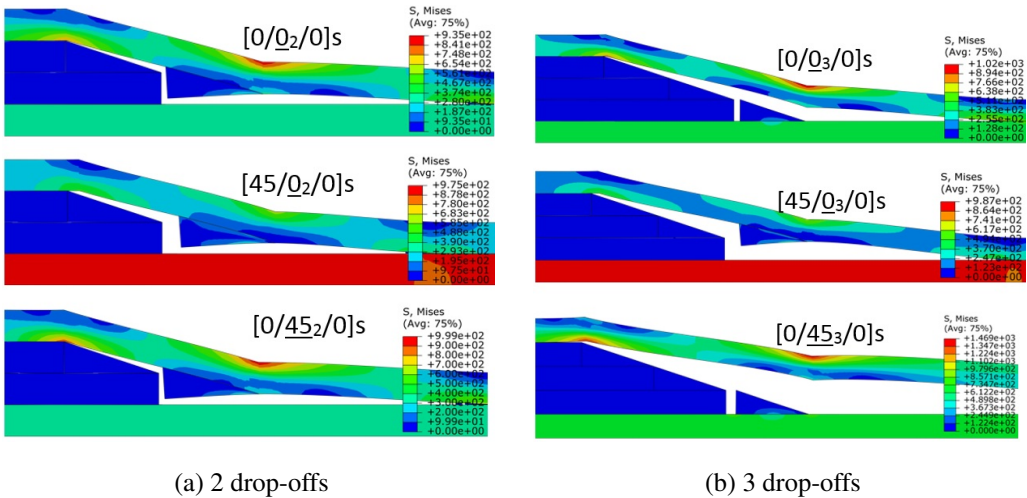


Figure 5.7: Distribution of equivalent stresses after last load-drop in laminates with (a) 2 drop-offs, (b) 3 drop-offs.

5.3.2 2-D Explicit Analysis Results

Load-displacement curves from both implicit and explicit analyses are shown in Fig. 5.8. The overall static and dynamic load-displacement behavior are found to be similar. Linear and steady behavior before the load-drop occurs in both cases. However, after load-drop, some oscillations in the load-displacement curve of explicit results exist after load-drops due to vibrations induced by inertial forces.

Delamination propagation patterns and the crack initiation time with respect to the first crack start time for different lay-ups are presented in Fig. 5.9. Like the results of static analyses, in most cases, the delamination initiates from the second resin pocket / belt interface. In $[0/0_2/0]_s$ and $[0/45_2/0]_s$ laminates, the initial crack is followed by a delamination in the first resin pocket tip, which propagates toward both thin and thick sections. $[45/0_2/0]_s$ laminate shows a different behavior than other laminates with two drop-offs. For this case, the second delamination initiates in the

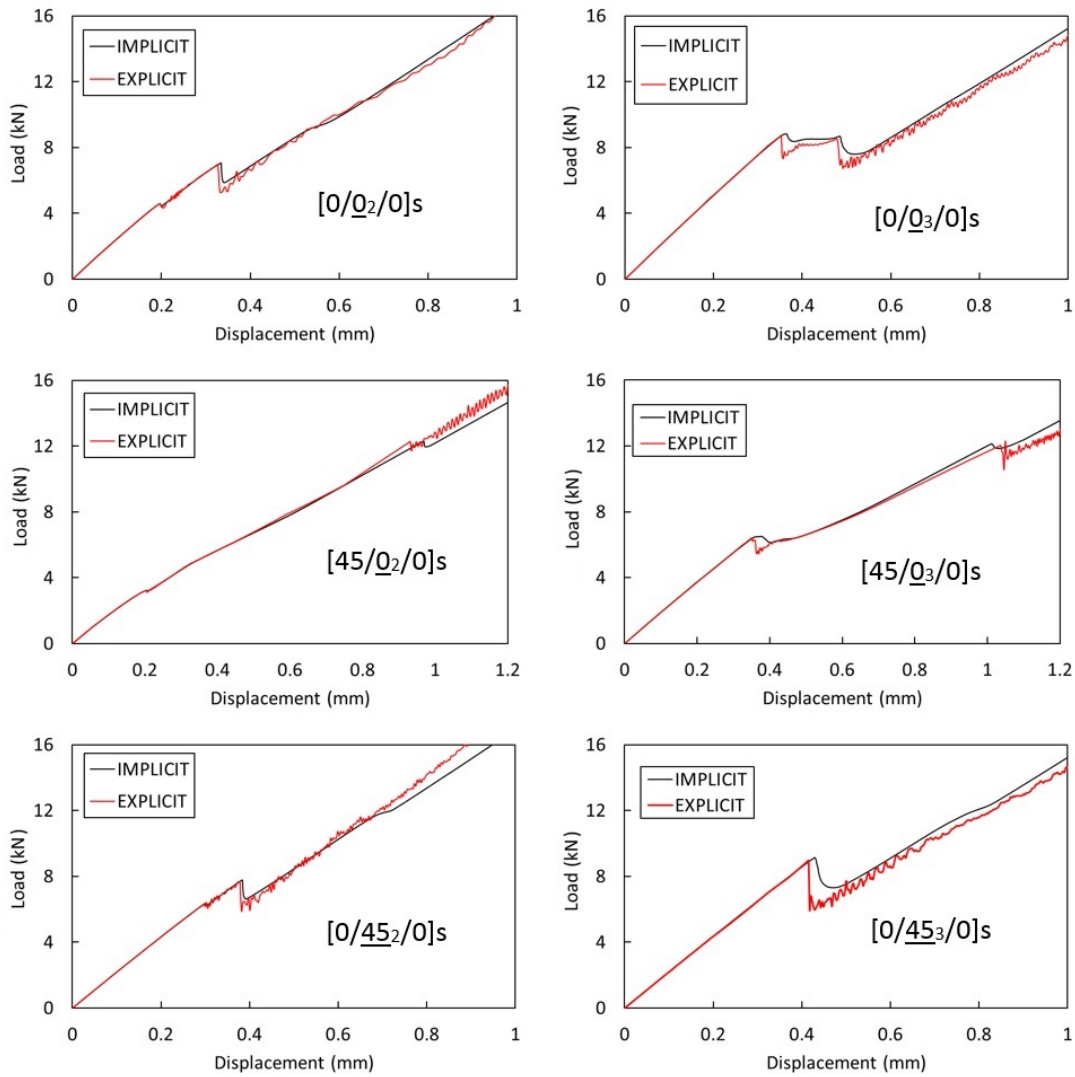


Figure 5.8: Load-displacement curves for implicit and explicit analyses.

belt / upper drop-off interface and continues into the thick section. However, the next delamination for this case, like the two others, is in the lower resin pocket tip toward the thin section.

In laminates with three drop-offs, a similarity in crack evolution patterns exists between $[0/0_3/0]_s$ and $[45/0_3/0]_s$ laminates, where the initial crack occurs in the second resin pocket / belt interface followed by a delamination below the first dropped ply. The time interval between each delamination in 3 drop-off cases, are considerably less than the case for laminates with two drop-offs. Also, for both drop-off methods, $[0/45_n/0]_s$ cases has considerably smaller time interval in comparison to other

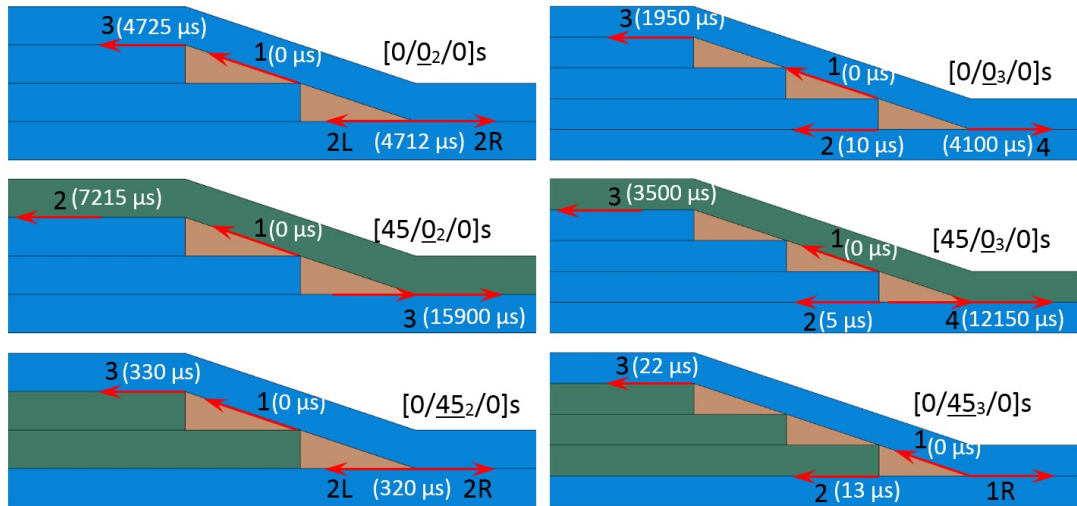


Figure 5.9: Delamination propagation patterns in different lay-ups.

lay-ups.

5.3.3 Delamination Propagation Speed

In this part of the study, the dynamic behavior of delaminations is discussed using the crack propagation speed for each of the laminates described in previous section. The crack tip speeds are calculated using the pointwise differentiation of the crack length graphs. In order to filter the high variations due to numerical differentiation, the moving average method [71] is used. The crack length vs. time and crack tip speed vs. time plots of the first delamination and the one growing into the thin section of the laminate, for the case of two drops are shown in Fig. 5.10 and 5.11, respectively.

For the case of 2 drop-offs, the first crack shows similar dynamic behavior in all configurations. This implies that the ply orientation does not affect the crack behavior in terms of delamination initiation location. [0/0₂/0]_s and [0/45₂/0]_s exhibit very similar dynamic behavior in all crack paths. For the case of [45/0₂/0]_s laminate, despite different propagation patterns, the crack propagation toward the thin section is very similar to two other cases.

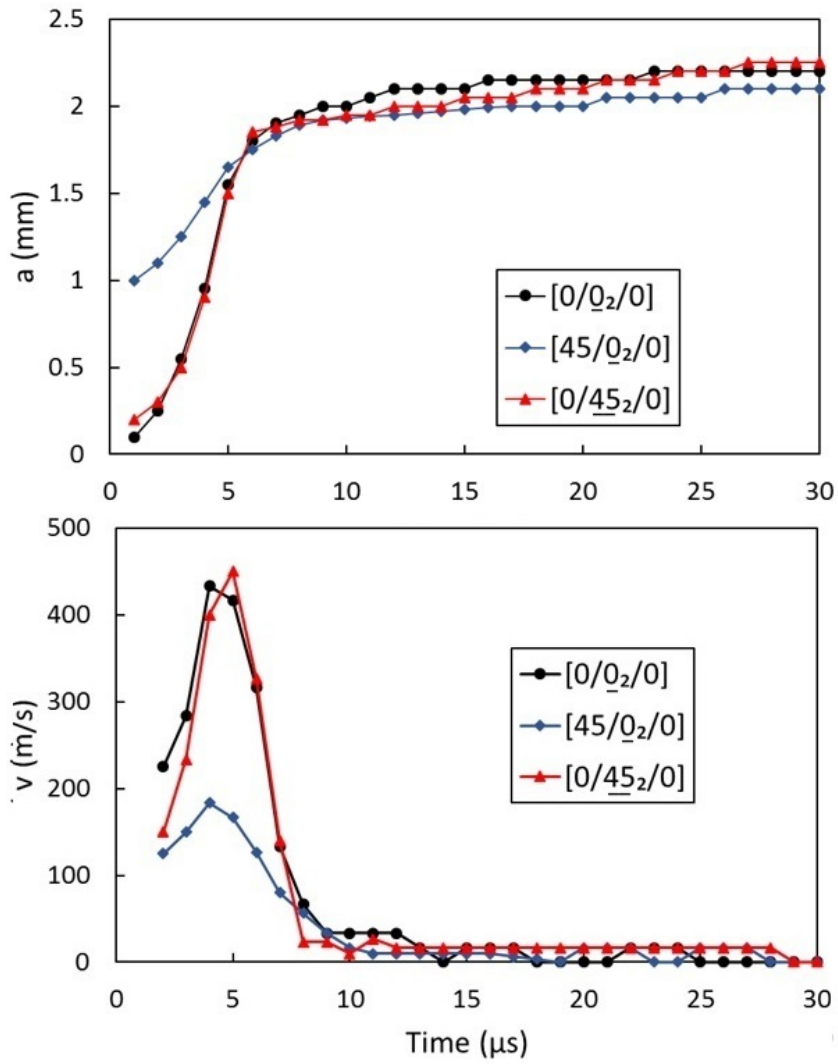


Figure 5.10: Crack length and crack tip speed vs. time plots for crack initiation in laminates with 2 drop-offs.

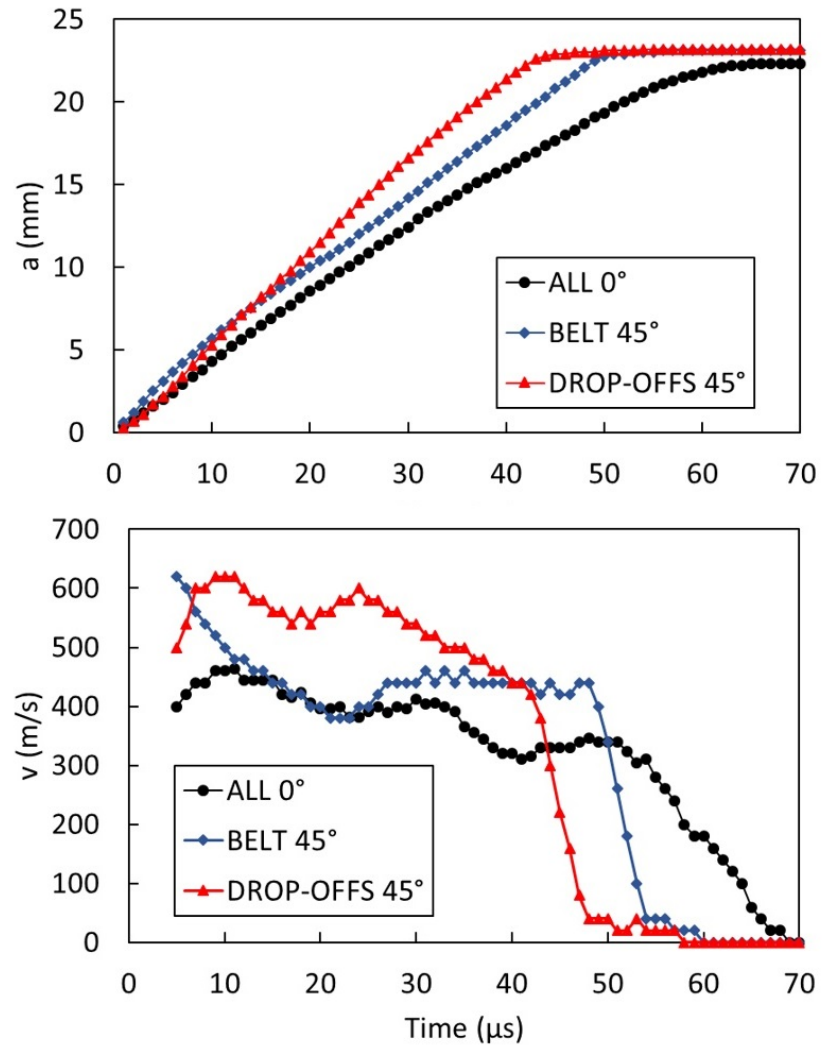


Figure 5.11: Crack length and crack tip speed vs. time plots for the crack growing into thin section for laminates with 2 drop-offs.

Figs. 5.12 and 5.13 show the crack length vs. time and crack tip speed vs. time graphs for the first and last cracks in laminates with three drop-offs. Like the case of laminate with two drop-offs, the dynamic delamination behavior is the same for these cases.

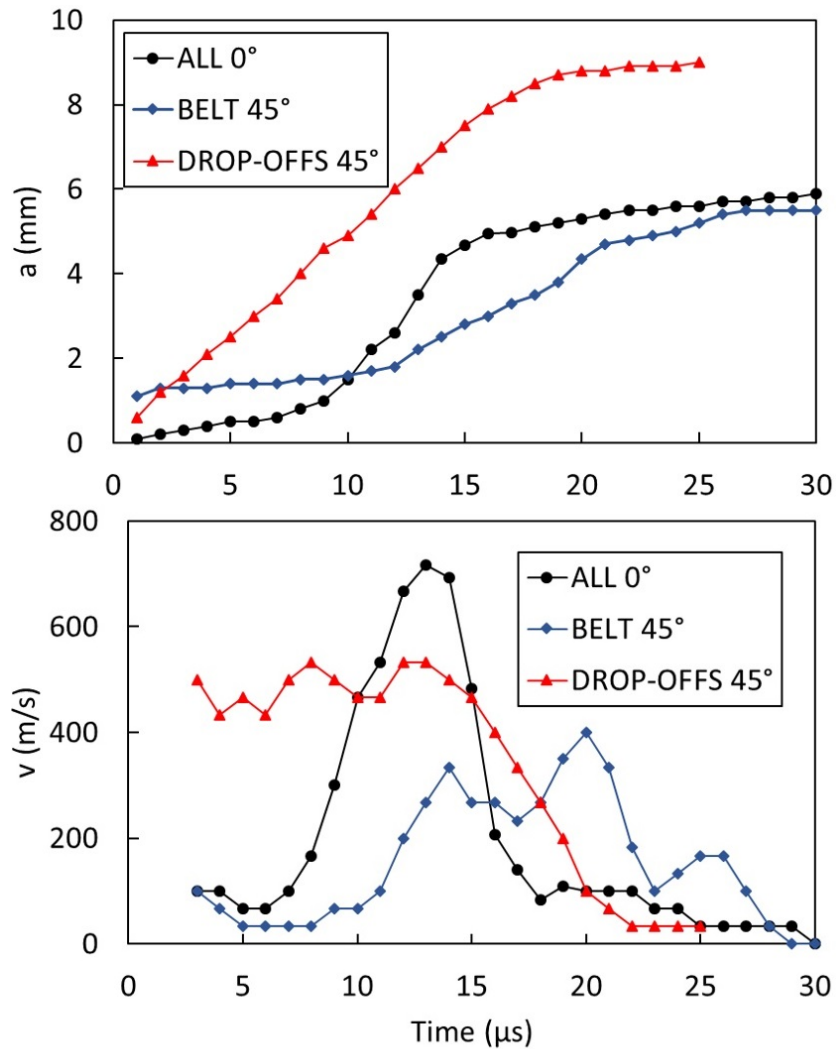


Figure 5.12: Crack length and crack tip speed vs. time plots for initial crack in laminates with 3 drop-offs.

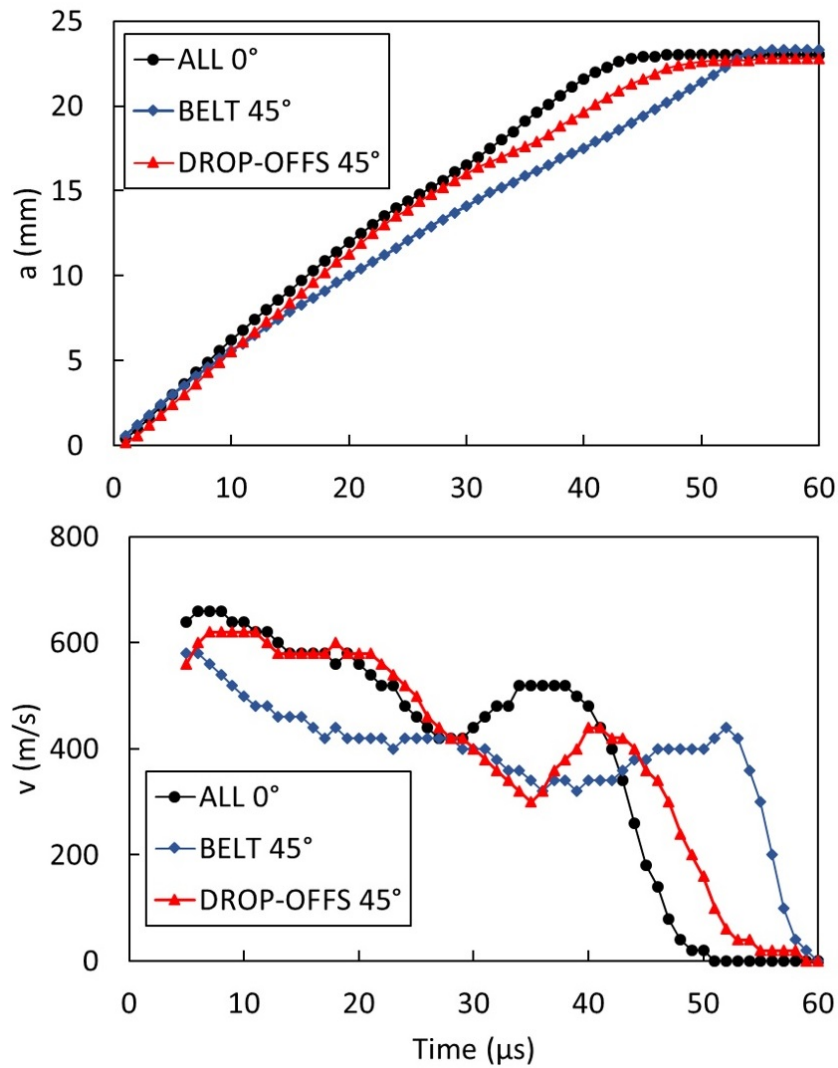


Figure 5.13: Crack length and Crack tip speed vs. time plots for the crack growing into thin section for laminates with 3 drop-offs.

Since $[0/\underline{45}_3/0]_s$ laminate shows very dynamic crack propagation responses, the graphs for this case are shown separately in Fig. 5.14. In this layup all cracks start in a very short time, where the last crack initiates only 23 μs after the first crack.

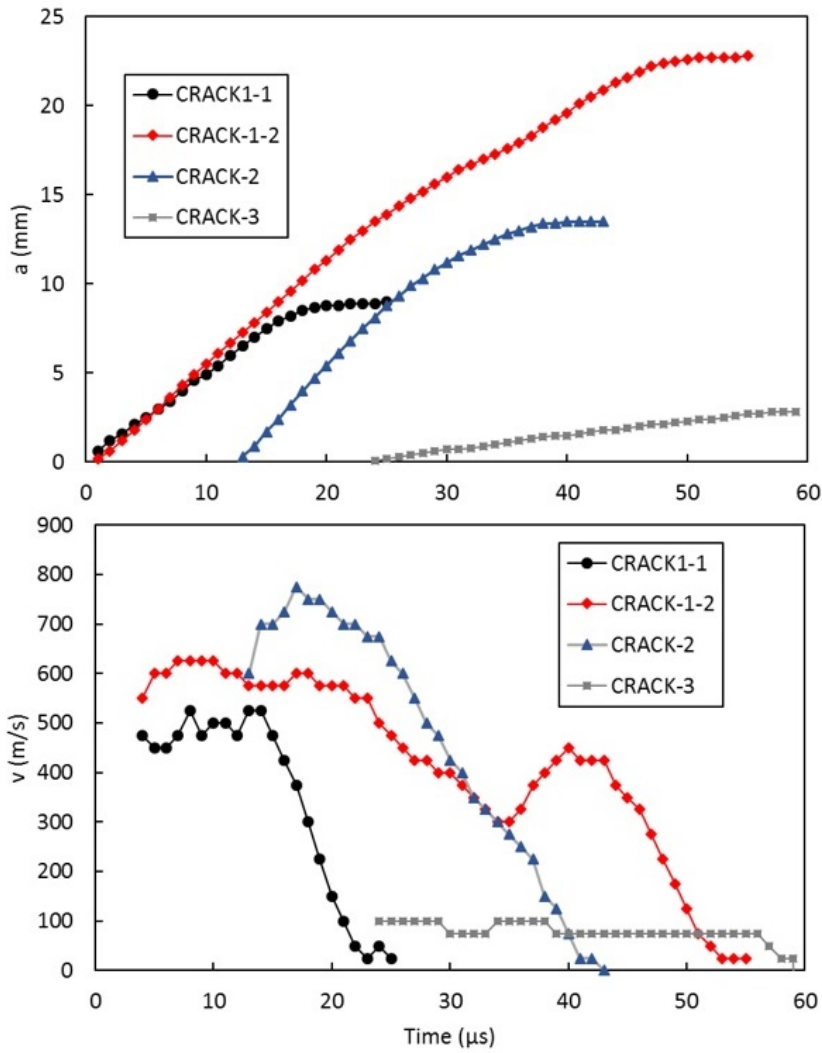


Figure 5.14: Crack length and crack tip speed vs. time plots for all cracks in $[0/45_3/0]_s$ laminate.

5.3.4 2-D vs. 3-D Results

Load-displacement curves for 2-D and 3-D explicit analyses are shown in Fig. 5.15. In all cases, the stiffness for 3-D modeling is slightly lower than 2-D. For laminates with all 0° plies, 2-D and 3-D curves are in good correlation, while in cases including 45° plies, specifically, cases including 45° belt, quite different behavior can be detected.

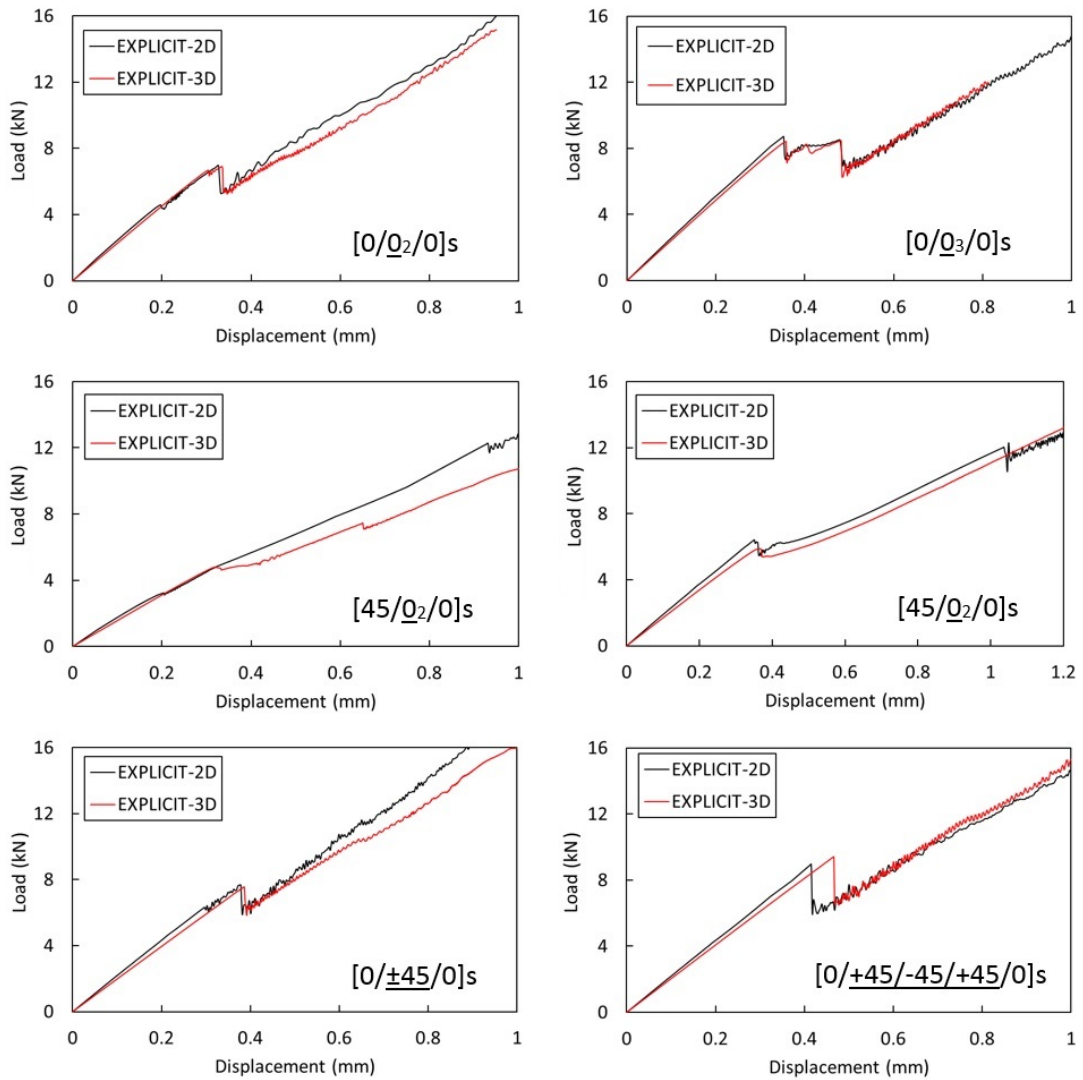


Figure 5.15: Comparison of load-displacement behavior for 2-D and 3-D explicit analyses.

Delamination initiation and propagation patterns for different lay-ups in 3-D analysis are presented in Fig. 5.16.

Delamination initiation location for 2-D and 3-D cases are found to be similar. However, some differences are detected in terms of delamination progression sequences.

Some differences are observed for in the interfaces between first resin pocket and core sublaminate. This crack path which exist in most cases of 2-D results, is completely eliminated in $[45/0_2/0]_s$ and $[45/0_3/0]_s$, and shifted to the upper interface of first resin pocket in $[0/0_2/0]_s$ and $[0/0_3/0]_s$ in 3-D results.

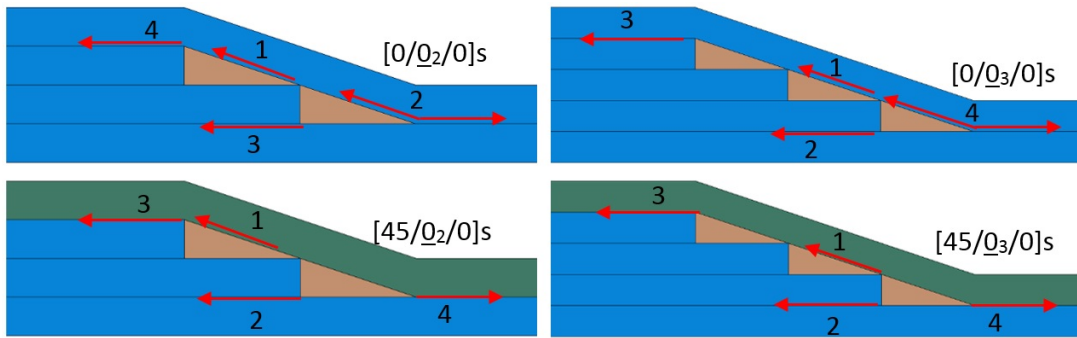
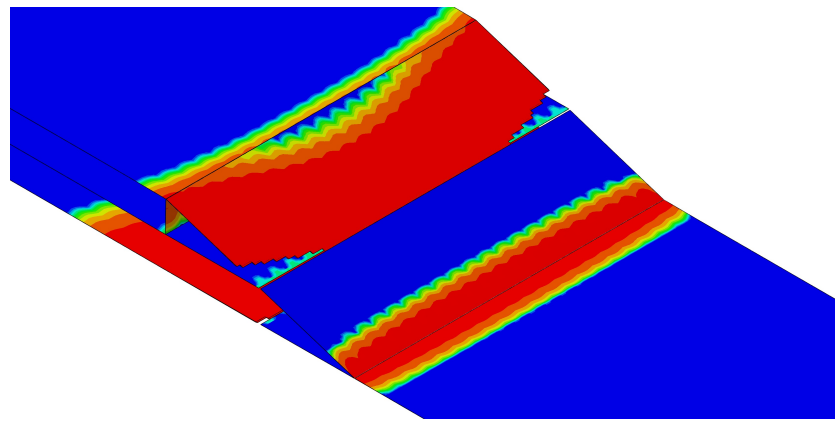
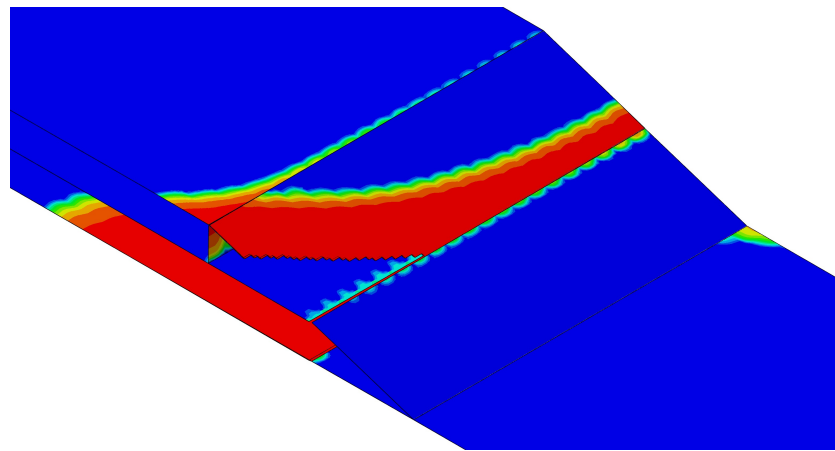


Figure 5.16: Delamination initiation and propagation patterns in 3-D results.

A non-uniform widthwise delamination, detectable in 3-D results can not be captured in 2-D modeling due to its two-dimensional nature. For $[0/\underline{0}_n/0]_s$ cases delamination start symmetrically in both sides of the laminate propagating both longitudinally and toward inside the laminate (Fig. 5.17a), while delamination is not symmetric in laminates including 45° sublaminates (Fig. 5.17b).



(a)



(b)

Figure 5.17: A non-uniform width-wise delamination.

The speed of a particular crack tip (crack 2 in $[0/0_2/0]_s$ laminate) in 2-D and 3-D analysis is compared in Fig. 5.18. Due to unsymmetrical delamination progression, laminates including 45° are not compared in this aspect. The crack length at laminate edge is used for 3-D model dynamic crack behavior.

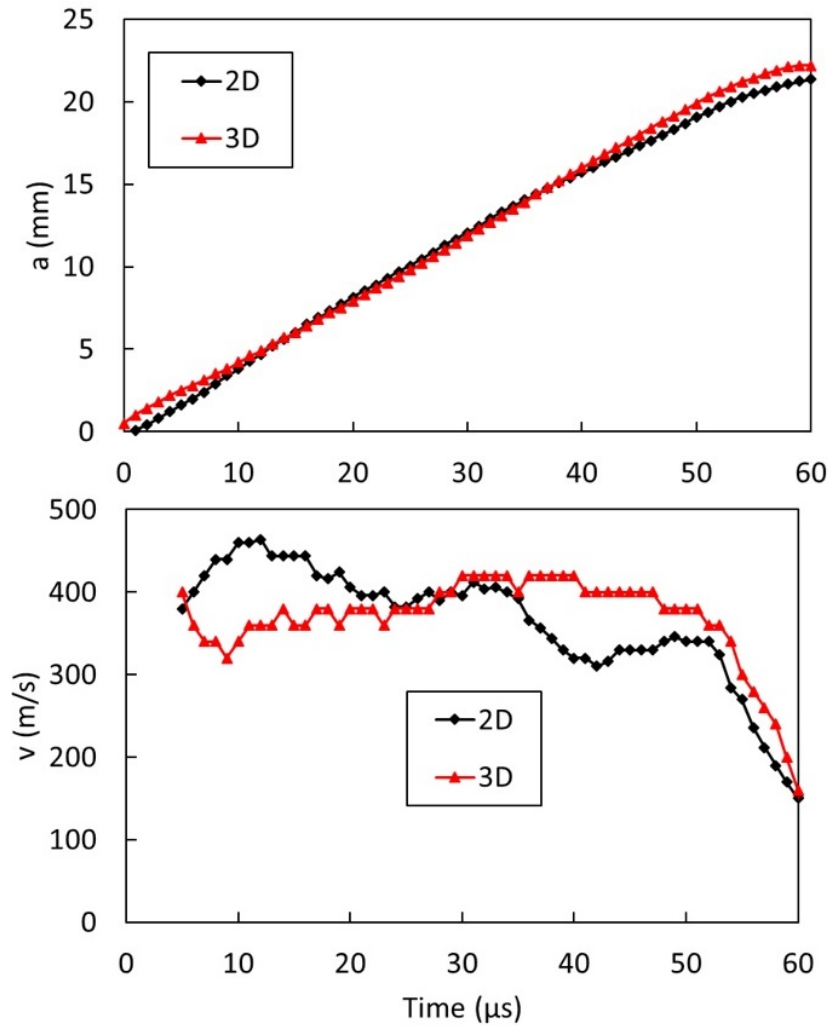


Figure 5.18: Comparison of crack length and crack tip speed plots for 2-D and 3-D explicit analyses.

5.4 Chapter Conclusions

Two and three-dimensional models were constructed for tapered laminates consisting of one, two, and three drop-offs. Laminates with various combinations of unidirectional plies with 0° and 45° orientations for the belt, core, and dropped sub-laminates are considered. Both implicit and explicit FE analyses are carried out. For each case, damage evolution is correlated to the load-displacement graph. The damage status and effective stress states before and after the first load drop are shown for each case. Also, crack extension and crack tip speeds versus time diagrams are obtained. The

outcome of this chapter can be summarized as follows:

- A failure in the vertical interface between a resin pocket and the neighboring drop-off ply seems to have no contribution on load drops of load-displacement curves, but it effects the propagation patterns.
- In all cases involving 45° drop-off plies, the initial stiffness (stiffness at the beginning of loading) is slightly less than the stiffness of the laminates with all plies of 0°. This implies that the contribution of drop-offs in overall stiffness of the laminate is not significant. After sequences of load drops, the stiffnesses for both layups completely match, since 0° belt and core, which are identical in both cases carry the significant portion of the load.
- Laminates with 45° core or belt have almost the same stiffness, considerably lower than the laminates with all 0° plies, which implies that belt and core sub-laminates have significant contribution on the overall stiffness of the laminate.
- For laminates with two and three drop-offs, the corner of second resin pocket (corner toward thin section) is found to be most critical than the corner of first resin pocket. However, in all laminates with two drop-offs delamination propagate along the interface below first resin pocket and toward thin section, while in laminates with three drop-offs, except laminate with 45° belt, the crack propagates above the resin pocket toward both thin and thick sections.
- There is a load drop observed in later stages of loading for all laminates having 45° belt which is not detected in other cases.
- Before damage initiation, stresses are highly non-uniform but they become more uniform after damage occurs and propagates.
- In most cases (except 3-drop-off case with 45° drop-off plies) the first crack initiates at the upper resin pocket / belt interface and its propagation ceases after a while and it resumes after delamination occur at other locations.
- The crack at the interface between the upper drop-off and the belt is very slow in all cases. In cases with 45° drop-off plies, all cracks start almost simultaneously while in other cases the time interval between each crack is comparatively larger.

CHAPTER 6

CONCLUSIONS AND FUTURE STUDY

6.1 Summary

In this thesis, damage in tapered composite laminates is investigated. The objective is to understand the delamination failure in tapered composite laminates made of unidirectional prepregs by creating high-fidelity simulation models. For this purpose, the cohesive zone method and a three-dimensional continuum damage mechanics-based material models are used to simulate delamination and composite ply damage, respectively. Results of an experimental study are utilized for the validation of finite element modeling. Five different types of asymmetric tapered specimens with different drop-off methods and layups are generated and implemented in ABAQUS/Explicit finite element tool. Finite element results are compared to the experimental observations in terms of delamination onset load, delamination initiation location, and propagation characteristics. An overall good agreement is obtained between experimental and numerical results.

Finite element modeling results and experimental observations show that in all configurations, the vertical interface between resin pocket and dropped ply is the weakest location of the laminate and potential for damage initiation. Although damage in these locations has no contribution to load drops in load-displacement curves, it affects the propagation patterns.

Both finite element and experimental results show that specimens with consecutive drop-offs without continuous plies in between have the lowest delamination strength. Using $+45^\circ$ and -45° plies in drop-offs increases the delamination onset load considerably. Delamination sequences captured by HSC, and the amount of load drop show

that delamination is highly dynamic and unstable in nature for these cases. Delamination initiation locations and propagation patterns are correctly predicted by cohesive zone modeling for these cases. An overall good correlation with experimental results is found despite underestimating the delamination growth rate and initiation load in finite element results.

For specimens in which continuous layers exist between the drop-offs plies, the nominal interface properties determined by standard tests resulted in a premature opening mode which is not observed in HSC images. Preventing this unobserved damage by enhancement of interface strength pairs in cohesive zone modeling, the predicted results are significantly improved in terms of both delamination loads and locations for these configurations.

A set of analyses with a modified cohesive strength pair is also carried out for all specimen types. A relatively low increase in delamination onset loads in new results shows that the configurations with consecutive drop-offs can be categorized as fracture toughness dominant types. Despite a similar trend in delamination initiation load for configuration U-4, such a conclusion can not be made since the delamination characteristics are significantly changed by updating the strength pair. However, the configuration U-5, can be identified as the strength-dominant case, where the load at delamination onset considerably increases by using enhanced cohesive strength pair. Despite a good agreement between the results of finite element modeling and experiments, further studies are required to develop a methodology for a better assessment of delamination characteristics of tapered laminates.

It can also be concluded that the simulation of dynamic characteristics of delamination using cohesive zone modeling by dynamic explicit analysis is effective when the delamination growth rates are higher than the loading rate. However, to obtain more accurate results in the delamination growth rate for the cases with stable growth behavior, real simulation times are required, which may not be computationally affordable.

In order to comprehend the dynamic delamination behavior and load transfer mechanisms, two and three-dimensional models are constructed for tapered laminates consisting of single, double, and triple drop-offs. Combinations of unidirectional plies

with 0° and 45° orientations for the belt, core, and dropped sub-laminates are considered. For each case, damage evolution is correlated to the load-displacement graph of the simulation and stress state in delamination locations. The damage status and effective stress states before and after the first load drop are shown for each case. Also, crack extension and crack tip speeds versus time diagrams are obtained. The following judgments can be made for the parametric study carried out in this thesis:

- A failure in the vertical interface between a resin pocket and the neighboring drop-off ply seems to have no contribution on load drops in load-displacement curves, but it effects the propagation pattern.
- In all cases involving 45° drop-off plies, the initial stiffness (stiffness at the beginning of loading) is slightly less than the stiffness of the laminates with all plies of 0° . This implies that the contribution of drop-offs in overall stiffness of the laminate is not significant. After sequences of load drops, the stiffnesses for both layups completely match, since 0° belt and core, which are identical in both cases carry the significant portion of the load.
- Laminates with 45° core or belt have almost the same stiffness, considerably lower than the laminates with all 0° plies, which implies that belt and core sub-laminates have significant contribution on the overall stiffness of the laminate.
- For laminates with two and three drop-offs, the corner of second resin pocket (corner toward thin section) is found to be most critical than the corner of first resin pocket. However, in all laminates with two drop-offs delamination propagate along the interface below first resin pocket and toward thin section, while in laminates with three drop-offs, except laminate with 45° belt, the crack propagates above the resin pocket toward both thin and thick sections.
- There is a load drop observed in later stages of loading for all laminates having 45° belt which is not detected in other cases.
- Before damage initiation, stresses are highly non-uniform but they become more uniform after damage occurs and propagates.
- In most cases (except 3-drop-off case with 45° drop-off plies) the first crack

initiates in the upper resin pocket/belt interface and its propagation ceases after a while and it resumes after delaminations at other locations.

- The crack in the interface between the upper drop-off and the belt is very slow in all cases. In cases with 45° drop-off plies, all cracks start almost simultaneously while in other cases the time interval between each crack is comparatively larger.

REFERENCES

- [1] B. O. Yavuz, “Interlaminar tensile strength and mode i fracture toughness of different angle-ply cfrp and gfrp composite laminates,” *Master Thesis, Middle East Technical University*, 2019.
- [2] A. Albanesi, F. Bre, V. Fachinotti, and C. Gebhardt, “Simultaneous ply-order, ply-number and ply-drop optimization of laminate wind turbine blades using the inverse finite element method,” *Composite Structures*, vol. 184, pp. 894–903, 2018.
- [3] M. K. Dhadwal, S. N. Jung, and T. J. Kim, “Evolutionary shape optimization of flexbeam sections of a bearingless helicopter rotor,” *Composites Research*, vol. 27, no. 6, pp. 207–212, 2014.
- [4] S. Sridharan, *Delamination behaviour of composites*. Elsevier, 2008.
- [5] Abaqus, “Analysis user’s guide,” vol. IV, pp. 32.5.6–5, 2016.
- [6] P. W. Harper and S. R. Hallett, “Cohesive zone length in numerical simulations of composite delamination,” *Engineering Fracture Mechanics*, vol. 75, no. 16, pp. 4774–4792, 2008.
- [7] G. B. Murri and J. R. Schaff, “Fatigue life methodology for tapered hybrid composite flexbeams,” *Composites science and technology*, vol. 66, no. 3-4, pp. 499–508, 2006.
- [8] K. W. Gan, G. Allegri, and S. R. Hallett, “A simplified layered beam approach for predicting ply drop delamination in thick composite laminates,” *Materials & Design*, vol. 108, pp. 570–580, 2016.
- [9] W. Cui, M. R. Wisnom, and M. Jones, “New model to predict static strength of tapered laminates,” *Composites*, vol. 26, no. 2, pp. 141–146, 1995.

- [10] M. R. Wisnom, M. Jones, and W. Cui, "Failure of tapered composites under static and fatigue tension loading," *AIAA journal*, vol. 33, no. 5, pp. 911–918, 1995.
- [11] M. R. Wisnom, R. Dixon, and G. Hill, "Delamination in asymmetrically tapered composites loaded in tension," *Composite structures*, vol. 35, no. 3, pp. 309–322, 1996.
- [12] B. Varughese and A. Mukherjee, "Analysis of tapered laminated composites with non-symmetric lay-up," *Journal of reinforced plastics and composites*, vol. 16, no. 7, pp. 631–660, 1997.
- [13] A. D. Botting, A. J. Vizzini, and S. W. Lee, "Effect of ply-drop configuration on delamination strength of tapered composite structures," *AIAA journal*, vol. 34, no. 8, pp. 1650–1656, 1996.
- [14] B. Vidyashankar and A. K. Murty, "Analysis of laminates with ply drops," *Composites science and technology*, vol. 61, no. 5, pp. 749–758, 2001.
- [15] L. Kawashita, M. Jones, S. Giannis, S. Hallett, and M. Wisnom, "High fidelity modelling of tapered laminates with internal ply terminations," in *18th International Conference on Composite Materials (ICCM), Jeju Island*, 2011.
- [16] E. A. Armanios and L. Parnas, "Delamination analysis of tapered laminated composites under tensile loading," in *Composite Materials: Fatigue and Fracture (Third Volume)*, ASTM International, 1991.
- [17] P. N. Harrison and E. R. Johnson, "A mixed variational formulation for interlaminar stresses in thickness-tapered composite laminates," *International journal of solids and structures*, vol. 33, no. 16, pp. 2377–2399, 1996.
- [18] A. Mukherjee and B. Varughese, "Development of a specialised finite element for the analysis of composite structures with ply drop-off," *Composite structures*, vol. 46, no. 1, pp. 1–16, 1999.
- [19] B. R. Trethewey Jr and J. W. Gillespie Jr, "Plate theory model for thickness tapered composite laminates," *Journal of reinforced plastics and composites*, vol. 20, no. 2, pp. 105–128, 2001.

- [20] K. He, R. Ganesan, and S. Hoa, "Modified shear-lag model for analysis of a composite laminate with drop-off plies," *Composites science and technology*, vol. 63, no. 10, pp. 1453–1462, 2003.
- [21] K. He, S. Hoa, and R. Ganesan, "Stress analysis of tapered composite laminates using partial hybrid finite elements," *Journal of reinforced plastics and composites*, vol. 23, no. 6, pp. 589–599, 2004.
- [22] H. S. Kim, S. Y. Rhee, and M. Cho, "Simple and efficient interlaminar stress analysis of composite laminates with internal ply-drop," *Composite Structures*, vol. 84, no. 1, pp. 73–86, 2008.
- [23] G. Allegri, M. Wisnom, and S. Hallett, "A simplified approach to the damage tolerance design of asymmetric tapered laminates. part i: Methodology development," *Composites Part A: Applied Science and Manufacturing*, vol. 41, no. 10, pp. 1388–1394, 2010.
- [24] E. Zappino, A. Viglietti, and E. Carrera, "Analysis of tapered composite structures using a refined beam theory," *Composite Structures*, vol. 183, pp. 42–52, 2018.
- [25] S. Obata, K. Takahashi, and K. Inaba, "Laminate design for a tapered frp structure with ply drop-off based on yielding of resin pockets," *Composite Structures*, vol. 253, p. 112787, 2020.
- [26] K. He, S. Hoa, and R. Ganesan, "The study of tapered laminated composite structures: a review," *Composites Science and Technology*, vol. 60, no. 14, pp. 2643–2657, 2000.
- [27] P. Dhurvey and N. Mittal, "Review on various studies of composite laminates with ply drop-off," *ARPJ Journal of Engineering and Applied Sciences*, vol. 8, no. 8, pp. 595–605, 2013.
- [28] J. Daoust and S. Hoa, "Parameters affecting interlaminar stresses in tapered laminates under static loading conditions," *Polymer Composites*, vol. 10, no. 5, pp. 374–383, 1989.

- [29] W. Cui, M. R. Wisnom, and M. Jones, "Effect of step spacing on delamination of tapered laminates," *Composites science and technology*, vol. 52, no. 1, pp. 39–46, 1994.
- [30] Z. Petrossian and M. R. Wisnom, "Parametric study of delamination in composites with discontinuous plies using an analytical solution based on fracture mechanics," *Composites Part A: Applied Science and Manufacturing*, vol. 29, no. 4, pp. 403–414, 1998.
- [31] A. Mukherjee and B. Varughese, "Design guidelines for ply drop-off in laminated composite structures," *Composites Part B: Engineering*, vol. 32, no. 2, pp. 153–164, 2001.
- [32] F.-X. Irisarri, A. Lasseigne, F.-H. Leroy, and R. Le Riche, "Optimal design of laminated composite structures with ply drops using stacking sequence tables," *Composite Structures*, vol. 107, pp. 559–569, 2014.
- [33] A. Turon, P. Camanho, J. Costa, and J. Renart, "Accurate simulation of delamination growth under mixed-mode loading using cohesive elements: definition of interlaminar strengths and elastic stiffness," *Composite structures*, vol. 92, no. 8, pp. 1857–1864, 2010.
- [34] P. W. Harper, L. Sun, and S. R. Hallett, "A study on the influence of cohesive zone interface element strength parameters on mixed mode behaviour," *Composites Part A: Applied Science and Manufacturing*, vol. 43, no. 4, pp. 722–734, 2012.
- [35] O. Celik and L. Parnas, "Maximization of ultimate strength of unidirectional tapered composite structures considering different failure modes," in *58th AIAA/ASCE/AHS/ASC Structures, Structural Dynamics, and Materials Conference*, p. 0893, 2017.
- [36] P. W. Harper and S. R. Hallett, "Advanced numerical modelling techniques for the structural design of composite tidal turbine blades," *Ocean Engineering*, vol. 96, pp. 272–283, 2015.
- [37] H. Abdulhamid, C. Bouvet, L. Michel, J. Aboissiere, and C. Minot, "Numerical simulation of impact and compression after impact of asymmetrically tapered

- laminated cfrp,” *International Journal of Impact Engineering*, vol. 95, pp. 154–164, 2016.
- [38] J. Bender, S. Hallett, and E. Lindgaard, “Parametric study of the effect of wrinkle features on the strength of a tapered wind turbine blade sub-structure,” *Composite Structures*, vol. 218, pp. 120–129, 2019.
- [39] B. Zhang, L. F. Kawashita, M. I. Jones, J. K. Lander, and S. R. Hallett, “An experimental and numerical investigation into damage mechanisms in tapered laminates under tensile loading,” *Composites Part A: Applied Science and Manufacturing*, p. 105862, 2020.
- [40] K. W. Gan, S. R. Hallett, and M. R. Wisnom, “Measurement and modelling of interlaminar shear strength enhancement under moderate through-thickness compression,” *Composites Part A: Applied Science and Manufacturing*, vol. 49, pp. 18–25, 2013.
- [41] R. Sepasdar and M. Shakiba, “Overcoming the convergence difficulty of cohesive zone models through a newton-raphson modification technique,” *Engineering Fracture Mechanics*, vol. 233, p. 107046, 2020.
- [42] A. Tabiei and W. Zhang, “Composite laminate delamination simulation and experiment: A review of recent development,” *Applied Mechanics Reviews*, vol. 70, no. 3, 2018.
- [43] F. Van der Meer, N. Moës, and L. Sluys, “A level set model for delamination—modeling crack growth without cohesive zone or stress singularity,” *Engineering Fracture Mechanics*, vol. 79, pp. 191–212, 2012.
- [44] R. Krueger, “The virtual crack closure technique for modeling interlaminar failure and delamination in advanced composite materials,” in *Numerical modelling of failure in advanced composite materials*, pp. 3–53, Elsevier, 2015.
- [45] P. Camanho and F. Matthews, “Delamination onset prediction in mechanically fastened joints in composite laminates,” *Journal of Composite Materials*, vol. 33, no. 10, pp. 906–927, 1999.

- [46] C. G. Dávila and E. R. Johnson, “Analysis of delamination initiation in post-buckled dropped-ply laminates,” *AIAA journal*, vol. 31, no. 4, pp. 721–727, 1993.
- [47] A. Turon, P. P. Camanho, A. Soto, and E. V. González, “8.8 analysis of delamination damage in composite structures using cohesive elements,” 2018.
- [48] G. Alfano, “On the influence of the shape of the interface law on the application of cohesive-zone models,” *Composites Science and Technology*, vol. 66, no. 6, pp. 723–730, 2006.
- [49] K. Park, G. H. Paulino, and J. R. Roesler, “A unified potential-based cohesive model of mixed-mode fracture,” *Journal of the Mechanics and Physics of Solids*, vol. 57, no. 6, pp. 891–908, 2009.
- [50] A. D 5528-13, “Standard test method for mode i interlaminar fracture toughness of unidirectional fiber-reinforced polymer matrix composites,” tech. rep., ASTM, 2013.
- [51] A. D 7905 / D7905M 19e1, “Standard test method for determination of the mode ii interlaminar fracture toughness of unidirectional fiber-reinforced polymer matrix composites,” tech. rep., ASTM, 2019.
- [52] A. D 6415 / D6415M 06a, “Standard test method for measuring the curved beam strength of a fiber-reinforced polymer-matrix composite,” tech. rep., ASTM, 2013.
- [53] A. D 2344 / D2344M 16, “Standard test method for short-beam strength of polymer matrix composite materials and their laminates,” tech. rep., ASTM, 2016.
- [54] S. Pinho, L. Iannucci, and P. Robinson, “Formulation and implementation of decohesion elements in an explicit finite element code,” *Composites Part A: Applied science and manufacturing*, vol. 37, no. 5, pp. 778–789, 2006.
- [55] P. P. Camanho, C. G. Davila, and M. De Moura, “Numerical simulation of mixed-mode progressive delamination in composite materials,” *Journal of composite materials*, vol. 37, no. 16, pp. 1415–1438, 2003.

- [56] A. C. Orifici, I. Herszberg, and R. S. Thomson, "Review of methodologies for composite material modelling incorporating failure," *Composite structures*, vol. 86, no. 1-3, pp. 194–210, 2008.
- [57] I. Abaqus, "Abaqus documentation," *Version*, vol. 6, pp. 1–5, 2014.
- [58] M. L. Benzeggagh and M. Kenane, "Measurement of mixed-mode delamination fracture toughness of unidirectional glass/epoxy composites with mixed-mode bending apparatus," *Composites science and technology*, vol. 56, no. 4, pp. 439–449, 1996.
- [59] A. Soto, E. González, P. Maimí, A. Turon, J. S. de Aja, and F. de la Escalera, "Cohesive zone length of orthotropic materials undergoing delamination," *Engineering Fracture Mechanics*, vol. 159, pp. 174–188, 2016.
- [60] A. Turon, C. G. Davila, P. P. Camanho, and J. Costa, "An engineering solution for mesh size effects in the simulation of delamination using cohesive zone models," *Engineering fracture mechanics*, vol. 74, no. 10, pp. 1665–1682, 2007.
- [61] Q. Yang and B. Cox, "Cohesive models for damage evolution in laminated composites," *International Journal of Fracture*, vol. 133, no. 2, pp. 107–137, 2005.
- [62] Q. Yang, B. N. Cox, R. K. Nalla, and R. Ritchie, "Fracture length scales in human cortical bone: the necessity of nonlinear fracture models," *Biomaterials*, vol. 27, no. 9, pp. 2095–2113, 2006.
- [63] A. Turon, E. González, C. Sarrado, G. Guillaumet, and P. Maimí, "Accurate simulation of delamination under mixed-mode loading using a cohesive model with a mode-dependent penalty stiffness," *Composite Structures*, vol. 184, pp. 506–511, 2018.
- [64] P. Maimi, J. Mayugo, and P. Camanho, "A three-dimensional damage model for transversely isotropic composite laminates," *Journal of Composite Materials*, vol. 42, no. 25, pp. 2717–2745, 2008.
- [65] I. Lapczyk and J. A. Hurtado, "Progressive damage modeling in fiber-reinforced materials," *Composites Part A: Applied Science and Manufacturing*, vol. 38, no. 11, pp. 2333–2341, 2007.

- [66] Abaqus, “Analysis user’s guide,” vol. IV, p. 13.2.1, 2016.
- [67] Abaqus, “Abaqus documentation,” *Version*, vol. 2, pp. 10–40, 2016.
- [68] I. Abaqus, “Abaqus user,” vol. 3, pp. 15–50, 2016.
- [69] C. Yu, A. Pandolfi, M. Ortiz, D. Coker, and A. Rosakis, “Three-dimensional modeling of intersonic shear-crack growth in asymmetrically loaded unidirectional composite plates,” *International Journal of Solids and Structures*, vol. 39, no. 25, pp. 6135–6157, 2002.
- [70] M. R. Wisnom and M. Jones, “Size effects in interlaminar tensile and shear strength of unidirectional glass fibre/epoxy,” *Journal of reinforced plastics and composites*, vol. 15, no. 1, pp. 2–15, 1996.
- [71] S. W. Smith, “Chapter 15 - moving average filters,” *Digital Signal Processing*, pp. 277–284, 2003.

Appendix A

```
! *****3D Hashin
subroutine vumat (
C Read only -
* nblock, ndir, nshr, nstatev, nfieldv, nprops, lanneal,
* stepTime, totalTime, dt, cmname, coordMp, charLength,
* props, density, strainInc, relSpinInc,
* tempOld, stretchOld, defgradOld, fieldOld,
* stressOld, stateOld, enerInternOld, enerInelasOld,
* tempNew, stretchNew, defgradNew, fieldNew,
C Write only -
* stressNew, stateNew, enerInternNew, enerInelasNew )
C
include 'vaba_param.inc'
C
dimension coordMp(nblock,*), charLength(nblock), props(nprops),
1 density(nblock), strainInc(nblock,ndir+nshr),
2 relSpinInc(nblock,nshr), tempOld(nblock),
3 stretchOld(nblock,ndir+nshr),
4 defgradOld(nblock,ndir+nshr+nshr),
5 fieldOld(nblock,nfieldv), stressOld(nblock,ndir+nshr),
6 stateOld(nblock,nstatev), enerInternOld(nblock),
7 enerInelasOld(nblock), tempNew(nblock),
8 stretchNew(nblock,ndir+nshr),
9 defgradNew(nblock,ndir+nshr+nshr),
```

```

1 fieldNew(nblock,nfieldv),
2 stressNew(nblock,ndir+nshr), stateNew(nblock,nstatev),
3 enerInternNew(nblock), enerInelasNew(nblock)
C
character*80 cmname
! **Definition of Parameters
parameter (ONE=1.d0,TWO=2.d0,ZERO=0.d0,HALF=0.5d0,
TOLERANCE=1.d-12)
! ** Definition of Arrays and Material Constants
real E1,E2,E3,G12,G13,G23,XT,XC,YT,YC,ST,SL,GFT,GFC,GMT,GMC,GSH
real NU12,NU13,NU23,NU21,NU31,NU32,density
real EPS11,EPS22,EPS33,EPS12,EPS23,EPS13
real dEPS11,dEPS22,dEPS33,dEPS12,dEPS23,dEPS13
real delta,DEG1,DEG2,DEG3,DEG4,DEG5,DEG6, new_energy
real DF,DM1,DM2,DS1,DS3,DS2_22,DS2_33,DS2,temp
real T1,T2,T3,T12,T23,T13,G
real STIFFNESS(9)
! **Definition of Material Properties
E1=props(1)! Modulus of Elasticity in Fiber Direction
E2=props(2)! Modulus of Elasticity in Transverse Direction
E3=props(3)! Modulus of Elasticity in Thickness Direction
G12=props(4)! Shear Modulus in 12 Plane
G13=props(5)! Shear Modulus in 13 Plane
G23=props(6)! Shear Modulus in 23 Plane
NU12=props(7)! Poisson 12
NU13=props(8)! Poisson 13
NU23=props(9)! Poisson 23
XT=props(10)! Fiber Tensile Strength
XC=props(11)! Fiber Compression Strength
YT=props(12)! Matrix Tensile Strength
YC=props(13)! Matrix Compression Strength
SL=props(14)! Shear 1 Strength
ST=props(15)! Shear 2 Strength

```

```

GFT=props(16) ! Fracture Energy Fiber Tensile
GFC=props(17) ! Fracture Energy Fiber Compression
GMT=props(18) ! Fracture Energy Matrix Tension
GMC=props(19) ! Fracture Energy Matrix Compression
GSH=props(20) ! Fracture Energy in Shear
NU21=NU12*(E2/E1)! Poisson 21
NU31=NU13*(E3/E1)! Poisson 31
NU32=NU23*(E3/E2)! Poisson 32
! **Definition of Stiffness Matrix
delta=ONE - (NU32*NU23) - (NU31*NU13) - (NU12*NU21)-
(TWO*NU13*NU21*NU32)
C
STIFFNESS(1)=(E1*(ONE - NU32*NU23)) / delta
STIFFNESS(2)=(E2*(ONE - NU13*NU31)) / delta
STIFFNESS(3)=(E3*(ONE - NU12*NU21)) / delta
STIFFNESS(4)=(E1*((NU31*NU23)+NU21)) / delta
STIFFNESS(5)=(E2*((NU12*NU31)+NU32)) / delta
STIFFNESS(6)=(E1*((NU21*NU32)+NU31)) / delta
STIFFNESS(7)=G12
STIFFNESS(8)=G23
STIFFNESS(9)=G13
! **Check if element failure occurred
do k=1,nblock
C if (stateNew(k,29) .eq. ZERO) then
C go to 1000
C end if
! ** Check if it is the beginning of analysis
if ( stepTime .eq. ZERO ) then
! ** Update Strains
stateNew(k,1)=strainInc(k,1)+stateOld(k,1)
stateNew(k,2)=strainInc(k,2)+stateOld(k,2)
stateNew(k,3)=strainInc(k,3)+stateOld(k,3)
stateNew(k,4)=strainInc(k,4)+stateOld(k,4)

```

```

stateNew(k,5)=strainInc(k,5)+stateOld(k,5)
stateNew(k,6)=strainInc(k,6)+stateOld(k,6)
! ** Assign updated Strain
EPS11=stateNew(k,1)
EPS22=stateNew(k,2)
EPS33=stateNew(k,3)
EPS12=stateNew(k,4)
EPS23=stateNew(k,5)
EPS13=stateNew(k,6)
! ** Update Stresses at t=0
stressNew(k,1)= (STIFFNESS(1)*EPS11) + (STIFFNESS(4)*EPS22)
+(STIFFNESS(6)*EPS33)

stressNew(k,2)= (STIFFNESS(4)*EPS11) + (STIFFNESS(2)*EPS22)
+(STIFFNESS(5)*EPS33)

stressNew(k,3)= (STIFFNESS(6)*EPS11) + (STIFFNESS(5)*EPS22)
+(STIFFNESS(3)*EPS33)

stressNew(k,4)= STIFFNESS(7)*EPS12
stressNew(k,5)= STIFFNESS(8)*EPS23
stressNew(k,6)= STIFFNESS(9)*EPS13
! **Updated all state variables for step time .ne. ZERO
else
! **Updated Strain State Variables
stateNew(k,1)=stateold(k,1)! strain EPS11
stateNew(k,2)=stateold(k,2)! strain EPS22
stateNew(k,3)=stateold(k,3)! strain EPS33
stateNew(k,4)=stateold(k,4)! strain EPS12
stateNew(k,5)=stateold(k,5)! strain EPS23
stateNew(k,6)=stateold(k,6)! strain EPS13
! ** Updated Damage Variables
stateNew(k,7)=stateold(k,7)! Damage variable DF

```



```

stateNew(k,8)=stateold(k,8)! Damage variable DM1
stateNew(k,9)=stateold(k,9)! Damage variable DM2
stateNew(k,10)=stateold(k,10)! Damage variable DS1
stateNew(k,11)=stateold(k,11)! Damage variable DS2
stateNew(k,12)=stateold(k,12)! Damage variable DS3
stateNew(k,13)=stateold(k,13)! Overall Damage
! ** Updated Failure Strain
stateNew(k,14)=stateold(k,14)! Strain Criterion 1
stateNew(k,15)=stateold(k,15)! Strain Criterion 2
stateNew(k,16)=stateold(k,16)! Strain Criterion 3
stateNew(k,17)=stateold(k,17)! Strain Criterion 4
stateNew(k,18)=stateold(k,18)! Strain Criterion 5
stateNew(k,19)=stateold(k,19)! Strain Criterion 5
! ** Updated Failure Criterion Stress
stateNew(k,20)=stateold(k,20)! Stress Criterion 1
stateNew(k,21)=stateold(k,21)! Stress Criterion 2
stateNew(k,22)=stateold(k,22)! Stress Criterion 3
stateNew(k,23)=stateold(k,23)! Stress Criterion 4
stateNew(k,24)=stateold(k,24)! Stress Criterion 5
stateNew(k,25)=stateold(k,25)! Stress Criterion 6
! ** Updated Damage
stateNew(k,26)=stateold(k,26)! Fiber Failure Index
stateNew(k,27)=stateold(k,27)! Matrix Failure Index in Direction 2
stateNew(k,28)=stateold(k,28)! Matrix Failure Index in Direction 3
! ** Updated Element Deletion Control
stateNew(k,29)=stateold(k,29)
! ** Assign New Strains to Updated state variable
stateNew(k,1)=strainInc(k,1)+stateOld(k,1)
stateNew(k,2)=strainInc(k,2)+stateOld(k,2)
stateNew(k,3)=strainInc(k,3)+stateOld(k,3)
stateNew(k,4)=strainInc(k,4)+stateOld(k,4)
stateNew(k,5)=strainInc(k,5)+stateOld(k,5)
stateNew(k,6)=strainInc(k,6)+stateOld(k,6)

```

```

! ** Check if no Damage Occured
  if (stateOld(k,13).eq.ZERO) then
! ***** Read Strain
EPS11=stateNew(k,1)
EPS22=stateNew(k,2)
EPS33=stateNew(k,3)
EPS12=stateNew(k,4)
EPS23=stateNew(k,5)
EPS13=stateNew(k,6)
! ** Updated Stresses
stressNew(k,1)= (STIFFNESS(1)*EPS11) + (STIFFNESS(4)*EPS22) +
(STIFFNESS(6)*EPS33)

stressNew(k,2)= (STIFFNESS(4)*EPS11) + (STIFFNESS(2)*EPS22) +
(STIFFNESS(5)*EPS33)

stressNew(k,3)= (STIFFNESS(6)*EPS11) + (STIFFNESS(5)*EPS22) +
(STIFFNESS(3)*EPS33)

stressNew(k,4)= STIFFNESS(7)*EPS12
stressNew(k,5)= STIFFNESS(8)*EPS23
stressNew(k,6)= STIFFNESS(9)*EPS13
! ** Check for Fiber Tension Damage (Hashin Criterion)
  if (stressNew(k,1) .gt. ZERO) then
    if (((stressNew(k,1)/(XT))**TWO) .gt. ONE) then
stateNew(k,13)=ONE
stateNew(k,26)=ONE
    end if
  else
! ** Check for Fiber Compression Damage (Hashin Criterion)
    if (((stressNew(k,1)/(XC))**TWO) .gt. ONE) then
stateNew(k,13)=ONE
stateNew(k,26)=ONE

```

```

end if
end if
! ** Check for Matrix Tension Damage (Hashin Criterion)
if (stressNew(k,2) .gt. ZERO) then
if (((EPS22/(YT/E2))**TWO) + ((TWO*EPS12/(SL/G12))**TWO) +
((TWO*EPS23/(ST/G23))**TWO)) .gt. ONE) then
stateNew(k,13)=ONE
stateNew(k,27)=ONE
end if
else
! ** Check for Matrix Compression Damage (Hashin Criterion)
if (((EPS22/(YC/E2))**TWO) + ((TWO*EPS12/(SL/G12))**TWO) +
((TWO*EPS23/(ST/G23))**TWO)) .gt. ONE) then
stateNew(k,13)=ONE
stateNew(k,27)=ONE
end if
end if
! ** Check for Out-of-Plane Matrix Tension Damage
! ** (starain Criterion)
if (stressNew(k,3) .gt. ZERO) then
if (((EPS33/(YT/E3))**TWO) + ((TWO*EPS13/(ST/G13))**TWO) +
((TWO*EPS23/(ST/G23))**TWO)) .gt. ONE) then
stateNew(k,13)=ONE
stateNew(k,28)=ONE
end if
else
! ** Check for Out-of-Plane Matrix Compression Damage
! ** (starain Criterion)
if (((EPS33/(YC/E3))**TWO) + ((TWO*EPS13/(ST/G13))**TWO) +
((TWO*EPS23/(ST/G23))**TWO)) .gt. ONE) then
stateNew(k,13)=ONE
stateNew(k,28)=ONE
end if

```

```

end if
! ** Update Criterion Variables
! if first criteria fails
  if (stateNew(k,26) .eq. ZERO) then
stateNew(k,14)=abs(EPS11)
stateNew(k,20)=abs(stressNew(k,1))
end if
! if second criteria fails
if (stateNew(k,27) .eq. ZERO) then
stateNew(k,15)=abs(EPS22)
stateNew(k,17)=abs(EPS12)
stateNew(k,18)=abs(EPS23)
stateNew(k,21)=abs(stressNew(k,2))
stateNew(k,23)=abs(stressNew(k,4))
stateNew(k,24)=abs(stressNew(k,5))
end if
! if thired criteria fails
if (stateNew(k,28) .eq. ZERO) then
stateNew(k,16)=abs(EPS33)
stateNew(k,19)=abs(EPS13)
stateNew(k,18)=abs(EPS23)
stateNew(k,22)=abs(stressNew(k,3))
stateNew(k,25)=abs(stressNew(k,6))
stateNew(k,24)=abs(stressNew(k,5))
  end if
end if
! ** Damage is equal to ZERO Until Here
! ** Check if Damage Occurred
  if (stateNew(k,13).ne.ZERO) then
! ** Compute Damage Variables
DF=ZERO
DM1=ZERO
DM2=ZERO

```

```

DS1=ZERO
DS2_22=ZERO
DS2_33=ZERO
DS2=ZERO
DS3=ZERO
! ** First Failure
  if (stateNew(k,26) .eq. ONE )then
! ** if Fiber Tensile
  if (stateNew(k,1).gt.ZERO) then
G=GFT
! ** if Fiber Compression
  else
G=GFC
  end if
T1=stateNew(k,20)
dEPS11=abs(stateNew(k,1)) - stateNew(k,14)
  if (dEPS11 .gt. TOLERANCE) then
  if (dEPS11 .lt. (TWO*G/(charLength(k)*T1))) then
temp=(T1/(dEPS11*E1)) - ((charLength(k)*(T1**TWO)*HALF)/(G*E1))
DF=ONE/(ONE+temp)
  else
DF=ONE
  end if
  end if
  end if
! ** if Matrix Tensile
  if (stateNew(k,27) .eq. ONE )then
  if (stateNew(k,2).gt.ZERO) then
G=GMT
! ** if Matrix Compression
  else
G=GMC
  end if

```

```

T2=stateNew(k,21)
T12=stateNew(k,23)
T23=stateNew(k,24)
dEPS22=abs(stateNew(k,2)) - stateNew(k,15)
dEPS12=abs(stateNew(k,4)) - stateNew(k,17)
dEPS23=abs(stateNew(k,5)) - stateNew(k,18)
  if (dEPS22 .gt. TOLERANCE) then
    if (dEPS22 .lt. (TWO*G/(charLength(k)*T2))) then
temp=(T2/(dEPS22*E2)) - ((charLength(k) *
(T2**TWO)*HALF)/(G*E2))
DM1=ONE/(ONE+temp)
    else
DM1=ONE
    end if
  end if
  if (dEPS12 .gt. TOLERANCE) then
    if (dEPS12 .lt. (TWO*GSH/(charLength(k)*T12))) then
temp=(T12/(dEPS12*G12)) - ((charLength(k) * (T12**TWO) *
HALF)/(GSH*G12))
DS1=ONE/(ONE+temp)
    else
DS1=ONE
    end if
  end if
  if (dEPS23 .gt. TOLERANCE) then
    if (dEPS23 .lt. (TWO*GSH/(charLength(k)*T23))) then
temp=(T23/(dEPS23*G23)) - ((charLength(k) * (T23**TWO) *
HALF)/(GSH*G23))
DS2_22=ONE/(ONE+temp)
    else
DS2_22=ONE
    end if
  end if

```

```

end if

if (stateNew(k,28) .eq. ONE ) then
  if (stateNew(k,3) .gt. ZERO) then
G=GMT
  else
G=GMC
  end if
T3=stateNew(k,22)
T23=stateNew(k,24)
T13=stateNew(k,25)
dEPS33=abs(stateNew(k,3)) - stateNew(k,16)
dEPS23=abs(stateNew(k,5)) - stateNew(k,18)
dEPS13=abs(stateNew(k,6)) - stateNew(k,19)
  if (dEPS33 .gt. TOLERANCE) then
    if (dEPS33 .lt. (TWO*G/(charLength(k)*T3))) then
temp=(T3/(dEPS33*E3)) - ((charLength(k) * (T3**TWO) *
HALF) / (G*E3))

DM2=ONE/(ONE+temp)
    else
DM2=ONE
    end if
  end if
  if (dEPS23.gt.TOLERANCE) then
    if (dEPS23 .lt. (TWO*GSH/(charLength(k)*T23))) then
temp=(T23/(dEPS23*G23)) - ((charLength(k) * (T23**TWO) *
HALF) / (GSH*G23))

DS2_33=ONE/(ONE+temp)
    else
DS2_33=ONE
    end if

```

```

end if
if ((dEPS13 .gt. TOLERANCE)) then
if (dEPS13 .lt. (TWO*GSH/(charLength(k)*T13))) then
temp=(T13/(dEPS13*G13))-((charLength(k)*(T13**TWO)*
HALF)/(GSH*G13))

DS3=ONE/(ONE+temp)
else
DS3=ONE
end if
end if
end if
DS2=max(DS2_22,DS2_33)

stateNew(k,7)=max(DF,stateOld(k,7))
stateNew(k,8)=max(DM1,stateOld(k,8))
stateNew(k,9)=max(DM2,stateOld(k,9))
temp=ONE-stateNew(k,7)

stateNew(k,10)=max(stateOld(k,10),(ONE-(temp*
(ONE-stateNew(k,8))*(ONE-DS1))))

stateNew(k,11)=max(stateOld(k,11),(ONE-(temp*
(ONE-stateNew(k,8))*(ONE-stateNew(k,9))*(ONE-DS2))))

stateNew(k,12)=max(stateOld(k,12),(ONE-(temp*
(ONE-stateNew(k,9))*(ONE-DS3))))

stateNew(k,13)=ONE
! ** Update Stifness Matrix
DEG1=ONE-stateNew(k,7)
DEG2=ONE-stateNew(k,8)
DEG3=ONE-stateNew(k,9)

```



```

DEG4=ONE-stateNew(k,10)
DEG5=ONE-stateNew(k,11)
DEG6=ONE-stateNew(k,12)

delta=ONE - (DEG2*DEG3*NU32*NU23) - (DEG1*DEG3*NU31*NU13) -
(DEG1*DEG2*NU12*NU21) - (TWO*DEG1*DEG2*DEG3*NU13*NU21*NU32)

STIFFNESS(1)=(DEG1*E1*(ONE-(DEG2*DEG3*NU32*NU23)))/delta
STIFFNESS(2)=(DEG2*E2*(ONE-(DEG1*DEG3*NU13*NU31)))/delta
STIFFNESS(3)=(DEG3*E3*(ONE-(DEG1*DEG2*NU12*NU21)))/delta
STIFFNESS(4)=(DEG1*DEG2*E1*((DEG3*NU31*NU23)+NU21))/delta
STIFFNESS(5)=(DEG2*DEG3*E2*((DEG1*NU12*NU31)+NU32))/delta
STIFFNESS(6)=(DEG1*DEG3*E1*((DEG2*NU21*NU32)+NU31))/delta
STIFFNESS(7)=DEG4*G12
STIFFNESS(8)=DEG5*G23
STIFFNESS(9)=DEG6*G13
! ** Update Strain
EPS11=stateNew(k,1)
EPS22=stateNew(k,2)
EPS33=stateNew(k,3)
EPS12=stateNew(k,4)
EPS23=stateNew(k,5)
EPS13=stateNew(k,6)

stressNew(k,1)=(STIFFNESS(1)*EPS11) + (STIFFNESS(4)*EPS22)
+(STIFFNESS(6)*EPS33)
stressNew(k,2)=(STIFFNESS(4)*EPS11) + (STIFFNESS(2)*EPS22)
+(STIFFNESS(5)*EPS33)
stressNew(k,3)=(STIFFNESS(6)*EPS11) + (STIFFNESS(5)*EPS22)
+(STIFFNESS(3)*EPS33)
stressNew(k,4)= STIFFNESS(7)*EPS12
stressNew(k,5)= STIFFNESS(8)*EPS23
stressNew(k,6)= STIFFNESS(9)*EPS13

```

```

! ** Check for Critical Damage
  if (stateNew(k,26) .eq. ZERO) then
  if (EPS11 .gt. ZERO) then
  if (((EPS11/(XT/E1))**TWO) .gt. ONE) then
stateNew(k,13)=ONE
stateNew(k,26)=ONE
  end if
  else
  if (((EPS11/(XC/E1))**TWO) .gt. ONE) then
stateNew(k,13)=ONE
stateNew(k,26)=ONE
  end if
  end if
  end if

  if (stateNew(k,27) .eq. ZERO) then
  if (EPS22 .gt. ZERO) then
  if (((EPS22/(YT/E2))**TWO) + ((TWO*EPS12/(SL/G12))**TWO)
  + ((TWO*EPS23/(ST/G23))**TWO)) .gt. ONE) then
stateNew(k,13)=ONE
stateNew(k,27)=ONE
  end if
  else
  if (((EPS22/(YC/E2))**TWO) + ((TWO*EPS12/(SL/G12))**TWO)
  + ((TWO*EPS23/(ST/G23))**TWO)) .gt. ONE) then
stateNew(k,13)=ONE
stateNew(k,27)=ONE
  end if
  end if
  end if

  if (stateNew(k,28) .eq. ZERO) then
  if (EPS33 .gt. ZERO) then

```

```

    if (((EPS33/(YT/E3))**TWO) + ((TWO*EPS13/(ST/G13))**TWO)
        + ((TWO*EPS23/(ST/G23))**TWO)) .gt. ONE) then
stateNew(k,13)=ONE
stateNew(k,28)=ONE
    end if
    else
    if (((EPS33/(YC/E3))**TWO) + ((TWO*EPS13/(ST/G13))**TWO)
        + ((TWO*EPS23/(ST/G23))**TWO)) .gt. ONE) then
stateNew(k,13)=ONE
stateNew(k,28)=ONE
    end if
    end if
    end if
! ** Criterion
    if (stateNew(k,26) .eq. ZERO) then
stateNew(k,14)=abs(EPS11)
stateNew(k,20)=abs(stressNew(k,1))
    end if

    if (stateNew(k,27) .eq. ZERO) then
stateNew(k,15)=abs(EPS22)
stateNew(k,17)=abs(EPS12)
stateNew(k,18)=abs(EPS23)
stateNew(k,21)=abs(stressNew(k,2))
stateNew(k,23)=abs(stressNew(k,4))
stateNew(k,24)=abs(stressNew(k,5))
    end if

    if (stateNew(k,28) .eq. ZERO) then
stateNew(k,16)=abs(EPS33)
stateNew(k,19)=abs(EPS13)
stateNew(k,18)=abs(EPS23)
stateNew(k,22)=abs(stressNew(k,3))

```

```

stateNew(k,25)=abs(stressNew(k,6))
stateNew(k,24)=abs(stressNew(k,5))
end if
end if
c
! ** if in one of the failure modes damage variable is equal to unity
if ((stateNew(k,7) .eq. ONE) .or. (stateNew(k,8).eq.ONE)
1 .or. (stateNew(k,9).eq.ONE) .or. (stateNew(k,10).eq.ONE)
2 .or. (stateNew(k,11).eq.ONE) .or. (stateNew(k,12).eq.ONE)) then
! ***** Delete Element
tateNew(k,29)=ZERO
end if
! ** Update Energy
c real new_energy
new_energy=HALF*((stressOld(k,1)+stressNew(k,1))*strainInc(k,1)
3 +(stressOld(k,2) + stressNew(k,2))*strainInc(k,2)
4 +(stressOld(k,3) + stressNew(k,3))*strainInc(k,3)
5 +(stressOld(k,4) + stressNew(k,4))*strainInc(k,4)*TWO
6 +(stressOld(k,5) + stressNew(k,5))*strainInc(k,5)*TWO
7 +(stressOld(k,6) + stressNew(k,6))*strainInc(k,6)*TWO)
c
enerInternNew(k)=enerInternOld(k) + (new_energy/density(k))
c
end if
1000 continue
end do
return
end

```

CURRICULUM VITAE

PERSONAL INFORMATION

Surname, Name: Hosseinpour Dashatan, Saeid

Nationality: Iranian

Date and Place of Birth: 1984, Tabriz, Iran

Marital Status: Married

E-Mail Address: saeid.dashatan@gmail.com

saeid.dashatan@metu.edu.tr

EDUCATION

Degree	Institution	Year of Graduation
M.S.	Urmia University	2012
B.S.	Azad University of Tabriz	2006

AREAS OF INTEREST

- Damage and Fracture in Advanced Composite Materials
- Composite Bonded Joints
- Recycling of Composite Materials

RESEARCH EXPERIENCE

Project Title: Damage Analysis in Advanced Tapered Composite Laminates/Impact Damage in Composite Laminates (Founded by Turkish Aerospace Industries, TAI),

May 2017- November 2020, Ankara, Turkey

PROFESSIONAL EXPERIENCE

Research Assistant: TED University, September 2015-September 2021

Teaching assistant for following courses: Introduction to Solid Mechanics, Mechanics of Materials, Material Science, Numerical Methods, Machine Design, Applied Finite Element Analysis, Design and Manufacturing, Dynamics, Measurement and Instrumentation, Experimental Engineering, Fundamentals of Metal Forming, Fundamentals of Composite Materials

LANGUAGES

- Azerbaijani: Mother Tongue
- Persian: Native
- Turkish: Advanced
- English: Advanced

PUBLICATIONS

Conferences

- Saeid H. Dashatan, Levend Parnas, Demirkan Coker, “2D and 3D Modelling of Delamination in Tapered Composite Laminates Using Cohesive Elements”, 8th Asian/Australian Rotorcraft Forum, Ankara, Turkey, Oct. 30 - Nov. 2, 2019. (Best Paper Award)
- Reyhan Deniz Atay, Saeid Hosseinpour Dashatan, Levend Parnas, “Failure Analysis In Adhesively Bonded Composite Joints,” 10th Ankara International Aerospace Conference, September 18-20 2019.

- Saeid H. Dashatan, Levend Parnas, Demirkan Coker, Mohsen Poorzeinolabedin, “Delamination Analysis of Tapered Composite Laminates using Cohesive Elements, 7th Asian/Australian Rotorcraft Forum, Jeju Island, Korea, Oct. 30 - Nov. 1, 2018.

Journal Papers

- Mohsen Poorzeinolabedin, Levend Parnas, Saeid Hosseinpour Dashatan, “Resin infusion under flexible tooling process and structural design optimization of the complex composite part” journal of Materials and Design, 64 (2014) 450-455, <https://doi.org/10.1016/j.matdes.2014.08.008>.
- Saeid Hoseinpour Dashatan, Taher Azdast, Samrand Rash Ahmadi, Arvin Bagheri “Friction Stir Spot Welding of Dissimilar Polymethyl Methacrylate and Acrylonitrile Butadiene Styrene Sheets,” Journal of Materials and Design, 45 (2013) 135–141, <https://doi.org/10.1016/j.matdes.2012.08.071>.